Order Number 9130393

Optical properties of amorphous silicon nitride films

Yin, Zhiping, Ph.D.

City University of New York, 1991

U·M·I

300 N. Zeeb Rd.
Ann Arbor, MI 48106

OPTICAL PROPERTIES OF AMORPHOUS SILICON NITRIDE FILMS

by

ZHIPING YIN

A dissertation submitted to the Graduate Faculty in Physics in partial fulfillment of the requirements for the degree of Doctor of Philosophy, The City University of New York.

1991

This manuscript has been read and accepted for the Graduate Faculty in Physics in satisfaction of the dissertation requirement for the degree of Doctor of Philosophy.

May 1, 1991
Data

Frederick W. Smith
Chair of Examining Committee

May 7, 1991
Data

Executive Officer

Supervisory Committee

The City University of New York

Abstract

Optical Properties of Amorphous Silicon Nitride Films

By

Zhiping Yin

Adviser : Professor F.W. Smith

The optical dielectric function ε (1.5 to 6.25 eV), infrared (IR) absorption (400-4000 cm^{-1}), and film density have been measured for a series of a-$Si_xN_yH_z$ films prepared by plasma enhanced CVD (PECVD). From a detailed analysis of the infrared absorption bands, dielectric functions, and density results, the concentrations of Si-H, N-H, Si-Si, and Si-N bonds and of Si, N, and H atoms have been obtained for the films studied. The effects of substrate temperature T_S, reactant ratio R, and power density on the film composition, density and dielectric function have been studied. The temperature-dependence and annealing behavior of the IR absorption in a-$Si_xN_yH_z$ films have been observed from 77 °K up to 350 °C. The effects of temperature on hydrogen bonding, O-H· · ·O, have been observed in a-$Si_xO_yH_z$ films. No strong effect of temperature on hydrogen bonding, N-H· · ·N, in a-$Si_xN_yH_z$ has been observed. It has been found that the N-rich diimidelike films prepared here have very low porosities and are thermally stable up to 700 °C.

A microstructural model based on Si-centered tetrahedra is developed for a-$Si_xN_yH_z$ alloys. The dependence of the optical dielectric function ε of the a-$Si_xN_yH_z$ alloys on stoichiometry ([N]/[Si] ratio) and hydrogen content has been determined for (1) Si-rich a-Si_xN_{1-x} alloys (containing no hydrogen); (2) N-rich a-$Si_xN_{y-z}(NH)_z$ alloys. By using the Si-centered tetrahedron model as combined with the Bruggemenn effective-medium approximation (EMA) analysis, Si-Si bond concentrations in the a-$Si_xN_yH_z$ films can be obtained reliably since Si-Si weak bonds have a strong effect on the dielectric function ε.

A free energy model (FEM) for bonding in amorphous covalent alloys is developed and applied to the ternary a-$Si_xN_yH_z$ alloy system. The Gibbs free energy of mixing $G_M = H_M - TS_M$ is obtained with use of the quasichemical approach to the thermodynamics of regular solutions, where H_M is enthalpy of mixing and S_M is the entropy of mixing. Chemical ordering (CO) in these alloys is shown to correspond to the preference for Si-N and Si-H bonds at the expense of Si-Si and N-H bonds. Using the FEM, the bond concentration fractions can be predicted.

ACKNOWLEDGEMENTS

I would like to express my deep gratitude to my adviser, Professor Fred W. Smith, for his patient guidance, encouragement, and continued support throughout my graduate education. His understanding was most helpful in my research and his constant advice was irreplaceable while I was far away from my own country and needed some guidance.

I express my grateful acknowledgement to Dr. David Tsu of North Carolina State University for providin and preparing the a-$Si_xO_yH_z$ sample and for his interest in this research and many helpful discussions, Dr. Ken Mui (our former postdoc) for his help and guidance at the beginning of my research work, especially in computer technology, Dr. R. Sabatini of Brookhaven National Laboratory (Upton, NY) for carrying out the SAM measurements on our samples, and Professors A. Woodward and M. Fishman of the Chemistry Department for the use of their FTIR and vis-uv spectrophotometers, respectively.

I am grateful to the Physics Department machine shop personnel for their professional help and expert suggestions concerning the design for the sample preparing system.

I thank the members of my thesis committee, Professors J. Gersten, R. Marino, M. Sarackik, and A. Woodward for their guidance and help.

I thank the members of our group: M. Sommer, A. Galea, and Professor R.B. Wang (visiting scholar from Northwest University in China) for their assistance and friendship and for contributing to the good working environment in our lab.

Finally, I wish to thank my husband and my parents for their encouragement and continual support, and to thank my father-in-law and my former English tutor Ms. A. Liu (retired) for their great help. They all have contributed to this dissertation.

CONTENTS

LIST OF TABLES

LIST OF FIGURES

Chapter 1 Introduction and Background

The study of silicon nitride thin films has begun in the early 1960's. These films can be deposited via a variety of techniques (Morosanu, 1980) such as chemical vapor deposition, chemical transport, direct nitridation, rf glow discharge, rf sputtering, vacuum evaporation, and ion implantation. Among them plasma-assisted depositions with low substrate temperatures (usually less than 400 °C) are becoming increasingly important as semiconductor device dimensions decrease and the deposited dielectrics must meet many requirements such as the requirements for optical parameters, hardness, thermo-stability, etc. for the dielectric films.

Plasma deposited silicon nitride is used mainly as a passivation coating over silicon integrated circuits to protect active areas of the circuit from contamination by preventing diffusion of sodium and moisture from the surface of the passivation coating to the inner circuit. The efficiency of the silicon nitride as a diffusion barrier is very significant as can be seen from the following experimental data. The results obtained by Saga et al (1982) and Kern and Rosler (1977) showed that there are less than 1% of sodium chloride diffusing more than 100 nm from the surface of the plasma-deposited silicon nitride for 10 to 20 hours at 550 to 600 °C. Capacitance-voltage measurements on 100 nm thick films of plasma silicon nitride on silicon show no measurable shift after 1 min. bias at 100 °C and 10^6 V/cm (Swann et al, 1967). For comparison, shifts of about 9V occur

with 100 nm of thermally grown silicon dioxide. For testing the effect of moisture, Kern and Rosler (1977) found that the oxidation rate in steam at 1200 °C is 3.5 nm/hr. For comparison, over 800 nm of oxide grow on single crystal silicon in one hour under similar conditions. Obviously, plasma silicon nitride improves the reliability of devices because of its excellent barrier properties.

Furthermore, since silicon nitride is a hard material, it can be used to protect the soft aluminum metal lines from scratches and mechanical damage (Sinha et al,1978; Mar and Samuelson, 1980; van de Ven, 1981; Baerg et al, 1983; Maes et al, 1983). Beside the applications mentioned above, the following applications for plasma deposited silicon nitride are also important : coatings for gallium arsenide to prevent evaporation of arsenic during heat treatment (Bartle et al, 1984; Ishii et al, 1984; Helix et al, 1987; Campbell and Baliga, 1983; Valco and Kapoor, 1983), gate dielectrics for transistors (Katoh et al, 1983; Woodward et al, 1981; Hezel at al, 1984), insulators between metal levels (Maeda and Nakamura, 1984; Summers, 1983), etch masks in multilevel resist structures (Soller et al, 1984), and dielectric and antireflection coatings for solar cells and photodetectors (Hezel and Schorner, 1981; Watanabe et al, 1984).

Because of the high technological importance of silicon nitride thin films in applications, especially in electronics, these films have been studied intensively both experimentally and theoretically. A considerable volume of information has been generated on Si-rich ([N]/[Si] < (4-5z)/(3-2z), here z is the fraction of hydrogen atoms in a film, see detail in section 7.4 of chapter 7) silicon nitride thin films in

the past years. However, it has been demonstrated recently (Tsu et al, 1986; Lucovsky and Tsu, 1987) that N-rich silicon nitride films ([N]/[Si] > (4-5z)/(3-2z)) can be deposited with compositions approaching that of silicon diimide, a-$Si(NH)_2$. These films can serve as useful low-temperature dielectric layers (Jousse et al, 1988). In addition, such polymeric layers can be relatively stable thermally, apparently up to at least 600 °C (Budhani et al, 1987). Based on this point, the study of silicon nitride thin films in this research project is focused on the N-rich silicon nitride thin films prepared by plasma-enhanced chemical-vapor-deposition (PECVD).

The films prepared by PECVD are generally referred to as hydrogenated amorphous silicon nitride, a-$Si_xN_yH_z$. The amount of incorporation of hydrogen into the film depends on deposition conditions such as substrate temperature T_s, reactant ratio R = NH_3/SiH_4, rf power density, and total pressure. The physical, electrical, and optical properties of the a-$Si_xN_yH_z$ films are strongly dependent on the film composition, i.e., the [N]/[Si] ratio y/x and the hydrogen content z. It is clearly important to establish as close a correlation as possible between the macroscopic properties of these N-rich a-$Si_xN_yH_z$ films and the film microstructure, i.e., the local atomic bonding configurations involving the Si, N, and H atoms.

This thesis consists of two major parts : an experimental part and a theoretical part.

The experimental part includes :

(1) Detailed measurements and analysis (Yin and Smith, 1990B) of the optical dielectric function ε in the range 1.5 eV to about 6.25 eV, of the infrared absorption in the range from 400-4000 cm^{-1}, and of the film density ρ for a-$Si_xN_yH_z$ films with the [N]/[Si] ratio y/x from 1.31 to 2.63 and hydrogen content from 19 at% to 54 at% (z=0.19 to 0.54), in addition, careful observation and analysis of the effects of hydrogen bonding in a-$Si_xO_yH_z$ (Yin and Smith, 1989A) and a-$Si_xN_yH_z$ films.

(2) The results for the effect of deposition parameters, such as substrate temperature T_s, reactant ratio R=NH_3/SiH_4, and deposition power density, on the growth rate and properties of the a-$Si_xN_yH_z$ films. Furthermore, the suggestions for the optimized deposition parameters for high quality N-rich a-$Si_xN_yH_z$ alloy films.

The theoretical part is divided in two parts. They are :

(1) A microstructural model for hydrogenated amorphous silicon nitride alloys based on a random mixture of Si-centered tetrahedra (Yin and Smith, 1989B, 1990A). In the Si-centered tetrahedron model, the tetrahedra are considered to be the fundamental structural units determining the optical response of the alloys. After combining the Si-centered tetrahedron model with an effective-medium-approximation (EMA) (Bruggemann, 1935) analysis, the dielectric functions ε for a-$Si_xN_yH_z$ alloys can be predicted. In addition, the EMA analysis has also made it possible to specifically estimate the Si-Si bond concentrations in the films studied. This is an important point since it has been suggested recently (Jousse and

Kanicki, 1989) that Si-Si and Si-H bonds are potentially harmful defects in the a-$Si_xN_yH_z$ films used in device-related applications. Furthermore, there is not yet any valid method to directly measure the existence of Si-Si bonds in these films.

(2) A free energy model (FEM) for bonding in amorphous covalent alloys (Yin and Smith, 1991). This model is based on the quasichemical approach to the thermodynamics of regular solutions (Gordon, 1968), which includes chemical-bonding effects in the enthalpy and effects due to the statistics of bonding within local structural units, i.e., Si-centered tetrahedra, in the entropy. By using the FEM, the bond concentration fractions can be predicted for a-$Si_xN_yH_z$ alloys as functions of the composition x, y, and z, where $x + y + z = 1$.

Details of the experimental set-up and procedure will be presented in chapter 2. The experimental measurements and data analysis for the dielectric function for a-$Si_xN_yH_z$ films in the range from 1.5 eV to about 6.25 eV will be given in chapter 3. Infrared absorption results, which include bonding species and annealing effects for a-$Si_xN_yH_z$ films, are shown in chapter 4. In chapter 5, the effects of deposition parameters (T_s, reactant ratio R, and power density) on film properties will be discussed in detail. Then, the optimized deposition parameters for high quality N-rich a-$Si_xN_yH_z$ films will be given. The EMA analysis for a-$Si_xN_yH_z$ alloys based on the Si-centered tetrahedron model is developed in chapter 6 and in chapter 7 the free energy model (FEM) for a-$Si_xN_yH_z$ alloys based on the quasichemical approach to the thermodynamics of regular

solutions is developed. Finally, conclusions and suggestions for further work follow in chapter 8.

Chapter 2 Experimental Apparatus and Procedures

2.1 Deposition System

As mentioned in chapter 1, silicon nitride films can be prepared in many different ways. Plasma-enhanced chemical-vapor-deposition (PECVD) via an rf (radio frequency) glow discharge was used for sample preparation in this research project.

The deposition system is shown schematically in Fig.2-1. The rf power supply (eni power systems, Inc. model HF-300) is capacitively-coupled to the powered electrode at 13.56 MHz through an rf matching network (Heathkit Deluxe Antenna Tuner model SA-2060A) which consists of two variable capacitors and a variable inductor as shown in Fig.2-1. The purpose of this matching network is to increase the power dissipation in the discharge, and to protect the power supply.

The two parallel electrodes are 3 inches in diameter and are separated by 1 inch. They are shielded from the plasma except for their front surfaces by grounded plasma shields which are made of stainless-steel (see Fig.2-1). The sample electrode is made of copper and contains a heater, a thermocouple for the temperature measurement, and the stainless-steel mask for holding the substrates. The heater (ARI BXX-06B41-4k) in the form of a spiral is mounted underneath the sample electrode (see Fig.2-1) and can heat the substrate up to about 600 °C. The heater and electrode are

isolated from each other by Macor, a Dow Corning ceramic. The substrate temperature was measured by a chromel-alumel thermocouple which is isolated electrically by a ceramic tube and placed just below the sample substrate. The substrate temperature is controlled by a controller (Model 149, Omega Engineering, Inc.). The other electrode, which is grounded in our experiment, is made of stainless-steel.

In the rf glow discharge used here, the discharge is generated between the two electrodes. Because of the large difference in mobility between electrons and ions in a glow discharge, a large electron current flux is directed toward the powered electrode during one-half of the cycle while a much smaller ion current flux occurs during the other half of the cycle. Therefore, the powered electrode (i.e., sample electrode in our experiment) is negatively biased to an average voltage V_S so that the net current is equal to zero. The self-bias voltage V_S was measured by a dc voltmeter connected to the powered electrode through an inductor which blocks rf power from the dc voltmeter (see Fig.2-1).

There are two pumping systems connected to the deposition chamber, as shown in Fig.2-1. The initial pumping is achieved by a Veeco diffusion pump (model EP2A-1) and Welch mechanical pump (model 1402). The pressure can reach 4×10^{-7} Torr with a liquid nitrogen trap using this pumping system. During the deposition, another pumping system which consists of a Roots pump (Leybold-Heraeus, RUVAC single stage roots pump, model WS150) and a backing pump (TRIVAC dual stage rotary vane pump, Leybold-

Heraeus, model D8A) is used. In order to prevent back-streaming of oil from the backing pump to the Roots pump, nitrogen gas was introduced between the Roots pump and backing pump. The pressure in that position was monitored by a thermocouple gauge (Leybold-Heraeus, THERMOVAC TM210). The pumping speed was controlled by a pressure control system in order to maintain a constant pressure in the deposition chamber. An MKS Baratron type 170 high accuracy capacitance manometer pressure measurement and control system was used for pressure control. This system consisted of a pressure sensor head (type 315BSH-10) with temperature controller (type 170M-39A), electronics unit (type 170M-6C) with digital readout unit (type 170M-27E), exhaust valve controller (type 252A), and a exhaust control valve (type 253A).

Since silane is spontaneously flammable and ammonia is toxic and flammable, special treatment is needed for the exhaust gases. Therefore, the exhaust gases from the discharge were first passed through a filter (Leybold-Heraeus, AF exhaust filter, model AF8-16A), diluted with N_2, and finally passed through a NaOH bubbler for neutralization.

The reactant gases, silane (SiH_4) and ammonia (NH_3) in our experiment, pass independently through MKS mass flow meters (258B) controlled by MKS series 260 control system (included type 260 controller, type 261 display, and type 260 PS-3 power supply). They then are fed into a gas mixing box which is sealed underneath the top flange of the deposition chamber. Inside the gas mixing box, three compartments were separated by two planes with one hole on

the side of each plane. These two holes along with the hole on the bottom of the gas mixing box were all arranged as far apart as possible in order to increase the distance traveled by the gases so as to enhance mixing. Finally, the mixture of gases enters into the deposition chamber from the hole on the bottom of the gas mixing box.

A mass spectrometer (INFICON IQ 200 Mass Analyzer, Leybold-Heraeus) was mounted on top of the deposition system (see Fig.2-1) for monitoring the gas species in the deposition chamber. A pressure converter (IPC-1) was used for reducing the partial pressure of each of the components in the gas mixture prior to analysis. The pressure converter has a $1\frac{1}{2}$ inch main valve and a small orifice valve to isolate the mass spectrometer from the deposition chamber. The orifice valve is used for analysis of gases when the chamber pressure is too high for the mass spectrometer.

2.2 Substrate Selection

For the purpose of characterizing the film properties, films have been deposited on different substrates. Polished clear fused quartz (0.75" × 0.5" and thickness of about 16 mils) was employed for optical constants measurements in the visible and ultra-violet range. Intrinsic <111> Si (resistivity > 2500 Ω-cm), polished on both side (0.75" × 0.5" and thickness of about 12 mils) was used for infrared measurements. For the density measurements, we used high purity aluminum foil (0.5" × 0.5" with thickness of 9.8 mils) as a substrate.

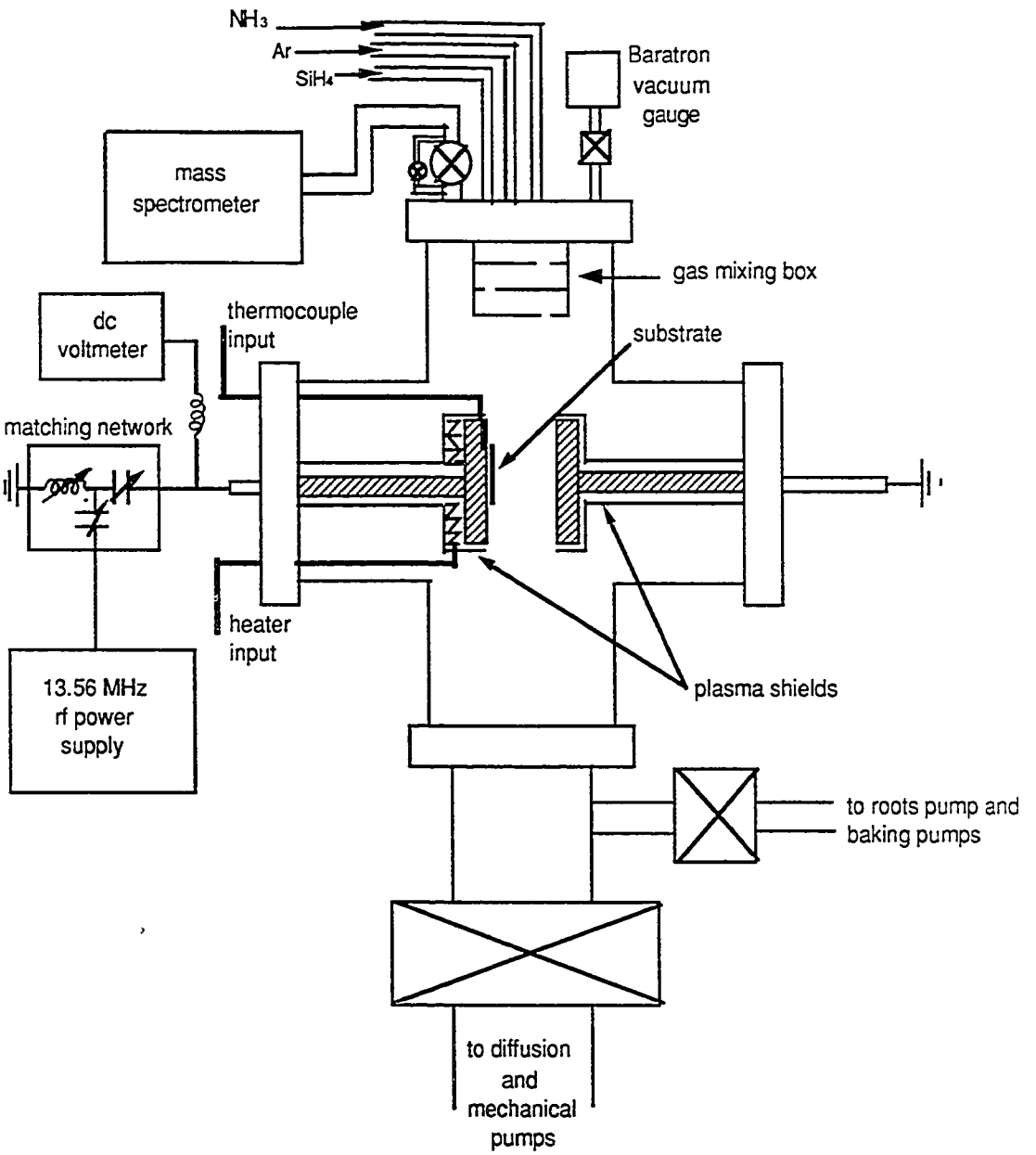

Fig.2-1 Schematic of rf glow discharge deposition system.

2.3 Sample Preparation

Before the substrates were mounted on the substrate holder, the quartz and aluminum substrates were cleaned ultrasonically in TUD (transene ultrasonic detergent, made by Transene Co., Inc.), and the Si substrates were cleaned by boiling in Transene 100 (Transene Co,, Inc.). Then, all the substrates were rinsed in deionized water and finally blown dry with N_2 gas. After cleaning, the substrates were mounted on the powered electrode. The deposition system was pumped down by diffusion and mechanical pumps overnight. In order to remove any surface contaminant, especially water vapor, the deposition system was baked out during the overnight pumping. The final pressure of system could reach 4×10^{-7} Torr with liquid nitrogen in the cold trap. Then the pumping system was switched to the Roots pump and backing pump for deposition. The pressure of the deposition chamber was controlled by the exhaust control valve to the desired value, typically 0.5 or 0.15 Torr. Before the film deposition, an argon discharge was carried out for about 5 minutes in order to clean the substrate by bombardment due to argon ions. After argon cleaning, the system was pumped down to about 1×10^{-6} Torr again using the diffusion pump. Then undiluted silane and ammonia were delivered via independent lines to the deposition chamber. After reaching a stable pressure, rf power was turned on to start the film deposition.

The properties of the films prepared by rf glow discharge depended on a number of parameters including substrate

temperature, ratio of the reacting gases, rf power density and frequency, and reaction chamber geometry. Here, three parameters are studied: 1) reactant ratio varied from R = NH_3/SiH_4 = 10, 20, and 40 with constant substrate temperature, total pressure and flow rate, and discharge power density. 2) discharge power density varied from 0.12, 0.17, 0.22, and 0.63 W/cm^2 with other deposition parameters held constant. 3) substrate temperature T_S varied from 100, 200, and 550 °C with other parameters held constant. The deposition conditions for the samples studied are listed in Table 2-1.

Table 2-1 Deposition parameters for a-$Si_xN_yH_z$ films*

Sample	deposition temp. T_S (°C).	NH_3 (sccm)**	SiH_4 (sccm)**	NH_3/SiH_4 R	power density (W/cm^2)
1	400	100	10	10	0.43
2	400	100	5	20	0.43
3	400	100	2.5	40	0.43
4	400	60	1.5	40	0.43
5	400	240	4	60	0.12
6	400	240	4	60	0.17
7	400	240	4	60	0.22
8	400	240	4	60	0.63
9	100	240	4	60	0.43
10	200	240	4	60	0.43
11	550	240	4	60	0.43

* Note that the deposition pressure is P=0.5 Torr for all the samples except for sample 4 where P=0.15 Torr.
** sccm: cubic centimeters per minute at STP.

2.4 Characterization

The optical properties of the a-$Si_xN_yH_z$ films have been examined in the visible-ultraviolet and infrared regions. The measurements of the film reflectance R and transmittance T for determining the dielectric function were carried out on an Aviv 14DS visible-uv spectrophotometer in the range 1.5-6.5 eV. A specular reflectance accessory calibrated using an NBS SRM 2023 specular reflectance standard mirror is employed for the determination of R. The NBS standard mirror calibration has been extended from 4.9 up to 6.7 eV using the known optical constants [D. E. Aspnes, 1983; H. R. Philipp, 1972] of a polished Si wafer.

Infrared measurements were carried out using a Digilab FTS-40 Fourier transform infrared spectrophotometer in the range from 400 to 4000 cm^{-1}, with a resolution of 8 cm^{-1}. For hydrogen bonding studies, infrared measurements were taken at various temperatures. A heating accessory was used to heat the film from room temperature up to 350 °C. For liquid nitrogen temperature (77 K) measurements, a Harrick dewar accessory (model DER-300) was used. The infrared absorption of the R=40, P=0.15 Torr film has also been measured after annealing the film at 700 and 1000 °C. The annealing is done in an electric tube furnace (Lindberg Hevi-Duty, type 54031) in an argon ambient. In order to avoid the possibility of oxidation, argon was flowed for one hour at flow rate 1.5 scfh (cubic feet per hour at STP) before putting the sample into the furnace. Then the sample was put into the furnace with flow rate 2.0 scfh for

one hour at the desired temperature. The flow of argon was maintained during and after the annealing until the sample cools down to room temperature.

Film densities have been obtained by determining the masses and the volumes of the films. The masses of the films were determined by weighing the Al-foil substrate before and after deposition using a Cahn electrobalance (model 26). The volumes of the films were obtained from measurements of film area and from thickness profiles which were obtained from optical measurements (see details in section 5.1 of chapter 5). Information concerning film composition has been obtained via depth profiling using a Perkin-Elmer PHI 600 scanning Auger microprobe (SAM) at Brookhaven National Labs. The depth profile of each film was obtained by sputtering using a 3-keV Ar^+-ion beam. Unfortunately, since the SAM sensitive factors for N and Si atoms in a-$Si_xN_yH_z$ alloys are unknown, the absolute value of the [N]/[Si] ratio for each sample can not be determined from the SAM measurement. Nevertheless, changes in the [N]/[Si] ratios between different samples, which are independent of the SAM sensitive factors for N and Si atoms, can be obtained. Therefore, SAM results can serve as a good check for our composition results obtained by using optical analysis (see details in section 5.2 of chapter 5).

Chapter 3 Optical Properties of $a\text{-}Si_xN_yH_z$ in the Visible-UV Region

3.1 Introduction

For a dielectric material, the complex frequency-dependent dielectric function $\varepsilon = \varepsilon_1 - i\varepsilon_2$ is an important parameter which describes the polarizability of a material in an external electric field. The dielectric function is related to the complex refractive index n by $\varepsilon = (n)^2 = (n - ik)^2$, i.e. $\varepsilon_1 = n^2 - k^2$ and $\varepsilon_2 = 2nk$. The real part of the refractive index n describes the propagation velocity of the light wave in the optical transparency region. The extinction coefficient k describes the attenuation of the electromagnetic wave while it traverses a material. In the Si-centered tetrahedron model (see chapter 6), the optical response of the alloys is determined by the fundamental tetrahedral structural units. Therefore, the optical constants (ε, n, and k) can provide important information concerning the atomic structure and bonding configurations present in amorphous films by using the Si-centered tetrahedron model with the Bruggemann effective medium approximation (see detail in chapter 6). Furthermore, the extinction coefficient is simply related to the absorption coefficient by $\alpha = 4\pi k/\lambda$. Here λ is the wavelength of the light in vacuum. From the shape of the optical absorption curve, one can gain important information about the width of energy gap and the tail states in the gap for amorphous materials.

3.2 Reflectance and Transmittance for the $a\text{-}Si_xN_yH_z$/quartz System

When a beam of light is normally incident on a surface which separates the media of refractive indices n_m and n_{m+1} as shown in Fig.3-1 , the relation between the amplitudes of the transmitted and reflected electric vectors and the amplitude of incident electric vectors is given as (Heavens, 1955):

$$\frac{E_m^-}{E_m^+} = \frac{n_m - n_{m+1}}{n_m + n_{m+1}} = r_{m+1} \qquad (3\text{-}1)$$

$$\frac{E_{m+1}^+}{E_m^+} = \frac{2n_m}{n_m + n_{m+1}} = t_{m+1} \qquad (3\text{-}2)$$

where E_m^+ and E_m^- are the electric vector of the positive-going beam and the negative-going beam, respectively, in the mth medium. Here, n_m can be a complex refractive index. r_m and t_m are known as the Fresnel reflection and transmission coefficients. We will see that it is convenient to use these Fresnel coefficients in the case of multiple layer systems. When a beam is incident on a multiple layer system, multiple reflection and transmission are created from this multiple interface system. Therefore, the transmitted and reflected beams for the system are the summation of those multiple reflected and transmitted elements which will be a very complex computation. By using matrix method in terms of Fresnel coefficients (Heavens, 1955), the electric vectors of the (m-1)th layer can be expressed in matrix form by:

$$\begin{pmatrix} E_{m-1}^{+} \\ E_{m-1}^{-} \end{pmatrix} = \frac{1}{t_m} \begin{pmatrix} e^{i\delta_{m-1}} & r_m e^{i\delta_{m-1}} \\ r_m e^{-i\delta_{m-1}} & e^{-i\delta_{m-1}} \end{pmatrix} \begin{pmatrix} E_m^{+} \\ E_m^{-} \end{pmatrix} \qquad (3\text{-}3)$$

where $\delta_m = \frac{2\pi n_m d_m}{\lambda}$, and d_m is the thickness of the mth layer, and λ is the wavelength of the incident beam in vacuum.

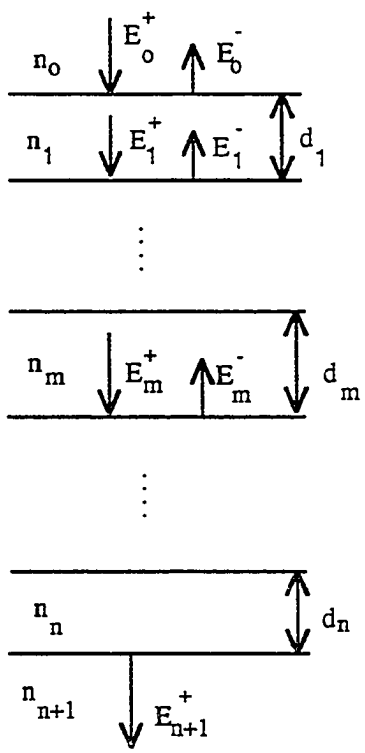

Fig.3-1 Multiple layer film system.

For a system of n layers (Fig.3-1), the relation between E_o^+, E_o^-, and E_{n+1}^+ obtained by using eqn.3-3 is as follows:

$$\begin{pmatrix} E_o^+ \\ E_o^- \end{pmatrix} = \frac{(C_1)(C_2)\ldots(C_{n+1})}{t_1 t_2 \ldots t_{n+1}} \begin{pmatrix} E_{n+1}^+ \\ E_{n+1}^- \end{pmatrix} \qquad (3\text{-}4)$$

where

$$(C_m) = \begin{pmatrix} e^{i\delta_{m-1}} & r_m e^{i\delta_{m-1}} \\ r_m e^{-i\delta_{m-1}} & e^{-i\delta_{m-1}} \end{pmatrix} \qquad (3\text{-}5)$$

Since there is no negative-going wave in the (n+1)th medium, E_{n+1}^- is equal to zero. After writing the matrix product

$$(C_1)(C_2)\ldots(C_{n+1}) = \begin{pmatrix} a & b \\ c & d \end{pmatrix} \qquad (3\text{-}6)$$

we obtain, from eqn.3-4

$$\begin{pmatrix} E_o^+ \\ E_o^- \end{pmatrix} = \frac{1}{t_1 t_2 \ldots t_{n+1}} \begin{pmatrix} aE_{n+1}^+ \\ cE_{n+1}^+ \end{pmatrix} \qquad (3\text{-}7)$$

then,

$$\frac{E_o^-}{E_o^+} = \frac{c}{a} \quad \text{and} \quad \frac{E_{n+1}^+}{E_o^+} = \frac{t_1 t_2 \ldots t_{n+1}}{a} \qquad (3\text{-}8)$$

The reflectance and transmittance are given by:

$$R = \frac{(E_o^-)(E_o^-)^*}{(E_o^+)(E_o^+)^*} \quad \text{and} \quad T = \frac{n_{n+1}}{n_o} \frac{(E_{n+1}^+)(E_{n+1}^+)^*}{(E_o^+)(E_o^+)^*} \qquad (3\text{-}9)$$

where the superscript * indicates the complex conjugate. Substituting eqn.(3-8) into (3-9) and setting $n_o = n_{n+1} = n_{air} = 1$ and $k_o = k_{n+1} = k_{air} \equiv 0$, we finally obtain the reflectance and transmittance for an n mutiple-layer system as follows:

$$R = \frac{cc^*}{aa^*} \quad \text{and} \quad T = \frac{(t_1 t_2 \ldots t_{n+1})(t_1^* t_2^* \ldots t_{n+1}^*)}{aa^*} \qquad (3\text{-}10)$$

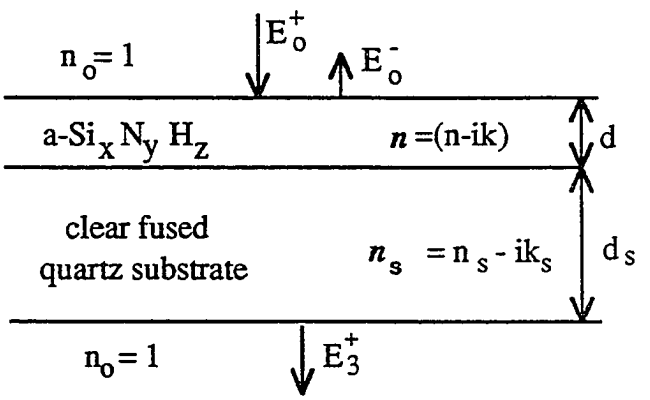

Fig.3-2 Our sample system.

For our optical system, an amorphous silicon nitride film is deposited on the top of a clear fused quartz substrate (see Fig.3-2). After using the above theory, the reflectance R and transmittance T

as functions of n, k, and d for the a-$Si_xN_yH_z$ film are obtained. These can be written in the following forms :

$$R(n,k,d,\lambda) = \frac{R1}{D} \quad \text{and} \quad T(n,k,d,\lambda) = \frac{T1}{D} \qquad (3\text{-}11)^*$$

(see footnote below for explicit expressions for R1, T1, and D).

---

* By using eqn.(3-5), (3-6), and (3-10), $R1 = cc^*$, $T1 = (t_1t_2t_3)(t_1^*t_2^*t_3^*)$, and $D = aa^*$ were given as follows:

$R1 = \beta_2[gh_2/\beta_1+gh_1\beta_1+t\cos\gamma+u\sin\gamma]+gh_3/\beta_2[1/\beta_1+gh_1gh_2\beta_1+v\cos\gamma-w\sin\gamma]$

$D = \beta_2[\beta_1+gh_1gh_2/\beta_1+v\cos\gamma+w\sin\gamma]+gh_3/\beta_2[gh_2\beta_1+gh_1/\beta_1+t\cos\gamma-u\sin\gamma]$

$T1 = [(1+g_1)^2+h_1^2][(1+g_2)^2+h_2^2][(1+g_3)^2+h_3^2]$

$t = 2(g_1g_2+h_1h_2), \qquad u = 2(g_1h_2-g_2h_1)$

$v = 2(g_1g_2-h_1h_2), \qquad w = 2(g_1h_2+g_2h_1)$

$gh_i = g_i^2 + h_i^2 \qquad i=1,2,3.$

$$\gamma = \frac{4\pi nd}{\lambda}$$

$$\beta_1 = \exp(\frac{4\pi kd}{\lambda}), \qquad \beta_2 = \exp(\frac{4\pi k_sd_s}{\lambda})$$

$$g_1 = \frac{n_o^2-n^2-k^2}{(n_o+n)^2+k^2}, \qquad h_1 = \frac{2n_ok}{(n_o+n)^2+k^2}$$

$$g_2 = \frac{n^2-n_s^2+k^2-k_s^2}{(n+n_s)^2+(k+k_s)^2}, \qquad h_2 = \frac{2(nk_s-n_sk)}{(n+n_s)^2+(k+k_s)^2}$$

$$g_3 = \frac{n_s^2-n_o^2+k_s^2}{(n_s+n_o)^2+k_s^2}, \qquad h_3 = \frac{-2n_ok_s}{(n_s+n_o)^2+k_s^2}$$

Since the quartz substrate does not provide interference because the roughness for the two surfaces of the quartz substrate (the substrate is 16 mils thick) is much larger than the wavelength of the incident beam, we have averaged out any interference effects due to the quartz substrate in our calculations. The n_s and k_s for the quartz substrate as functions of wavelength have been obtained from the measured values of reflectance R_{exp} and transmittance T_{exp} for the quartz substrate itself based on the same theory for R and T of a single layer, i.e. n =1.

3.3 Dielectric Function of a-$Si_xN_yH_z$

The optical constants n and k of a-$Si_xN_yH_z$ films have been extracted by a computer fitting procedure based on the above theory for the exact amplitudes of the reflected and transmitted waves and from the experimental data for reflectance R_{exp} and transmittance T_{exp} for the a-$Si_xN_yH_z$/quartz system. An example of R_{exp} and T_{exp} for the sample prepared at R = 20, P = 0.5 Torr, T_s = 400 °C, and power density = 0.43 W/cm^2 is given in Fig.3-3. In order to solve the equations for n and k, it is necessary to have an approximate thickness value as a starting point. This can be obtained from $d = \frac{\lambda_{m+1}\lambda_m}{2n(\lambda_m-\lambda_{m+1})}$. Here λ_m is the wavelength of the mth order of maximum reflectance or transmittance in region of $\lambda > 4500$ Å and n is the refractive index of the film in this region which is approximately equal to 2 for a-$Si_xN_yH_z$ alloys. Since the above expression for d is only valid for non-absorbing films, only the data of R and T in the region of $\lambda > 4500$ Å, in which region k is close to

zero for our sample, is used. The order of m for a given maximum is guessed initially. A constant d for all the maxima will be obtained when the correct m is used.

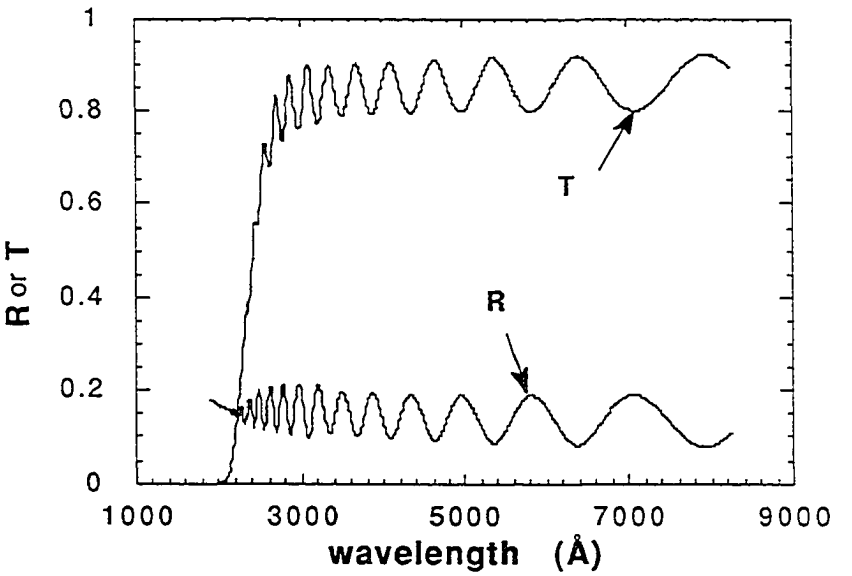

Fig.3-3 Transmittance T and reflectance R for the film prepared at R=20, P=0.5 Torr, T_s=400 °C, and power density=0.43 W/cm^2.

In order to solve the equations for n and k, the two-dimensional Newton-Raphson technique (Nagendra et al, 1981) was used. For two given functions with two unknowns, $f_1 = f_1(x, y)$ and $f_2 = f_2(x, y)$, this method yields the following iteration formulas for x and y:

$$x_{i+1} = x_i + \frac{f_2 \times \frac{\partial f_1}{\partial y} - f_1 \times \frac{\partial f_2}{\partial y}}{\frac{\partial f_1}{\partial x} \times \frac{\partial f_2}{\partial y} - \frac{\partial f_1}{\partial y} \times \frac{\partial f_2}{\partial x}} \qquad (3\text{-}10)$$

$$y_{i+1} = y_i + \frac{f_1 \times \frac{\partial f_2}{\partial x} - f_2 \times \frac{\partial f_1}{\partial x}}{\frac{\partial f_1}{\partial x} \times \frac{\partial f_2}{\partial y} - \frac{\partial f_1}{\partial y} \times \frac{\partial f_2}{\partial x}}$$

In our case, f_1 and f_2 are equal to the differences between theoretical and experimental results for reflectance and transmittance, respectively. In order to simplify the calculation, however, we choose:

$$f_1(n,k) = R1 - R_{exp} \bullet D \qquad (3\text{-}11)$$

$$f_2(n,k) = T1 - T_{exp} \bullet D$$

In these forms for f_1 and f_2, the derivatives of f_1 and f_2 will be much simpler since D is the same for R and T.

The computer fitting procedure was carried out by reading in experimental values of R_{exp}, T_{exp}, and d from the interference fringes, and initial values of n_o and k_o for a given wavelength λ. Then the program starts iterating until either f_1 and f_2 are smaller than the convergence value 10^{-16} or the iteration number exceeds 100. Examples of the solutions for n yielded by this method are given in Fig.3-4 for three different thickness. We can see that the solutions are not only the real continuous dispersion curve for the refractive index n but also the inadmissible solutions obtained for such complicated equations. From the dispersion curve obtained for the refractive index n, it is possible to infer whether the estimated film thickness is too high or too low (Nagendra et al, 1981). In Fig.3-4, the solutions for the true value of thickness, d = 2552 Å, fall on a

continuous dispersion curve, i.e., the curve is closed at the intersection point (as the arrow shows in Fig.3-4). In the case of an under or over-estimated thickness, these dispersion curves break at the intersection points, such as the curves for d = 2500 and 2600 Å in Fig.3-4. From the curvature of the solutions near an intersection point, such as upward or downward, one can tell if the d value chosen is too high or too low. By using this method, the accuracy of thickness is better than 1%, which has a negligible effect on n and k.

After finding n and k for a film, ε_1 and ε_2 are given by $\varepsilon_1 = n^2 - k^2$ and $\varepsilon_2 = 2nk$, and α by $\alpha = 4\pi k/\lambda$.

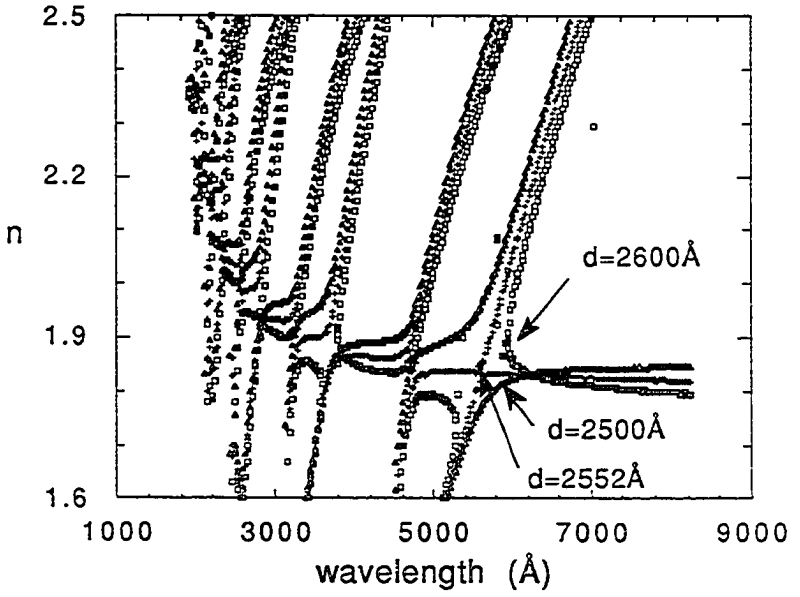

Fig.3-4 The solutions for refractive index n for the film prepared at R=40, P=0.15 Torr, T_S=400 °C, and power density=0.43 W/cm^2 yielded by the computer fitting procedure for three different thicknesses: d=2600 Å (too high), d=2552 Å (true value), and d=2500 Å (too low).

3.4 Optical Absorption Edge of a-$Si_xN_yH_z$

The typical density of states for amorphous semiconductors in the region of the energy gap is shown in Fig.3-5. The optical absorption of such a material consists of three regions as shown in Fig.3-6: 1) a shoulder corresponding to transitions from localized gap (defect) states to extended states for $\alpha \leq$ about 1 cm^{-1} (region A), 2) an exponential tail (region B) for α below about 10^4 cm^{-1} known as the Urbach tail and corresponding to transitions from localized tail states to extended band states, and 3) a slowly varying region (region C) for $\alpha >$ about 10^4 cm^{-1} corresponding roughly to band-to-band transitions. The optical absorption edge refers to regions B and C.

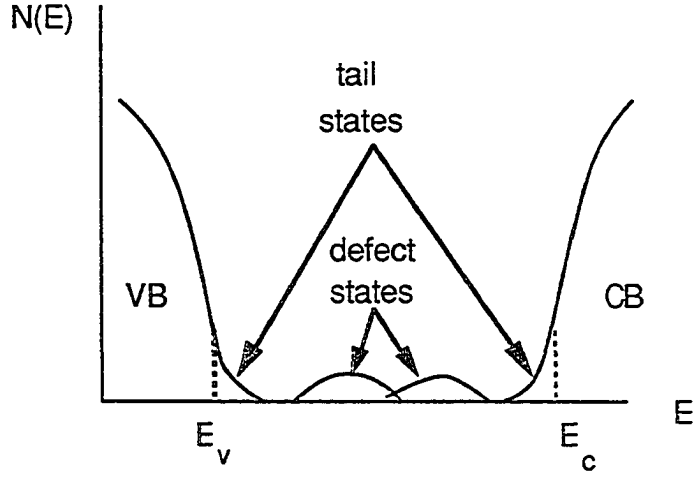

Fig.3-5 Density of states for an amorphous semiconductor. E_v, the top of the valence band (VB). E_c, the bottom of the conduction band (CB).

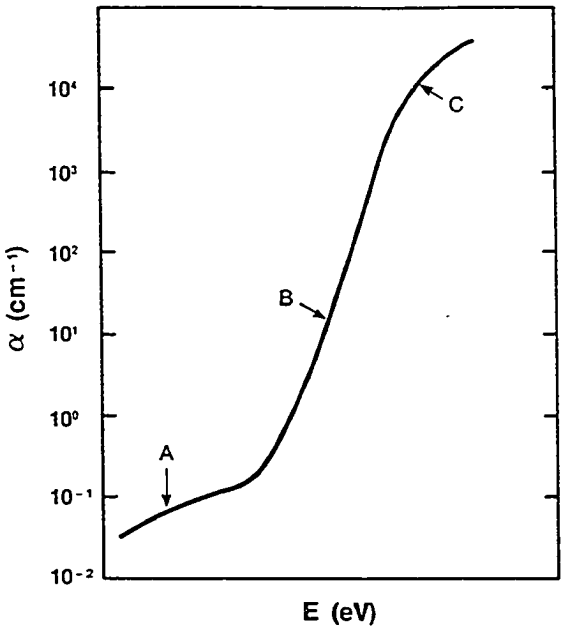

Fig.3-6 Idealized absorption edge of amorphous semiconductors.

The absorption in region B can be written in the following form (Pankove, 1984):

$$\alpha = \alpha_o \exp\left(\frac{E}{E_o}\right) \qquad (3\text{-}12)$$

where E_o is called the Urbach edge parameter and is related to the width of the tail of the valence band. Taking the natural logarithm, then :

$$\ln\alpha = \left(\frac{1}{E_o}\right)E + \ln\alpha_o \qquad (3\text{-}13)$$

Therefore, the Urbach edge parameter E_o can be obtained from the slope of $\ln\alpha$ vs energy E in region B.

In region C associated with band-to-band transitions, the imaginary part of the dielectric function ε_2 is given by Tauc et al (1966) as follows:

$$\varepsilon_2(E) = B(E - E_{opt})^2/E^2 \qquad (3\text{-}14)$$

where B is a constant independent of energy and E_{opt} is the optical energy gap which is approximately equal to $E_c - E_v$. From the plot of $E(\varepsilon_2)^{1/2}$ vs E, the optical energy gap E_{opt} can be obtained from the intercept of the plot in region C. In addition, the parameter E_{04}, the energy corresponding to $\alpha = 1\times10^4\ cm^{-1}$, can also be defined as an optical gap and is used very often for the comparison of the optical absorption edge for different amorphous semiconductors.

3.5 Experimental Results

The results obtained for the real part of dielectric function $\varepsilon_1=n^2-k^2$ and imaginary part of dielectric function $\varepsilon_2=2nk$ as functions of energy E between 1.5 and about 6.25 eV are given in Table 3-1 for all the samples studied. The deposition conditions for the samples are given in Table 2-1 (see chapter 2). The measured real part ε_1 and imaginary part ε_2 for samples with gas ratio R = NH_3/SiH_4 =10, 20, 40, and 60 at T_S = 400 °C are shown in Fig.3-7, and for samples with T_S = 100, 200, 400, and 550 °C at R = 40 to 60 are shown 3-8 as functions of photon energy E. Also shown in Fig.3-7 and 3-8 for comparison are the results of Philipp (1973) for a CVD a-Si_3N_4 film

which was essentially hydrogen-free. All the films studied here have values of n which are lower than that of the CVD film studied by Philipp, due to their lower densities resulting from the incorporation of hydrogen. Also, in Fig.3-9 and Fig.3-10, we can see that the refractive index n at 1.5 eV (see Table 3-2) increases with increasing substrate temperature T_S and decreasing gas ratio R. A further discussion will be given in chapter 5.

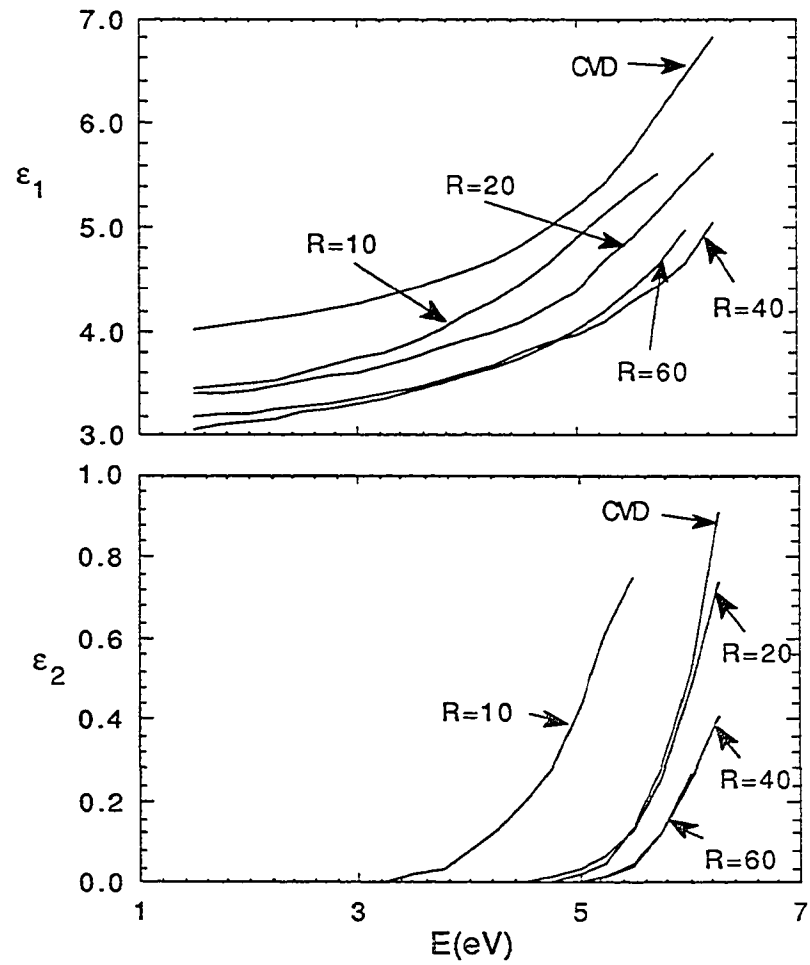

Fig.3-7 Real part ε_1 and imaginary part ε_2 of the optical dielectric function vs energy E for the samples (sample 1, 2, 3, and 8) prepared at R=10, 20, 40, and 60 and T_S=400°C. Also shown is Philipp's CVD a-Si_3N_4 film for comparison.

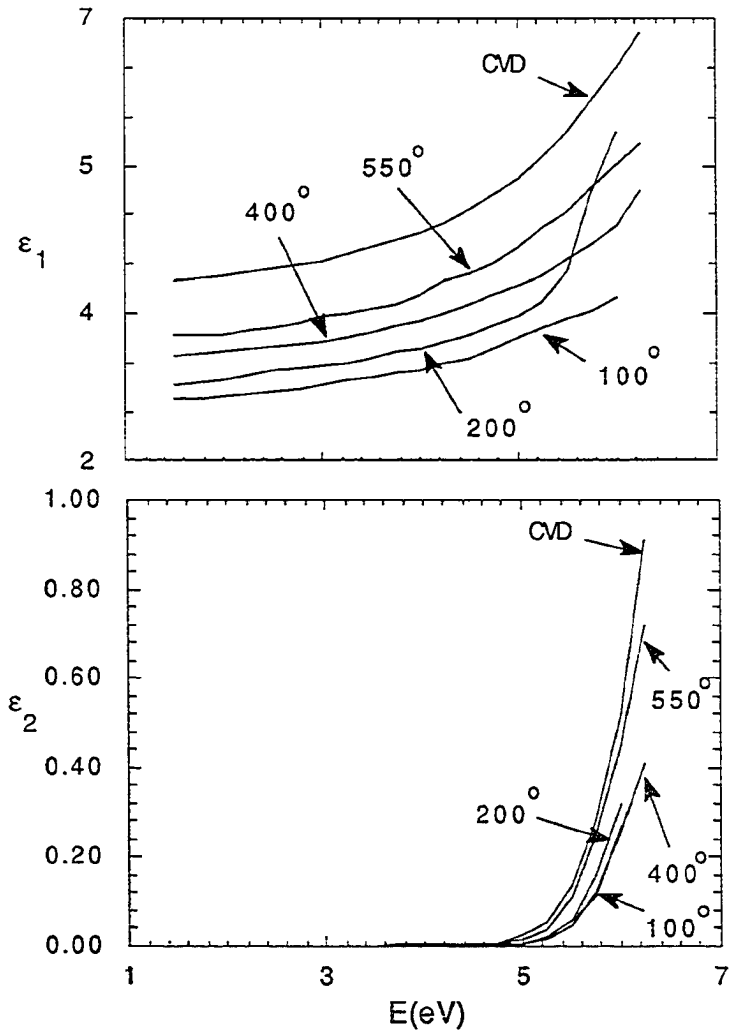

Fig.3-8 Real part ε_1 and imaginary part ε_2 of the optical dielectric function vs energy E for the samples (sample 9, 10, 3, and 11) prepared at T_S = 100, 200, 400, and 550 °C using R=40 to 60. For comparison, Philipp's CVD a-Si_3N_4 film data are included.

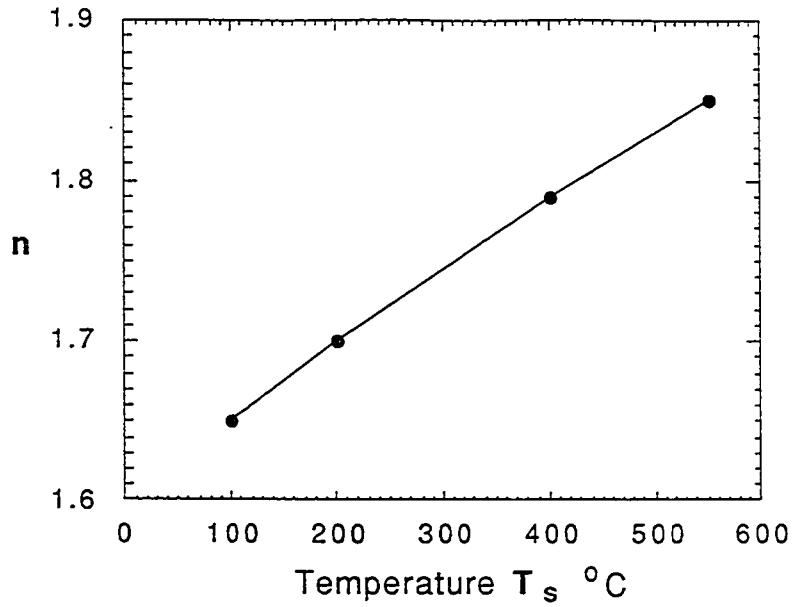

Fig.3-9 Refractive index n at 1.5 eV as a function of substrate temperature T_S for the a-$Si_xN_yH_z$ films studied (samples 3, 9, 10, and 11. R=40 and 60).

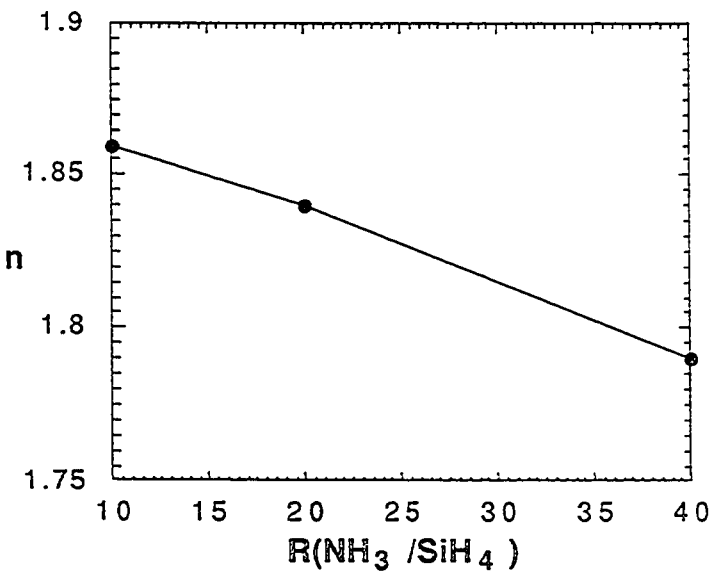

Fig.3-10 Refractive index n at 1.5 eV as function of reactant ratio R = NH_3 /SiH_4 for the a-$Si_xN_yH_z$ films studied (samples 1, 2, 3. T_S=400 °C).

Table 3-1A Real part of dielectric function e1 for the eleven films studied (see Table 2-1 for the deposition conditions for the films).

E (eV)	1	2	3	4	5	6	7	8	9	10	11
1.50	3.45	3.40	3.19	3.31	3.19	3.13	3.19	3.06	2.71	2.88	3.42
1.75	3.48	3.42	3.22	3.33	3.20	3.17	3.25	3.11	2.71	2.90	3.42
2.00	3.50	3.44	3.23	3.35	3.22	3.18	3.27	3.13	2.74	2.92	3.44
2.25	3.53	3.48	3.26	3.38	3.25	3.21	3.29	3.16	2.77	2.97	3.47
2.50	3.59	3.52	3.29	3.39	3.27	3.27	3.36	3.24	2.79	3.02	3.52
2.75	3.66	3.57	3.32	3.47	3.30	3.32	3.38	3.27	2.82	3.05	3.57
3.00	3.73	3.61	3.36	3.48	3.33	3.38	3.42	3.32	2.87	3.08	3.63
3.25	3.80	3.67	3.41	3.50	3.38	3.43	3.47	3.37	2.91	3.11	3.6
3.50	3.91	3.74	3.46	3.59	3.44	3.47	3.50	3.43	2.94	3.17	3.72
3.75	4.02	3.83	3.53	3.60	3.51	3.52	3.60	3.50	3.00	3.23	3.77
4.00	4.16	3.92	3.59	3.73	3.58	3.59	3.67	3.57	3.04	3.28	3.89
4.25	4.28	4.01	3.66	3.74	3.66	3.69	3.74	3.64	3.12	3.35	4.03
4.50	4.45	4.09	3.78	3.83	3.74	3.80	3.86	3.74	3.16	3.43	4.12
4.75	4.66	4.24	3.88	3.98	3.87	3.92	3.97	3.85	3.27	3.53	4.24
5.00	4.91	4.38	3.98	4.14	4.07	4.05	4.11	4.02	3.39	3.63	4.42
5.25	5.12	4.69	4.10	4.28	4.26	4.23	4.31	4.19	3.50	3.80	4.62
5.50	5.32	4.90	4.29	4.51	4.46	4.47	4.50	4.40	3.61	4.16	4.82
5.75	5.51	5.13	4.44	4.80	4.68	4.70	4.89	4.65	3.70	5.04	5.08
6.00	-	5.44	4.66	4.94	4.94	5.04	5.61	4.98	3.86	5.73	5.35
6.25	-	5.70	5.05	5.32	5.37	-	7.07	-	-	-	5.59

Typical uncertainty for ε_1 is ± 0.08.

Table 3-1B Imaginary part of dielectric function ε_2 for the eleven films studied (see Table 2-1 for the deposition conditions for the films).

E (eV)	1	2	3	4	5	6	7	8	9	10	11
1.50	0.000	0.000	0.000	0.000	0.000	0.000	0.000	0.000	0.000	0.000	0.000
1.75	0.000	0.000	0.000	0.000	0.000	0.000	0.000	0.000	0.000	0.000	0.000
2.00	0.000	0.000	0.000	0.000	0.000	0.000	0.000	0.000	0.000	0.000	0.000
2.25	0.001	0.000	0.000	0.000	0.000	0.000	0.000	0.000	0.000	0.000	0.000
2.50	0.003	0.000	0.000	0.000	0.000	0.000	0.000	0.000	0.000	0.000	0.000
2.75	0.004	0.000	0.000	0.000	0.000	0.000	0.000	0.000	0.000	0.000	0.000
3.00	0.003	0.000	0.000	0.000	0.000	0.000	0.000	0.000	0.000	0.000	0.000
3.25	0.003	0.000	0.000	0.000	0.000	0.000	0.000	0.000	0.000	0.000	0.000
3.50	0.018	0.000	0.000	0.000	0.000	0.000	0.000	0.000	0.000	0.000	0.000
3.75	0.041	0.000	0.000	0.000	0.000	0.000	0.000	0.000	0.000	0.000	0.000
4.00	0.077	0.001	0.000	0.000	0.000	0.000	0.000	0.000	0.000	0.000	0.000
4.25	0.127	0.001	0.000	0.000	0.000	0.000	0.000	0.000	0.000	0.000	0.000
4.50	0.199	0.003	0.000	0.000	0.000	0.001	0.000	0.000	0.000	0.001	0.001
4.75	0.296	0.013	0.001	0.000	0.002	0.003	0.000	0.001	0.001	0.002	0.004
5.00	0.453	0.030	0.004	0.004	0.012	0.010	0.008	0.004	0.004	0.005	0.012
5.25	0.620	0.066	0.015	0.015	0.034	0.033	0.029	0.014	0.017	0.018	0.036
5.50	0.753	0.134	0.047	0.045	0.091	0.080	0.079	0.045	0.056	0.058	0.107
5.75	-	0.263	0.121	0.126	0.195	0.180	0.190	0.123	0.108	0.155	0.252
6.00	-	0.481	0.262	0.284	0.366	0.354	0.447	0.267	0.269	0.318	0.452
6.25	-	0.740	0.408	0.551	0.632	-	0.674	-	-	-	0.724

Typical uncertainty for ε_2 is ± 0.002.

Table 3-2 Optical parameters of a-$Si_xN_yH_z$ films

sample	n [a] (at 1.5 eV)	E_o [b] (eV)	B [c] (cm eV)$^{-1}$	E_{Tauc} [c] (eV)	E_{opt} [d] (eV)	E_{04} [e] (eV)
1	1.86	0.27	425	3.83	3.83	4.10
2	1.84	0.28	715	5.14	5.05	5.32
3	1.79	0.20	740	5.28	5.20	5.55
4	1.82	-	880	5.46	5.42	5.63
5	1.78	-	745	5.28	5.27	5.46
6	1.77	0.18	665	5.21	5.23	5.48
7	1.78	-	715	5.26	5.26	5.48
8	1.75	0.20	650	5.27	5.24	5.62
9	1.65	0.16	585	5.13	5.54	5.57
10	1.70	0.20	570	5.16	5.24	5.56
11	1.85	0.22	785	5.27	5.37	5.46

[a]. Index of refraction at 1.5 eV; typical uncertainty is ± 0.02.
[b]. Urbach edge parameter; typical uncertainty is ±0.01 eV.
[c]. $(\alpha E)^{1/2} = B(E-E_{Tauc})$ where α = absorption coefficient; typical uncertainties for B and E_{Tauc} are ± 25 (cm eV)$^{-1}$ and 0.05 eV, respectively.
[d]. $E(\varepsilon_2)^{1/2} = B'(E-E_{opt})$; typical uncertainty for E_{opt} is ±0.05 eV.
[e]. E_{04} is the energy corresponding to absorption coefficient $\alpha = 10^4$ cm^{-1}; typical uncertainty is ±0.05 eV.

It has been observed here that ε_1 and ε_2 are essentially independent of pressure at T_s = 400 °C , R = 40, and power density of 0.43 W/cm^2. Also, we have observed that thinner a-$Si_xN_yH_z$ films have higher values of n than thicker films prepared under the same conditions. We believe that this is due to the existence of enhanced concentrations of Si-centered tetrahedra containing Si-Si bonds near the film-substrate interfaces, Such tetrahedra would lead to higher n

values (see details in chapter 6) and it is clear that this effect would be more important for thin films.

Optical absorption edges for R = 10, 20, and 40 films are shown in Fig.3-11 and again the result of Philipp for the CVD a-Si_3N_4 film is shown for comparison. The Urbach edge parameter E_o and the optical energy gaps E_{opt} and E_{04} are given in Table 3-2. It can be seen that the optical absorption edge shifts to higher energies with increasing gas ratio R. This is due to stronger Si-N bonds replacing weaker Si-Si bonds in the films (see next chapter for the bond concentrations). This behavior has been observed previously (Ibaraki et al, 1984; Dunnett et al,1986).

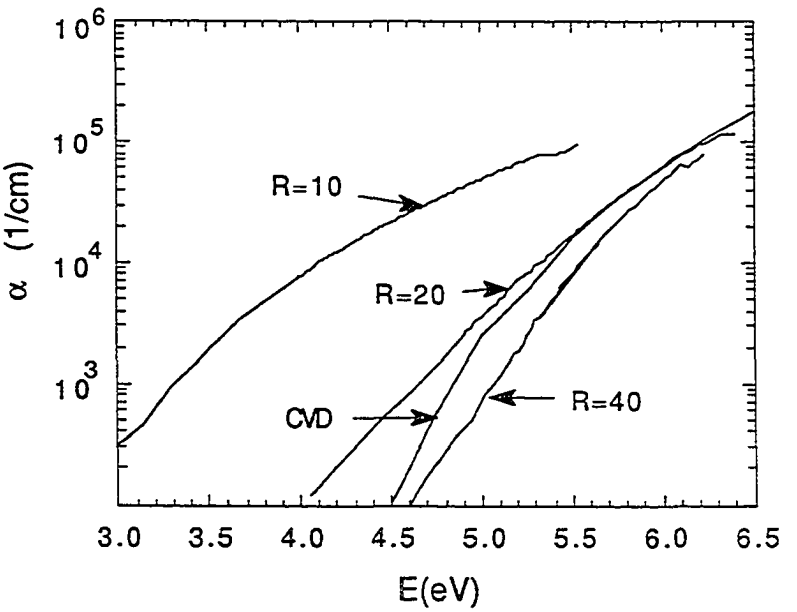

Fig.3-11 Optical absorption edges for a-$Si_xN_yH_z$ films prepared at R = 10, 20, and 40 and T_s=400°C for samples 1, 2, and 3 and for Philipp's CVD a-Si_3N_4 film.

It is noted that ε_1 was not affected significantly by change of the power density from 0.12 to 0.63 W/cm^2 at constant R = 60, T_s = 400 °C, and pressure = 0.5 Torr. According to D. L. Smith' studies (Smith et al, J. Electrochem. Soc., 1990) of the radicals in NH_3-SiH_4 plasmas, only disilane, Si_2H_6, was produced at low power density (below 0.01 W/cm^2 at R = 25). With increasing power, silane and disilane decreased while triaminosilane, $Si(NH_2)_3$, rose linearly and then abruptly levelled off above 0.06 W/cm^2, which was named the power "saturation" regime by Smith et al. The reaction which takes over in the power saturation regime for NH_3-SiH_4 plasmas is the reaction leveling to aminosilanes, $SiH_{4-n}(NH_2)_n$, consuming 98% of silane and preventing the formation of disilane. The parameter which determines the dominant reaction is not only the power, but also the silane flow rate. In our study of the effect of power, the silane flow rate was 4 sccm and the power was varied from 0.12 to 0.63 W/cm^2. Therefore, the plasma may be already in the power saturation regime so that we did not observe strong effects of power density on ε from our experiment. More discussion will be given in chapter 5.

Chapter 4 Infrared Absorption of a-$Si_xN_yH_z$ and a-$Si_xO_yH_z$ Films

4.1 Introduction

Infrared (IR) spectroscopy is a convenient and popular technique for studying the microscopic structure and bonding present in a material simply because the different bonding units have different fingerprints in the infrared absorption spectrum. The ability to absorb infrared energy depends on a net change in dipole moment, i.e. the change of the distribution of electrical charges, occurring when the molecule vibrates. Furthermore, since in the molecule different types of vibrations exist, they will correspond to different bands in the infrared spectrum. The terminology for different vibration modes which is used very often are stretching, bending, rocking, and wagging mode (Kendall, 1966). As shown in Fig.4-1, a stretching vibration is the back and forth motion along the valence bond of two or three atoms. When two like atoms bond to the same central atom and move in phase along their valence bonds, it is called symmetric stretching (see Fig.4-1A) and when out of phase, it is called asymmetric stretching (see Fig.4-1B). One specialized type of stretching vibration is the so-called breathing vibration. This is a completely symmetric stretching vibration usually found in ring compounds. A bending vibration is a motion across the valence bond between atoms, i.e. the vibration has internal changes of angle between bonds (see Fig.4-1C). A wagging vibration results when the atomic grouping, which has no internal changes of angle and moves as a rigid unit with respect to the

remainder of the molecule, swings back and forth in a plane perpendicular to the molecule's symmetry plane (see Fig.4-1D). A rocking vibration is similar to the wagging type except the atomic grouping concerned swings as a unit back and forth in the symmetry plane of the molecule (see Fig.4-1E).

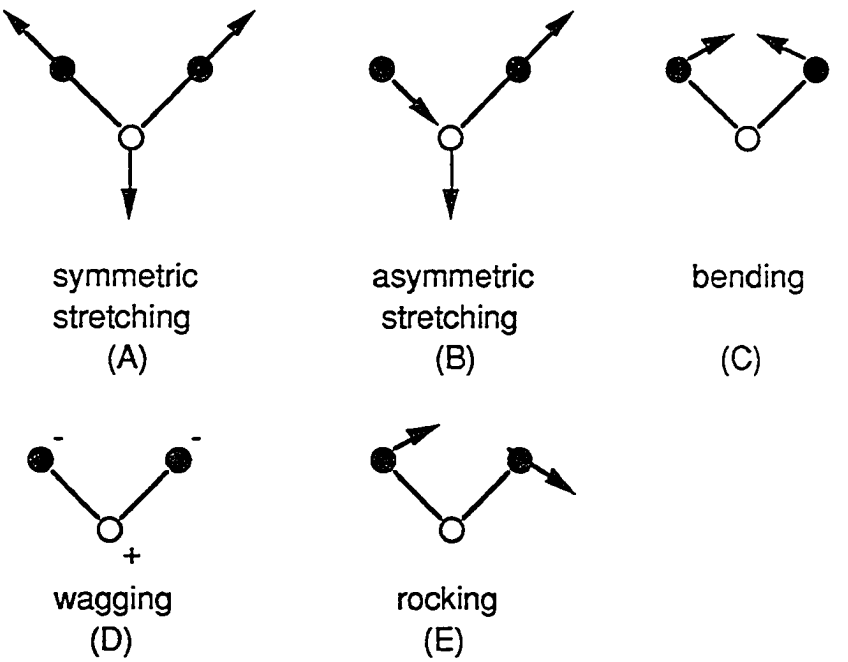

Fig.4-1 The definitions for the vibration modes.

The band intensities of infrared absorption are intimately tied up with changes in electron configuration during the vibration. In the first approximation, the basic relationship (A. L. Smith, 1979) between observed intensities and the dipole moment of bond μ is:

$$\int \alpha(\nu) d\nu = \frac{N\pi}{3c^2}\left(\frac{\partial \mu}{\partial Q}\right)^2 \qquad (4\text{-}1)$$

where $\alpha(\nu)$ is the absorption coefficient at wave number ν, N is the number of absorbing molecules per cubic centimeter of sample, Q is the normal coordinate for the vibration, and c and π have their usual meaning. Mathematical descriptions of the phenomenon are very complicated. Although some calculations of absorption intensities have been carried out, they are too crude to be valuable. Therefore, empirical correlations of intensity with structure, in other words the cross section for infrared absorption, are used in practice.

To do quantitative analysis of infrared absorption, the basic theory is given by the Lambert-Beer-Bouguer law, often called simply Beer's law (van der Maas, 1972). Beer's law states that the relation between the amount of light from a monochromatic beam that passes through an absorbing medium and the amount of the absorbant present is given as follows when the reflection of the beam can be ignored:

$$I = I_o \exp (- kCd) \qquad (4\text{-}2)$$

where I is the transmitted intensity, I_o the intensity of the radiation incident on the absorbant, C the concentration of the absorbant, d the thickness of the sample, and k a conversion constant related to the absorptive power of the sample. The formula can be transformed into :

$$\log \frac{I}{I_o} = - \frac{kCd}{2.303} \qquad (4\text{-}3)$$

where $\log e = \frac{1}{2.303}$ was used.

Frequently, the absorbance A is used for $\log \frac{I_o}{I}$. Thus, eqn.(4-3) can be written as:

$$A = \frac{kCd}{2.303} \qquad \text{or} \qquad C = \frac{1}{k}\alpha \qquad (4\text{-}4)$$

where $\alpha = \frac{2.303\ A}{d}$ is the absorption coefficient.

In practice, however, the infrared absorption due to a bond is broadened out over a wavenumber region. There are two most important factors causing this broadening: the limited resolution of available instruments, due to the finite slit width, and the interactions of neighboring molecules which cause a distribution of vibration frequencies. Since finite slit widths are used in real situations, the apparent band is broadened and less intense than the true band. In other words, the shape of the absorption band depends on the setting of slit width for the instrument. Fortunately, it is found that the band area, i.e. the integrated absorbance, is more or less independent of the slit width and is thus a more suitable value for quantitative analysis. The vibration frequencies are dependent on the complete force field and the magnitudes of the masses involved. The relation between bond concentration, N(X-Y), and the absorbance of the X-Y bond vibration is usually written as:

$$N(X\text{-}Y) = K(X\text{-}Y) \int \alpha(\nu) d\nu \qquad (4\text{-}5)$$

The wave-number integral of the absorption coefficient α over the band in question gives the normalized area of the band. K(X-Y) is a

empirical constant for the X-Y vibration type. The IR absorption cross section, $\sigma = 1/K(X\text{-}Y)$, is used very often and also will be used in the following text. It is not unreasonable to expect that the cross section of infrared absorption for X-Y bonding vibration will be affected by the surrounding environment of the bonding. Thus, the accuracy of the K value limits the accuracy of quantitative analysis of infrared absorption. Nevertheless, quantitative analysis of infrared absorption is still used widely in scientific research.

In our study of a-$Si_xN_yH_z$, the bands used for bond concentrations are the 3320 cm^{-1} N-H (stretching) band, the 2180 cm^{-1} Si-H (stretching) band, and the sum of the Si-N (stretching) bands near 880 and 1030 cm^{-1}. Values of $K(N\text{-}H) = 8.2 \times 10^{16}$ cm^{-1} and $K(Si\text{-}H) = 5.9 \times 10^{16}$ cm^{-1} have been obtained from the results of Lanford and Rand (1978).* These K values are commonly used for

---

* Lanford and Rand express the concentration of hydrogen atom per unit area as:

$$H/cm^2 = \frac{1}{\sigma} \text{ Area} \qquad (1)$$

$$\text{Area} = A \, \Delta \nu_{A/2}$$

where A is absorbance, $\Delta \nu_{A/2}$ is bandwidth (cm^{-1}) at half absorbance, and σ is the absorption cross section (cm) which is 7.4×10^{-18} cm for Si-H and 5.3×10^{-18} cm for N-H as given by Lanford and Rand.

According to eqn.(4-5), we can write :

$$H/cm^2 = K(X\text{-}Y) \int 2.303 A d\nu \approx 2.303 \, K(X\text{-}Y) \text{ Area} \qquad (2)$$

After comparing (1) and (2), we get:

$$\frac{1}{\sigma} = 2.303 \, K(X\text{-}Y)$$

or $$K(X\text{-}Y) = \frac{1}{2.303\sigma} \qquad (3)$$

When the values of σ given above are substituted into (3), we get $K(Si\text{-}H) = 5.9 \times 10^{16}$ cm^{-1} and $K(N\text{-}H) = 8.2 \times 10^{16}$ cm^{-1}.

calculation of the N-H and Si-H bond concentrations. However, different values of K(Si-N) for Si-N bands have been obtained by different people. This may be caused by the change of the surrounding environment for the Si-N bond, which affects the change of dipole moment occurring when the Si-N bond vibrates. For example, K(Si-N) for films with low [N]/[Si] ratios ($y/x < 0.9$) has been estimated to be in the range (0.9 to 1.0) $\times 10^{16}$ cm^{-1} by Yadav et al and other workers (Yadav and Yoshi, 1979; Chayahara et al, 1985; Hasegawa et al, 1987). For nearly stoichiometric films, however, K(Si-N) = 2.4×10^{16} cm^{-1} has been obtained by Bustarret et al, (1988). Therefore, an alternative approach to obtaining N(Si-N) and hence, K(Si-N), will be introduced in chapter 5.

Other than the bond concentrations for our sample, we also used the infrared measurement to study the annealing behaviors and to investigate hydrogen bonding. The results of our experiments will be given in the following section.

4.2 Infrared Spectra of a-$Si_xN_yH_z$

The IR absorption spectra for all the films studied are shown in Fig.4-2A, B, C, and D in the range from 400 to 4000 cm^{-1}. In order to remove the interference effects in the films, a computer fitting procedure of baseline correction has been carried out by fitting the remaining spectrum after eliminating the absorption band portion, such as a-b, c-d, and e-f portion in Fig.4-2B for sample 1, to the function $a_0 + a_1\sin(a_2v + a_3)$ where the a_i are fitting parameters. The IR absorption spectra for the R=10 and R=40 films prepared at T_s =

400 °C, power = 0.43 W/cm^2, and P = 0.5 Torr after baseline correction are shown in Fig.4-3. Absorption bands for the N-H (stretching) mode have been observed near 3320 cm^{-1}, for Si-H (stretching) near 2180 cm^{-1}, for H-N-H (bending) near 1550 cm^{-1}, for N-H (bending) near 1180 cm^{-1}, for Si-N (stretching) near 880 cm^{-1}, and for Si-N (breathing) near 480 cm^{-1}. The weak features seen near 2320 cm^{-1} result from an incomplete subtraction of the absorption due to CO_2 in the spectrophotometer sample chamber.

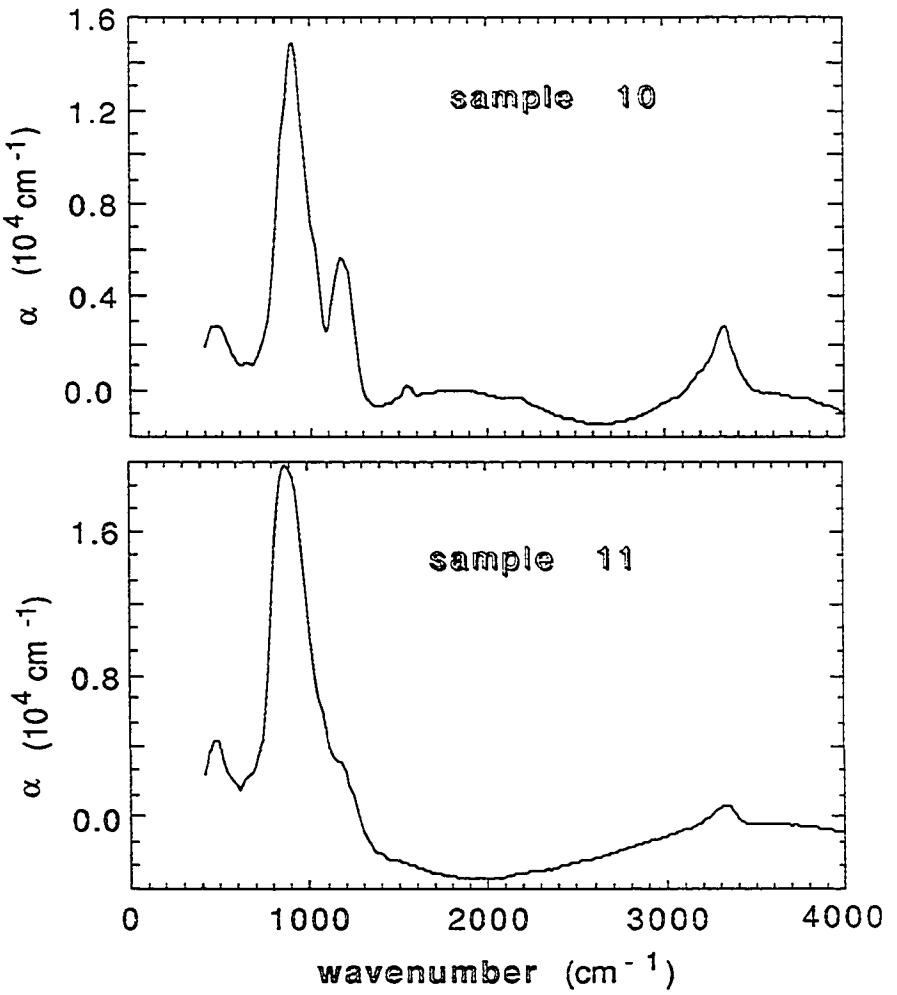

Fig.4-2A Measured absorption coefficients for samples 10 and 11.

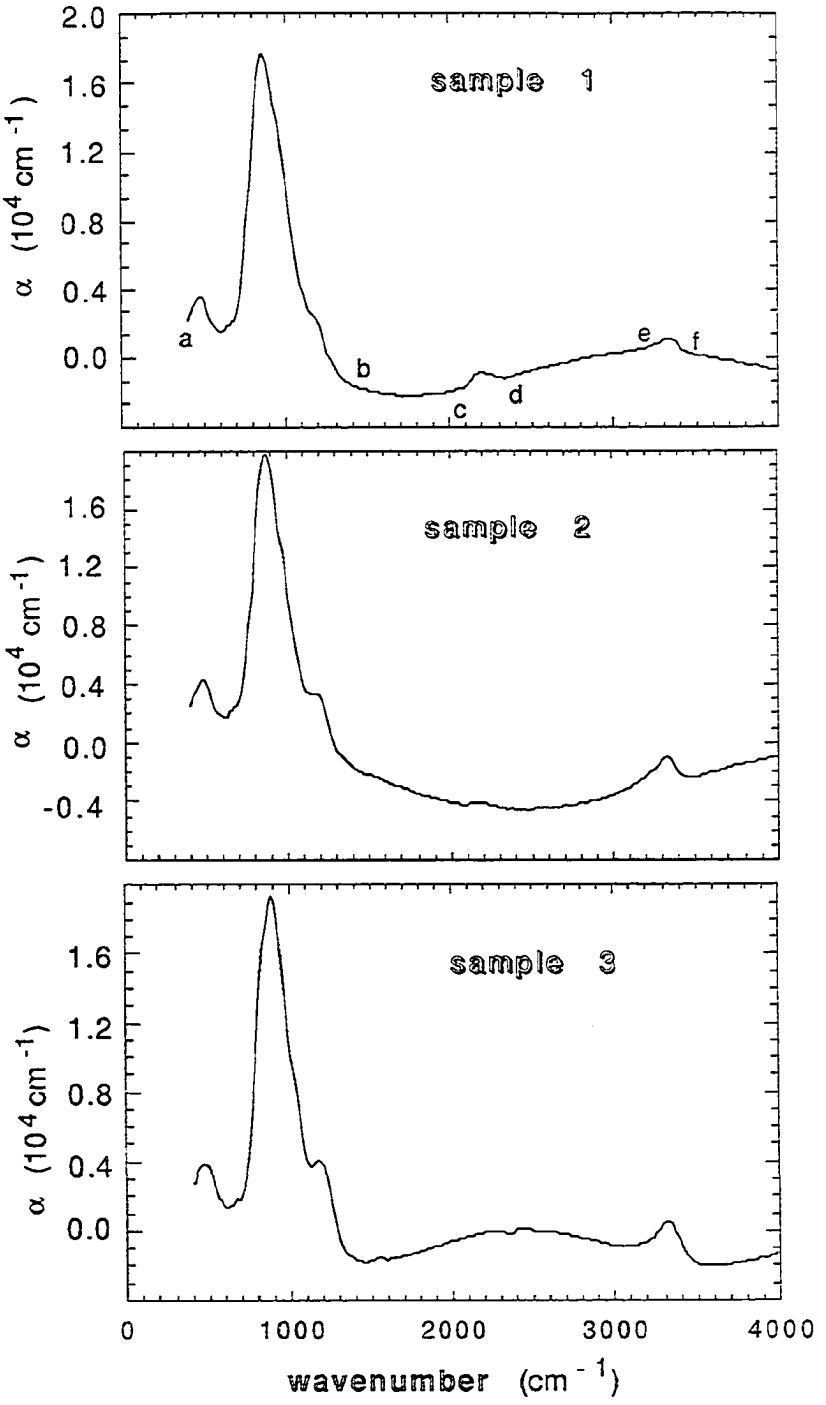

Fig.4-2B Measured absorption coefficients for samples 1, 2, and 3.

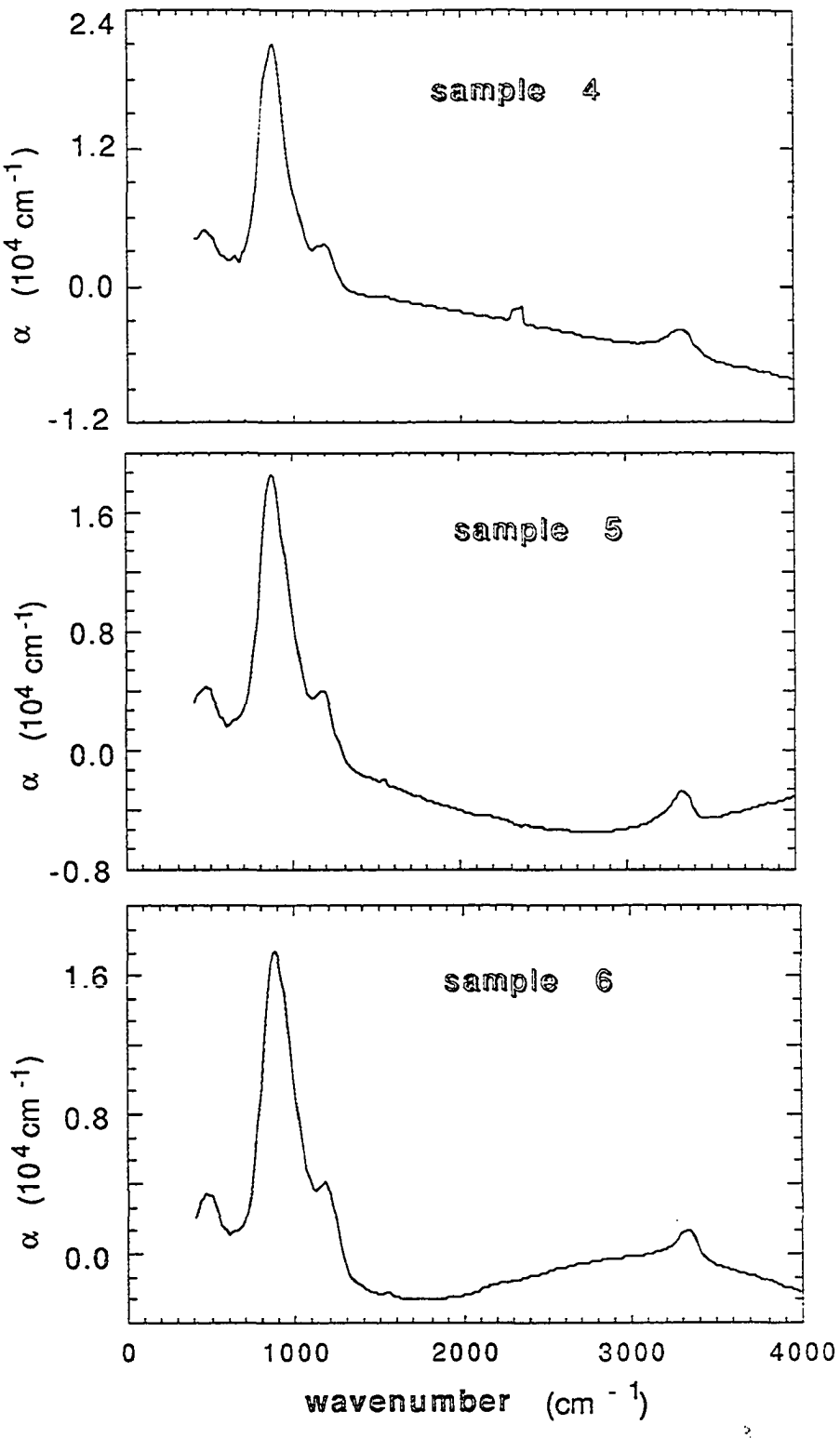

Fig.4-2C Measured absorption coefficients for samples 4, 5, and 6.

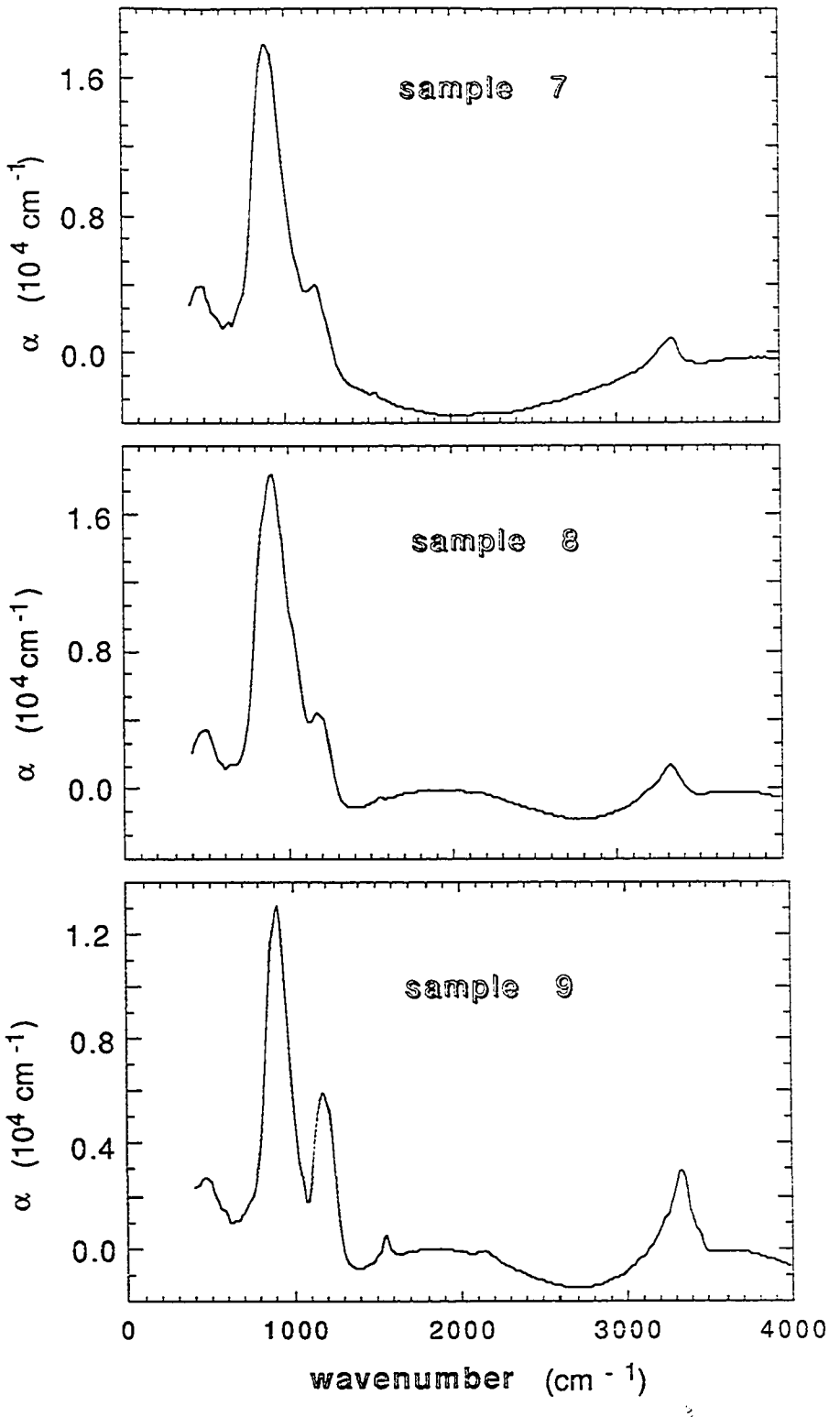

Fig.4-2D Measured absorption coefficients for samples 7, 8, and 9.

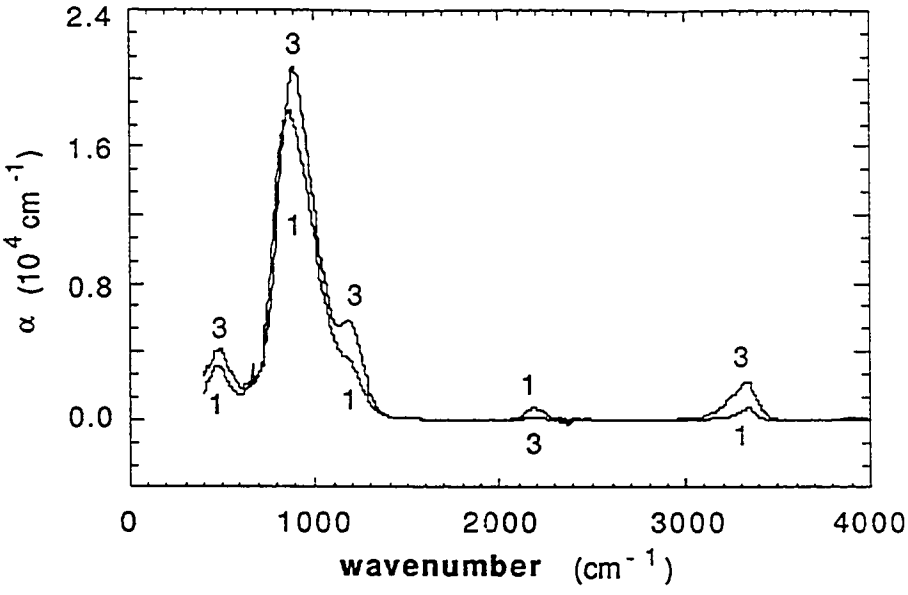

Fig.4-3 Absorption coefficients for sample 1 and sample 3 (see Table 2-1 for deposition conditions) after baseline corrections.

Evidence for the Si-H (stretching) absorption near 2180 cm^{-1} has been observed only in the films prepared with the SiH_4 flow rate greater than or equal to 4 sccm. The Si-H absorption band appears to consist of two sub-bands near 2170 and 2250 cm^{-1}, which is consistent with Si-H (stretching) absorption arising from $Si\text{-}HN_2Si$ and $Si\text{-}HN_3$ tetrahedra, respectively (Lucovsky, 1979).

In order to accurately determine the absorbances of the N-H (bending) band near 1180 cm^{-1} and the Si-N (stretching) band near 880 cm^{-1}, it has been necessary to carry out deconvolutions of the broad region of absorption extending from 400 to near 1500 cm^{-1}. For this purpose, five Gaussian absorption bands have been employed, centered near 1180, 1030, 880, 640, and 480 cm^{-1}. An example of the deconvolution for the R=40 and P=0.5 Torr film is shown in Fig.4-4. There is only one absorption feature in this region

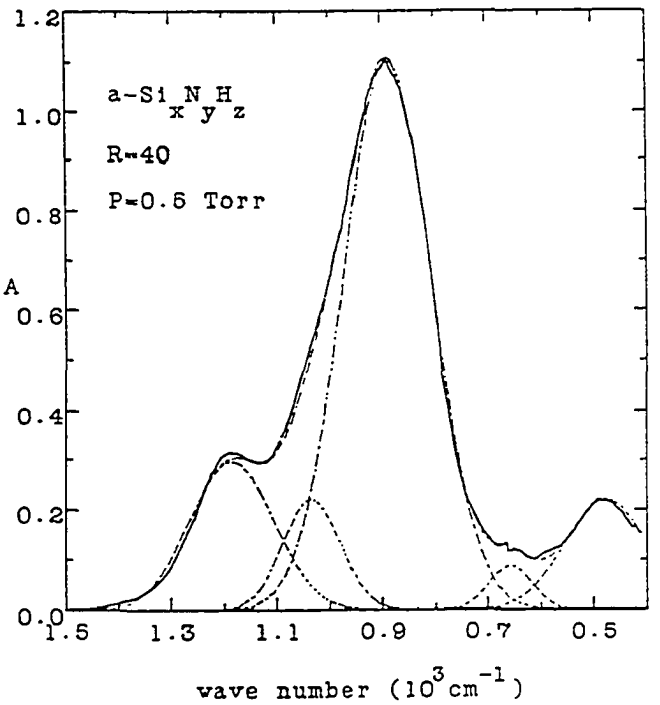

Fig.4-4 Absorbance A vs wave number for sample 3. The solid curve is the experimental result, while the dashed curve are the individual fitted absorption bands and their sum.

which is clearly hydrogen-related, namely the N-H (bending) band near 1180 cm^{-1}. The absorption band centered near 1030 cm^{-1} is proposed to be a shoulder on the main Si-N (stretching) band near 880 cm^{-1}. The small absorption feature consistently observed for these films near 640 cm^{-1} would normally be assumed to be due to Si-H (rocking, wagging) modes (Cardona, 1983). But this cannot be the complete explanation here since this feature has been observed in the films prepared at SiH_4 flow rate lower than 4 sccm for which there is no evidence for absorption due to the Si-H (stretching) mode near 2180 cm^{-1}. In addition, annealing experiments (see section 4.3) have shown that, as the hydrogen is driven out of the film via heating up to 1000 °C, no significant changes are observed to occur in

the 640 cm^{-1} absorption. We propose instead that this absorption band is due to a vibration of the N-Si_3 bonding units which appears near 680 cm^{-1} for α-Si_3N_4 (Volgin et al, 1975). In this case, the pattern of three absorption bands (near 880, 640, and 480 cm^{-1}) for Si-N-Si in a-$Si_xN_yH_z$ is similar to the bands (near 1070, 800, and 450 cm^{-1}) for the Si-O-Si bonding units in a-SiO_2 films (Ericksson and Granqvist, 1986).

The results derived from the infrared absorption spectra, such as peak wave numbers ν(peak), maximum absorption coefficients α(max), full widths at half maximum (FWHM), and normalized absorption band areas $\int \alpha d\nu$ for these bands, are listed in Table 4-1 for the films we studied along with the results for absorption bands which have been identified as being present near 1030 and 640 cm^{-1} from deconvolutions of the main absorption band.

Table 4-1 Infrared absorption results for a-$Si_xN_yH_z$ films.

Sample	Si-N				N-H and Si-H (in parentheses)			
	ν [a] (peak) (cm^{-1})	α [b] (max) (cm^{-1})	FWHM[c] (cm^{-1})	$\int\alpha d\nu$ [d] (cm^{-2}) $\times10^5$	ν [a] (peak) (cm^{-1})	α [b] (max) (cm^{-1})	FWHM[c] (cm^{-1})	$\int\alpha d\nu$ [d] (cm^{-2}) $\times10^4$
1	877	18300	223	43.50	3340	810	141	13.6
	1035	2860	103	3.13	1163	3520	206	77.2
	478	3150	175	5.85	1543	60	32	0.18
	631	838	63	0.55	(2184	750	139	11.0)
2	877	20200	197	42.35	3317	1860	177	38.9
	1034	3850	120	4.91	1178	4120	184	80.6
	487	3700	140	5.53	1547	160	38	0.649
	644	1230	76	0.99	(2182	310	153	4.93)
3	888	20400	196	42.42	3336	2290	163	44.7
	1034	4750	130	6.56	1185	5540	178	104.8
	476	4060	183	7.92	1546	190	42	0.824
	656	1640	104	1.80	-	-	-	-
4	868	20700	169	37.19	3325	2310	189	51.8
	1022	4310	125	5.73	1181	3620	158	61.0
	475	3790	178	7.16	1551	180	46	0.880
	661	1400	96	1.43	-	-	-	-
5	881	17971	113	36.13	3337	2233	153	42.2
	1034	3037	55	2.96	1174	4610	103	83.9
	466	1734	92	2.84	1550	326	41	1.33
	-	-	-	-	(2183	187	131	2.93)
6	890	18546	125	40.94	3337	1807	143	31.8
	1040	2850	53	2.68	1179	5834	109	112.5
	479	3575	108	6.82	1543	319	44	1.40
	647	1112	51	1.01	(2172	191	135	2.74)
7	882	19141	118	40.06	3333	1890	158	38.9
	1030	3502	61	3.79	1175	5669	116	116.2
	472	4206	119	8.86	1543	332	147	1.56
	655	1336	59	1.51	(2172	199	138	3.08)

8	901	20027	133	47.05	3321	2179	201	54.2
	1045	2625	53	2.45	1183	5760	100	102.3
	484	3880	121	8.31	1543	250	51	1.28
	657	1374	53	1.29	(2199	102	157	1.73)
9	903	14223	93	23.34	3336	3420	163	74.1
	1022	3071	51	2.79	1180	7285	87	112.7
	472	3131	156	8.64	1547	958	48	4.60
	722	2135	89	3.36	(2156	232	124	3.27)
10	896	15831	106	29.60	3333	2862	167	61.7
	1023	3686	62	4.06	1182	6865	88	106.8
	486	3115	130	7.15	1547	588	49	2.88
	697	1898	76	2.57	(2172	183	142	2.85)
11	876	21126	122	45.57	3332	1197	158	23.9
	1028	4503	81	6.50	1173	4582	126	102.7
	481	4520	101	8.05	1543	157	- 57	0.89
	646	1774	53	1.67	2191	154	138	2.32)

[a] Peak wave number of absorption band; typical uncertainty is ±5 cm^{-1}.

[b] Maximum absorption coefficient of absorption band; typical uncertainty is ±4 %.

[c].Full width at half maximum of absorption band; typical uncertainty is ±4 cm^{-1}.

[d] Normalized absorption band area $\int \alpha d\nu$, where $\alpha = (2.303/d)A$ is the absorption coefficient, d is the film thickness, and A the absorbance; typical uncertainty is ±5%.

* The symbol of '-' means the corresponding peak is not observed.

It can be seen clearly in Fig.4-5 that the substrate temperature T_S affects the bonds present in the film. At low T_S (≤ 200 °C), many N-H or $N-(H)_2$ units are present in the film. These units decrease in concentration as the substrate temperature increases (up to 550 °C). Also, in the films which were prepared at higher gas ratios R = 40

and 60, evidence can be seen in Fig.4-6 for increasing absorption due to stretching modes of the N-$(H)_2$ unit between 3400 and 3500 cm^{-1} (Narikawa, et al, 1985). The spectrum for the film prepared at R=10 is also shown in Fig.4-6 for comparison. The presence of the N-$(H)_2$ stretching mode is not observed for this low hydrogen content sample. In the same films, the H-N-H (bending) absorption band near 1550 cm^{-1} is also observed to be stronger, as shown in Fig.4-7. These results are consistent with those of previous studies (Tsu, et al, 1986; Lucovsky and Tsu, 1987).

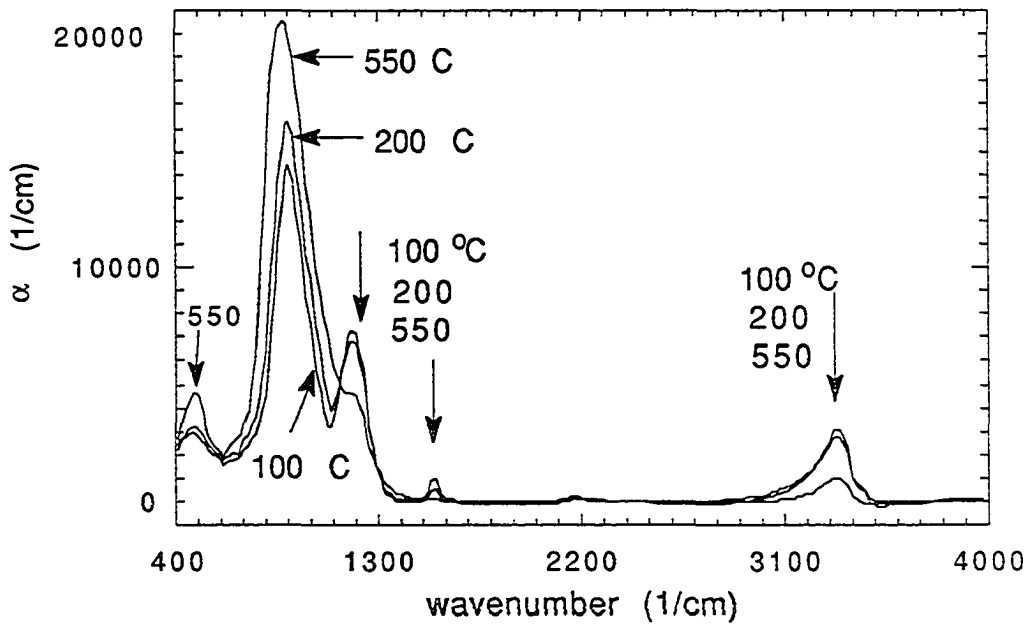

Fig.4-5 Absorption coefficien: for samples 9, 10, and 11 prepared at substrate temper res T_s = 100, 200, and 550 °C, respectively. (after baselin correction).

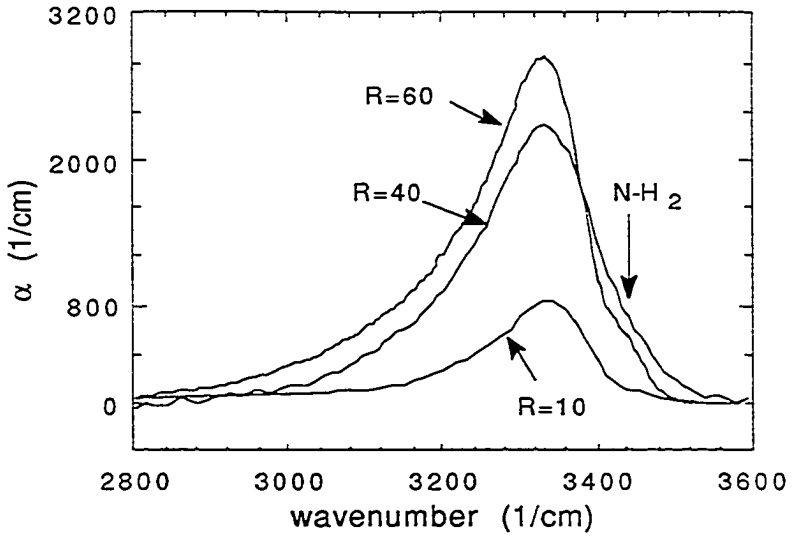

Fig.4-6 Absorption coefficient for N-H (stretching) band for the samples prepared at reactant ratio R=60 (sample 10), R=40 (sample 4), and R=10 (sample 1). The shoulder in the region from 3400 to 3500 cm^{-1} corresponds to N-$(H)_2$ stretching modes.

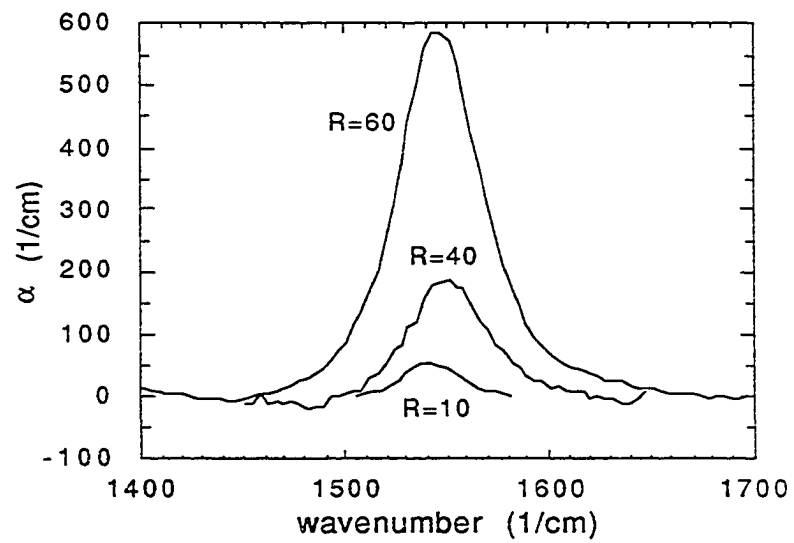

Fig.4-7 Absorption coefficient for N-$(H)_2$ (bending) bands for the samples prepared at reactant ratio R=60 (sample 10), R=40 (sample 4), and R=10 (sample 1).

It is important to note here that, for a given alloy, measurable changes in the peak position, full widths at half maximum (FWHM), and maximum absorption coefficients $\alpha(max)$ of the main Si-N (stretching) band have been observed for films of different thickness prepared under identical conditions. We found that the Si-N (stretching) peak positions are about 20 cm^{-1} higher for thick films (d = 0.5 ~ 1.0 μm) than for thinner films (d = 0.1 ~ 0.2 μm). The FWHM's for the thicker films are greater by 20-40 cm^{-1} than the FWHM's for the thinner films and $\alpha(max)$ of the thicker films are lower than the $\alpha(max)$ of the thinner film. However, the normalized Si-N (stretching) absorption band areas have been found to be independent of film thickness, to within experimental error (±5%), for the films studied. Thus, the areas of the Si-N (stretching) bands can be used, in principle, to determine bond concentrations for these films.

One example is given in Fig.4-8 for two films prepared under same conditions of R=10, P=0.5 Torr, T_s = 400 °C, and power = 0.43 W/cm^2 with different thicknesses (one is 9800 Å and the other is 1373 Å). It can be seen that the Si-N band shifts to higher wavenumber by 20 cm^{-1}, is broader by 36 cm^{-1}, with a 25% decrease of $\alpha(max)$ when the thickness changes from 1373 Å to 9800 Å. It is clear, however, that correlations of parameters such as index of refraction n with the peak wave number of the Si-N (stretching) band are valid only when carried out for films of comparable thickness. The observed shifts in $\nu(peak)$ and $\alpha(max)$ with film thickness are due to changes in film reflectance (Philipp, 1979)

resulting from the strong absorption of the Si-N (stretching) mode. Therefore, films with comparable thicknesses should be used to minimize this effect.

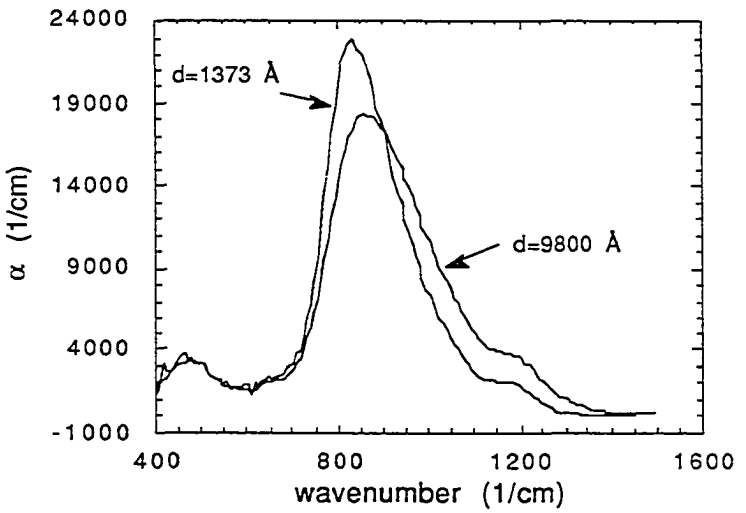

Fig.4-8 Absorption coefficient of Si-N bands for films prepared at R=10, P=0.5 Torr, T_S=400, and power=0.43 W/cm^2 for thickness 1373 and 9800 Å.

It should also be noted that the samples prepared at T_S = 400°C are very stable since no evidence in the infrared spectra has been found for the diffusion of either O_2 or H_2O into the films during the period of 17 months following their initial exposure to the atmosphere. This observation indicates that these films can be prepared with very low porosities. For the sample prepared at T_S = 100 °C, however, evidence of absorbing O_2 or H_2O was observed in infrared measurements after exposure to the atmosphere for only about 2 days. Only very little change was observed, however, for the sample prepared at T_S = 200 °C. Fig.4-9 shows the change of the spectrum for the sample prepared at T_S = 100 °C. In Fig.4-9B, the

change of the spectra ΔA (A(after exposure) - A(as deposited) is shown, which clearly indicates the growth of intensity in the region 1070 cm^{-1} corresponding to the vibration of Si-O (stretching).

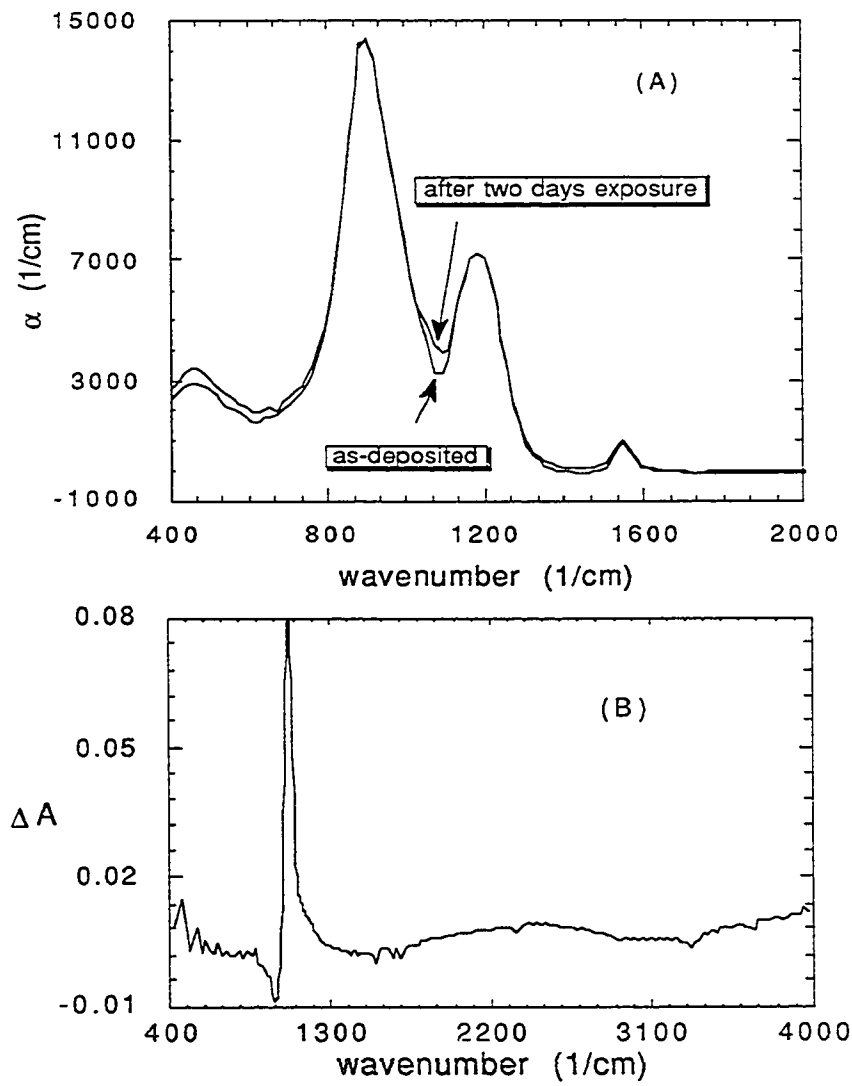

Fig.4-9 (A) Infrared spectra (in range 400 to 2000) obtained right after deposition and after two days exposure in air for the film prepared at T_S=100°C, R=60, P=0.5 Torr, and power=0.43 W/cm^2. (B) The difference of the above two spectra, i.e., ΔA = A(after exposure) - A(as-deposited). The sharp peak corresponds to the absorption of the Si-O band.

4.3 Hydrogen Bonding and Annealing Behavior in a-$Si_xO_yH_z$ and a-$Si_xN_yH_z$ alloys

As we saw in chapter 3, the incorporation of hydrogen atoms into silicon nitride causes the real part of the dielectric function ε_1 to shift to lower values and imaginary part of the dielectric function ε_2 to shift to higher energy. In addition, hydrogen bonding is another role that hydrogen atom can have in amorphous materials. The notation of the hydrogen bond is usually written as A-H· · ·B. The criteria (Vinogradov and Linnell, 1971) for the formation of hydrogen bonds are as follows: (1) There has to be a proton donor group A-H, where A is a strongly electronegative atom such as O, N, or F. This means that the electrons of the A-H bond are not equally shared by the two atoms, but distributed more towards the A atom side. Then the net positive charge on the H atom side forms a H-bond donor. (2) A proton acceptor group B has to have lone pair electrons in an asymmetric orbital. That means the H atoms with net positive charge will be attracted to the regions which have large electron density such as the region of the lone pair electrons on atom B.

Infrared absorption is a very important tool for investigating hydrogen bonding. The effects of hydrogen bonding in the infrared region are as follows: (1) The A-H stretching vibrations are shifted to lower frequencies, which is due to the weakening of the force constant for the A-H bond caused by the formation of the hydrogen bond. (2) The shifted absorption bands corresponding to the hydrogen bonded A-H stretching vibrations are much broader than

the corresponding bands of the non-hydrogen bonded A-H group. In other words, the infrared absorption cross section is greater for the hydrogen-bonded A-H group than for the isolated A-H group. (3) The A-H bending modes are shifted to higher frequencies but do not change in width and intensity when hydrogen bonding occurs. The effects of hydrogen bond formation found for the A-H bending modes are smaller than those for the A-H stretching vibration. Thus, the A-H stretching vibrations have been more widely investigated in hydrogen bonding studies than any other effect.

According to the criteria for the formation of hydrogen bonds, it is very likely to have hydrogen bonding present in a-$Si_xO_yH_z$ and a-$Si_xN_yH_z$ alloys due to the presence of O-H and N-H groups and O and N atoms which have lone pair electrons. In order to investigate the hydrogen bonding in these alloys, the temperature-dependence and annealing behavior of the infrared absorption have been studied from liquid N_2 temperature (77 °K) up to 350 °C.

The a-$Si_xO_yH_z$ film studied was prepared by D. Tsu at North Carolina State University via remote plasma-enhanced CVD at 140°C deposition temperature and a total pressure of 0.3 Torr. A mixture of 20% O_2 in He flowing at 100 sccm was plasma-excited and mixed downstream with 10% SiH_4 in He at 10 sccm, deposition taking place onto high-resistivity crystalline Si. The absorption spectra of the film measured at 25 °C before annealing and also following anneals at 150, 250, and 350 °C are shown in Fig.4-10. The absorption modes of Si-O-Si bonding units were observed near 1070, 800, and 450 cm^{-1} (Fig.4-10A), while H-related absorptions were found in the region

from 3000 to 3700 cm^{-1} (O-H stretching) (Fig.4-10B) and also near 1150 and 925 cm^{-1}, the latter corresponding to the stretching mode of Si-O-H units (Pliskin, 1977; Lucovsky et al, 1987). From the area of the O-H (s) band and assuming a film density of 2.2 g/cm^3, the approximate composition of the film before annealing was found to be $a\text{-}Si_{0.31}O_{0.64}H_{0.05} = a\text{-}SiO_{2.08}H_{0.16}$.

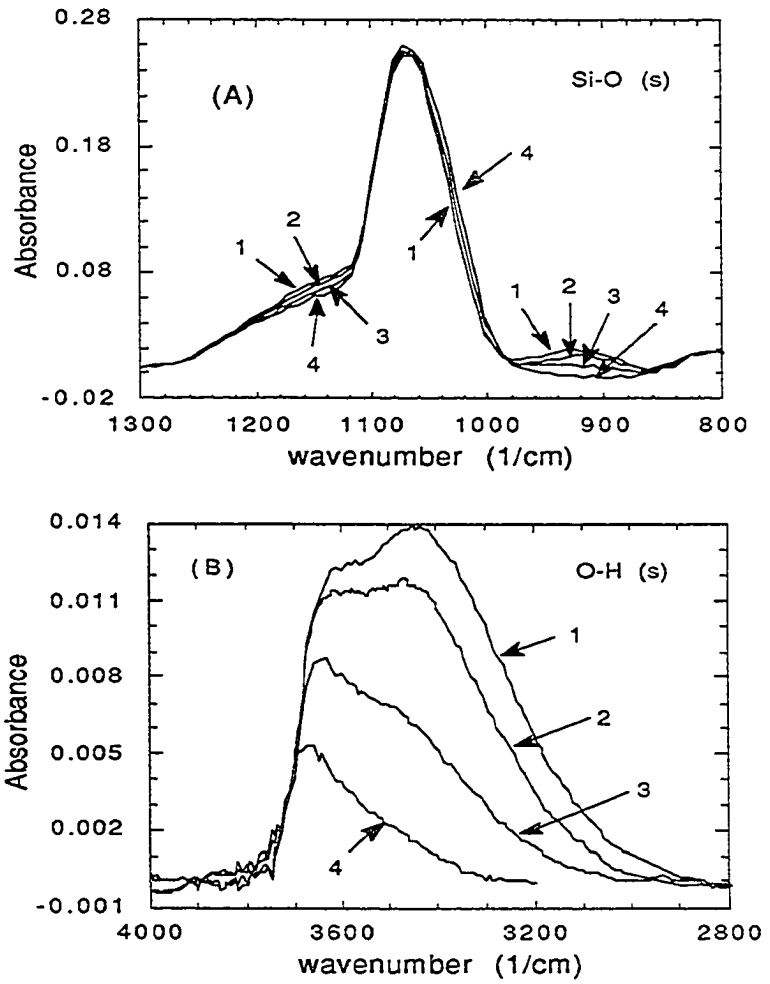

Fig.4-10 Irreversible effects of annealing on absorbance vs wavenumber (A) for the Si-O (s) region (1300-800 cm^{-1}) and (B) for the O-H (s) region (4000-2800) measured at 25 °C for an $a\text{-}SiO_2$ film as-deposited (curve 1) and following anneals at 150 °C (curve 2), 250 °C (curve 3), and 350 °C (curve 4).

Fig.4-10A and B show the irreversible changes in the 3000-3700, 1150, and 925 cm^{-1} regions which are due to the loss of hydrogen from the sample via out-diffusion. Shown here is a clear demonstration of a H-related absorption feature near 1150 cm^{-1}, within the main Si-O-Si band. This absorption may be related to a bending mode of the O-H unit (Tsu and Lucovsky, 1987). Note also that, following the 350 °C anneal, the main Si-O peak has shifted from 1070 to 1067 cm^{-1} and at the same time the FWHM of this peak has increased from 74 to 80 cm^{-1}. The resulting increase in area of this band is consistent with a transfer of absorption from the Si-OH band near 925 cm^{-1} to the main Si-O-Si band as hydrogen leaves the film. The release of hydrogen will occur first from near neighbor OH groups via a reaction such as $2SiOH \leftrightarrow Si\text{-}O\text{-}Si + H_2O$, which is consistent with the above-mentioned shift of absorption.

In order to investigate the hydrogen bond, the sample was first annealed at annealing temperature T_a to stabilize the composition of the film at this temperature and then was cooled down to room temperature. After this annealing process, the film is said to be in an anneal-stable state. Then, infrared measurements were taken at room temperature and at the annealing temperature T_a separately. Interesting reversible temperature dependent changes have been observed. As shown in Fig.4-11, the OH absorption loses intensity at lower wavenumbers, sharpens, and decreases in area when the film temperature increases. These changes in the OH absorption disappear after the film temperature is returned to 25 °C. Since the hydrogen bond strength generally falls in range from 0.04 to 0.5 eV (Pimentel

and McClellan, 1960), it can be broken or weakened when the temperature of film is increased above room temperature. The reversible changes in absorption observed in the O-H (stretching) band in Fig.4-11A at 150 °C, in Fig.4-11B at 250 °C, and in Fig.4-11C at 350 °C are attributed to significant changes in the hydrogen-bonding of OH groups as the temperature of the film is varied. A careful analysis has been carried out for the OH (stretching) absorption band by deconvoluting the OH band to the superposition of three Gaussians centered near 3650, 3520, and 3360 cm^{-1} The 3650 cm^{-1} sub-band corresponds to OH groups which are essentially free, i.e. not hydrogen-bonded, while the 3520 and 3360 cm^{-1} sub-bands are related to hydrogen bonding. From a careful analysis, we can see that a small part of the intensities of the 3360 and 3520 cm^{-1} hydrogen-bonded sub-bands shift to 3650 cm^{-1} as the film temperature increases.

For comparison, the same measurements were taken at liquid N_2 temperature (77 K). As expected, the absorption band gained intensity and became broader, i.e. the area of the OH band was increased when the temperature of film decreased from room temperature. Again, those changes are reversible when the film temperature returns to 25 °C (see Fig.4-12).

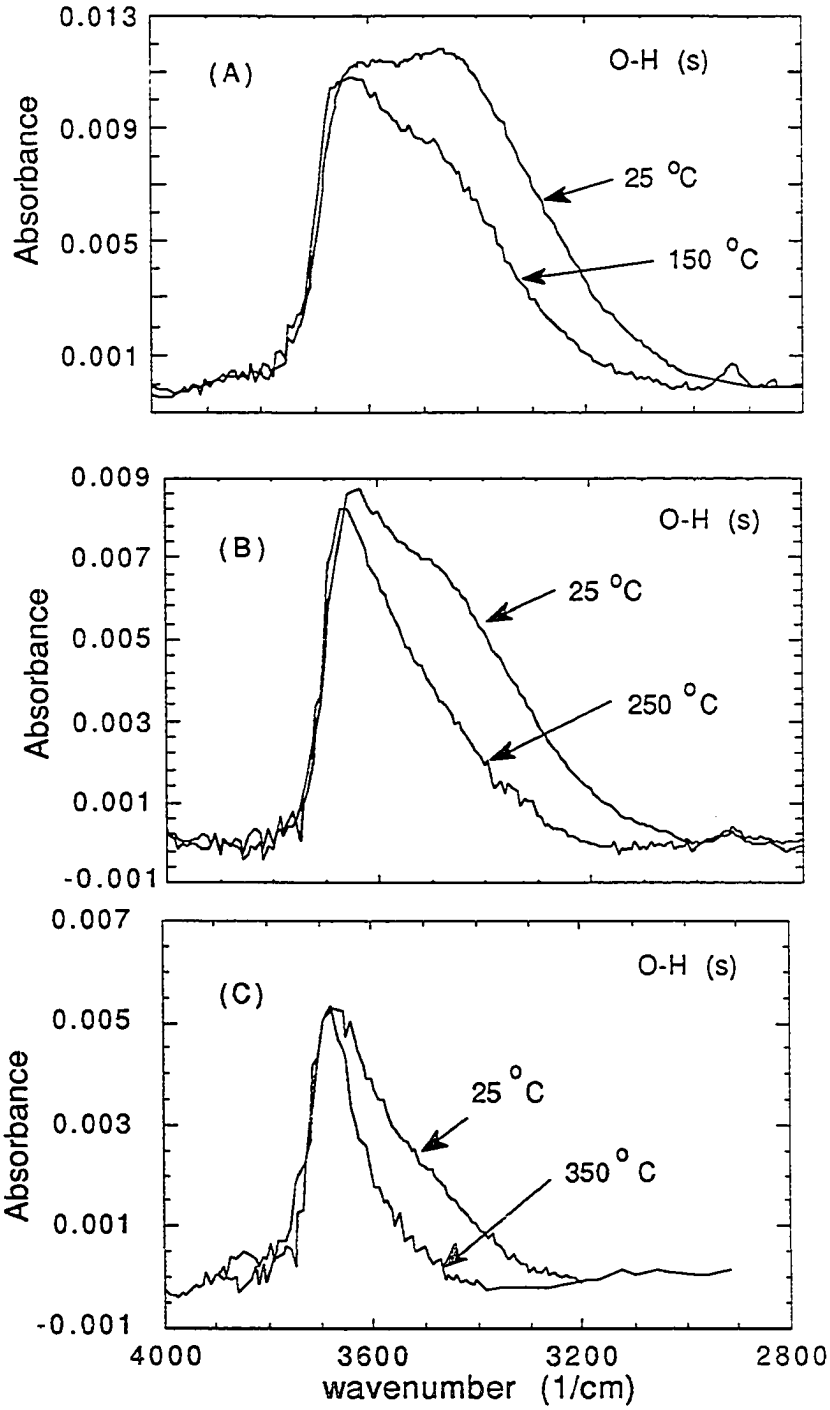

Fig.4-11 Reversible effects of temperature on absorbance vs wavenumber measured at 25 °C (after annealing) and at (A) 150 °C, (B) 250 °C, and (C) 350 °C for the O-H (s) absorption band.

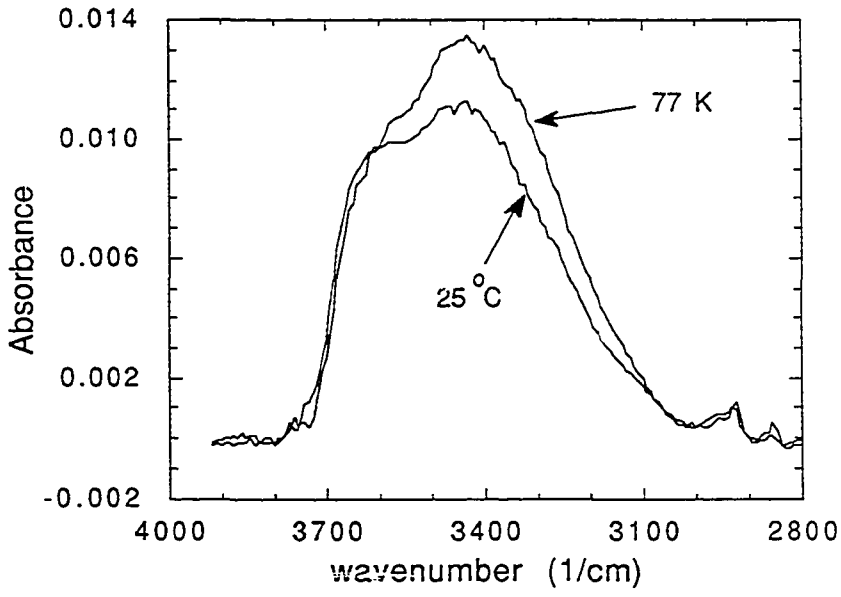

Fig.4-12 Reversible effects of temperature on absorbance vs wavenumber measured at 25 °C and at 77 K for the O-H (s) absorption band.

As we mentioned before, the cross section of hydrogen-bonded sub-band is greater than the cross section of non-hydrogen-bonded band. Therefore, we can conclude that the frequency shift and intensity loss of the OH (stretching) band as temperature increases are due to the breaking or weakening of hydrogen bonding and on the contrary the gain of intensity and broadening of the OH (stretching) band as temperature decreases are caused by the formation or strengthening of hydrogen bonding. These reversible changes are not caused by OH groups leaving or entering in the film with increase or decrease of the film temperature. In other words, the number of O-H groups released from hydrogen-bonding should equal the number of O-H groups transferred to the 3650 cm^{-1} band

when the film temperature is increased. Since the concentration of bonds equals the area of the absorption band divided by the absorption cross section σ, then the relation of the two absorption cross sections for the hydrogen-bonded and the non hydrogen-bonded O-H groups is given as:

$$\frac{1}{\sigma_h} \text{ Area(H-bonded sub-band)} = \frac{1}{\sigma} \text{ Area (non H-bonded sub-band)}$$

$$\text{or} \quad \frac{\sigma_h}{\sigma} = \frac{\text{Area (H-bonded sub-band)}}{\text{Area (non H-bonded sub-band)}} \qquad (4\text{-}6)$$

where σ_h and σ are the absorption cross section for hydrogen-bonded and non hydrogen-bonded O-H groups, respectively. We found that the absorption cross section for the hydrogen-bonded OH groups is enhanced by about a factor of six, in good agreement with previous estimates (Pliskin, 1977; Lucovsky, et al, 1987; Beckmann and Harrick, 1971).

In addition, we can write N(T), the concentration of O-H group associated with hydrogen bonding in an anneal-stable state at temperature T, in terms of a generalized form:

$$N(T) \propto \exp(-E_a/k_bT) \qquad (4\text{-}7)$$

where E_a is a thermal activation energy, k_b is the Boltzmann constant, and T is film temperature. Since the bond concentration is proportional to the normalized area of the absorption band (see eqn.4-5), eqn.4-8 can be written at

$$\text{Area}(T) \propto \exp(-E_a/k_bT) \qquad (4\text{-}8)$$

where Area(T) is the area of the OH absorption bands related to hydrogen bonding, i.e. the two lower bands in the OH absorption region. Then, the ratio of the area at and above room temperature (RT) is as follows:

$$\ln\left(\frac{\text{Area(T)}}{\text{Area(RT)}}\right) = -\left(\frac{E_a}{k_b}\right)\frac{1}{T} + \text{constant} \qquad (4\text{-}9)$$

Therefore, the thermal activation energy can be obtained from the slope of $\ln\left(\frac{\text{Area(T)}}{\text{Area(RT)}}\right)$ vs $\frac{1}{T}$. The value of the thermal activation energy from our experiment is 0.06±0.01 eV which is reasonably consistent with the energy of a hydrogen bond.

The reversible effects of temperature on the main Si-O-Si band are shown in Fig. 4-13A and B. As T increases from 25 to 350 °C (see Fig.4-13A), the peak position, FWHM, and maximum absorption coefficient change from 1067 to 1055 cm^{-1}, from 80 to 87 cm^{-1}, and from 23600 to 22100 cm^{-1}, respectively, while the area of the Si-O-Si band remains essentially constant. When the temperature of film decreases form 25°C to 77 K, all the changes described above occur in the opposite direction, as expected, (see Fig.4-13B). These changes are probably the result of reversible changes in the local environment of the Si-O-Si bonding units, such as increase or decrease of Si-O-Si bond angle disorder with the change of film temperature. More work needs to be done to clarify the origins of these changes.

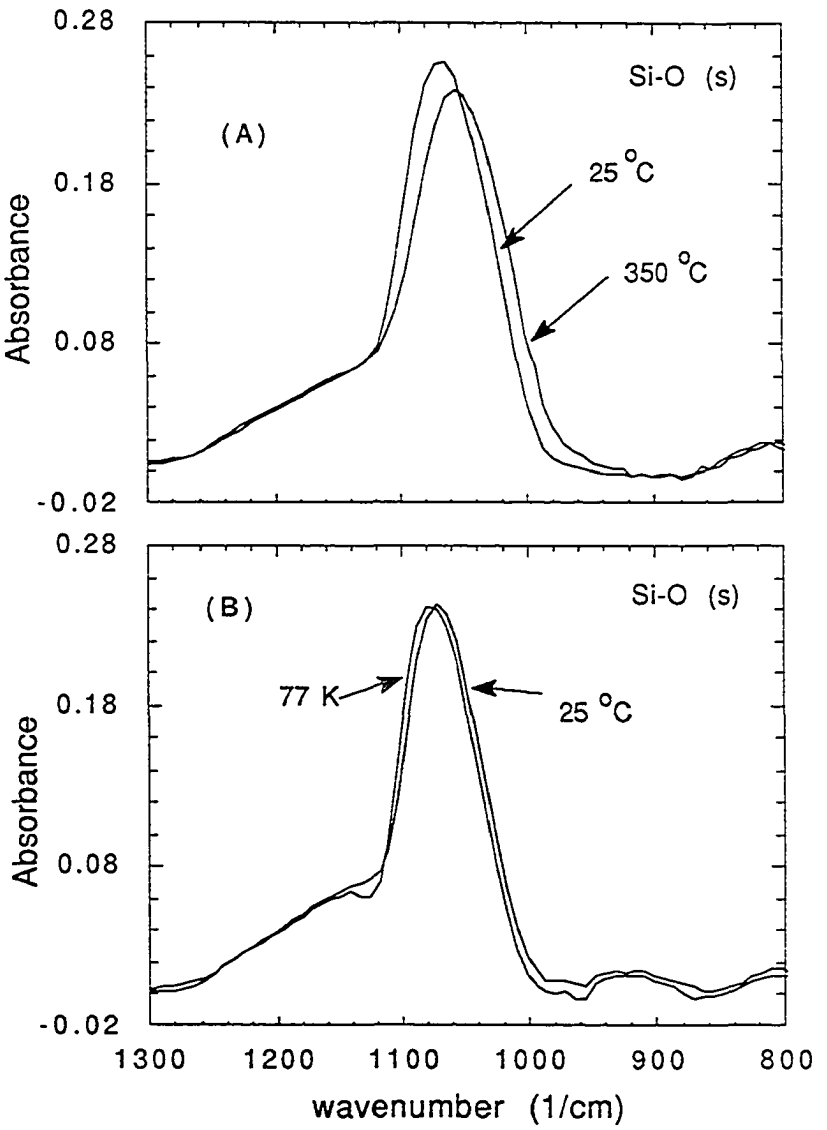

Fig. 4-13 Reversible effects of temperature on absorbance vs wavenumber measured at 25 °C (after annealing) and at (A) 350 °C and (B) 77 K for the Si-O-Si absorption band.

Similar temperature-dependent reversible changes may be expected to be seen in a-$Si_xN_yH_z$ films since N-H groups and N atom with lone pair electrons are present in the alloys. The N-H (stretching) band near 3320 cm^{-1} is observed to be an asymmetric peak with a tail extending on the low wave-number side down to

about 2900 cm^{-1}. This asymmetry was explained (Maeda and Nakamura, 1985) as the effect of hydrogen bonding in the film. Unexpectedly, we have observed no obvious changes in the infrared spectra, to within experimental error, when the film temperature was increased up to 280 °C or decreased to 77 K for the samples prepared at T_S = 400 °C. This result may be explained as follows. The magnitude of the frequency shift due to hydrogen bonding depends on the strength of the hydrogen-bond and in turn is related to the A···B distance. The previous study (Nakamoto et al, 1955) of the relation between the A···B distance and the frequency ν (stretching) shows that the N-H···N stretching band will shift from about 3368 to 3242 cm^{-1} when the N···N distance changes from 3.25 Å to 2.90 Å (ΔR = 0.35 Å), but the O-H···O stretching band will shift from about 3626 to 3116 cm-1 while the same change of ΔR = 0.35 Å (from 3.10 Å to 2.75 Å) occurs. Clearly the N-H stretching absorption band is much less sensitive than the O-H stretching absorption band to hydrogen bonding. This is probably due to the fact that the hydrogen bond for O-H···O, about 0.09-0.5 eV, is stronger than the hydrogen bond for N-H···N, about 0.05-0.16 eV, because the electronegativity of O atoms (3.5) is greater than the electronegativity of N atoms (3.0). Therefore, N···N distance changes in the rigid a-$Si_xN_yH_z$ alloy could be very small so that the infrared measurement is not sensitive enough to detect the change of N-H stretching absorption caused by the hydrogen bonding.

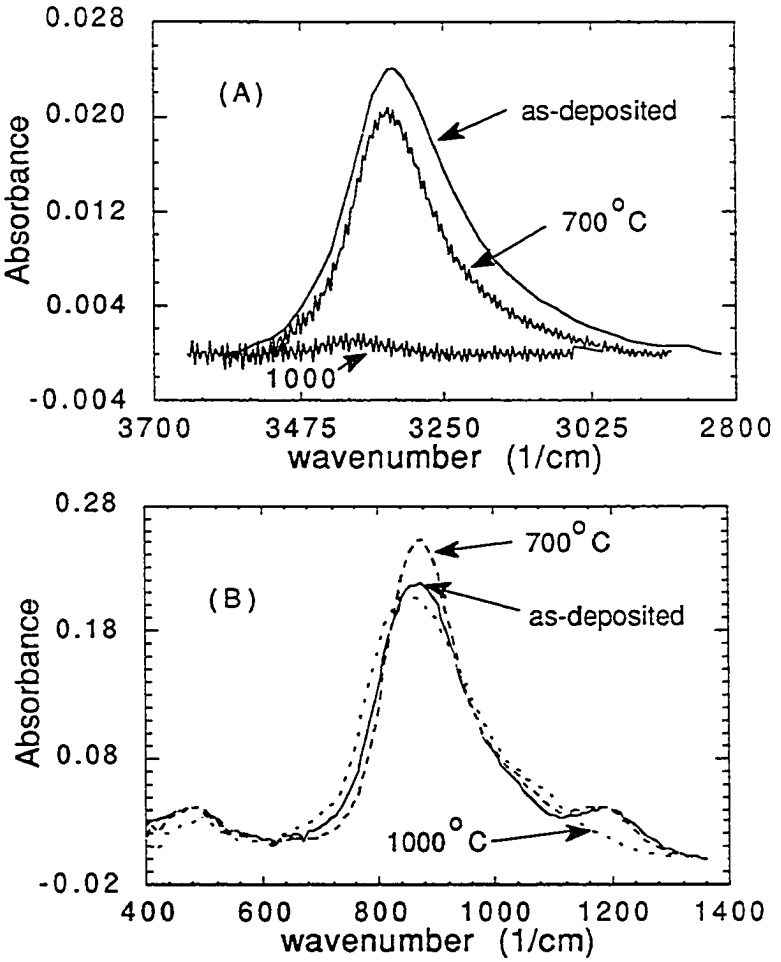

Fig.4-14 Annealing effects on absorbance vs wavenumber measured after deposition, 700 °C annealing, and 1000 °C annealing for (A) N-H (s) band in region 3700-2800 cm^{-1} and (B) region 1400 to 400 cm^{-1} including the Si-N (s) and N-H (b) bands.

To gain additional insight into the behavior of hydrogen, we carried out an annealing study of an a-$Si_xN_yH_z$ alloy film. The film (R=40, P=0.15 Torr, T_S = 400, and power = 0.43 W/cm^2) was annealed at 700 and at 1000 °C for an hour in an argon atmosphere. The changes for the hydrogen-related bands, N-H stretching which is centered at 3350 cm^{-1} and N-H bending band which is centered at

1175 cm^{-1}, clearly show in Fig.4-14A and B that hydrogen atoms were driven from the sample after annealing. Also, it has been observed that the absorption band at 1550 cm^{-1} (H-N-H bending mode) increased after the 700 °C annealing. This provides evidence for the conversion of N-H bonding units to $N-(H)_2$ units. The areas of the Si-N (stretching), N-H (stretching and bending), and $N-(H)_2$ (bending) bands before and after annealing for this sample are listed in Table 4-2. During the annealing process, the N-H units will first convert to $N-(H)_2$ units, then the near neighbor NH_2 groups will react with each other to release NH_3 via a reaction such as $2N-SiH_2 \leftrightarrow N-HSi_2 + NH_3\uparrow$. The Si-N bond concentration should therefore not be changed by the release of NH_3 from the film. However, we can see in Table 4-2 that the area of the Si-N band increases after annealing. This could be caused by the increase of the cross section due to the change of the film composition after annealing. The relation of cross section and composition is not clear so far. More work needs to be done to clarify the change of the infrared spectra of the sample after annealing treatment.

Table 4-2 Annealing result for $\int \alpha \, dv$ for sample 4

	Si-N(s) (10^5 cm^{-2})	N-H(s) (10^5 cm^{-2})	N-H(b) (10^5 cm^{-2})	NH_2(b) (10^4 cm^{-2})
Befor annealing	42.92	5.18	6.18	0.88
700 °C annealing	43.82	3.49	5.89	1.36
1000 °C annealing	49.07	0.11	1.74	not observed

Chapter 5 Density and Composition of a-$Si_xN_yH_z$ Films

5.1 Density and Deposition Rate of the Films.

The density of a film is equal to the mass of the film divided by the volume of the film. It is straightforward to get the mass of the film by weighing the substrate before and after deposition. In order to get accurate results for the mass of a film, aluminum foil was chosen as the substrate since the lighter the substrate is, the better the accuracy is for the mass of the film. The thickness of the film on the aluminum substrate is determined from the interference fringes observed from the reflection measurement for the film. As we know, constructive interference for two beams occurs whenever their path difference is an integral multiple of the wavelength. When a beam is incident on a thin film with thickness d and refractive index n, the path difference for the two interfering beams from the upper and lower surfaces of the film is equal to 2nd for normal incidence. Therefore, the condition for constructive interference for a thin film is:

$$2nd = m\ \lambda_m \qquad (5\text{-}1)$$

where m (= 0, 1, 2, ...) is the order of the interference. λ_m is the wavelength corresponding to mth order maximum intensity.

In addition to the path difference, the phase shift of reflectance at the surfaces for the two beams has to be considered also, i.e. the order m should be replaced by (m + 1/2) when a half cycle phase

shift occurs. In order to understand the shift of phase for a beam reflected from a surface, let's consider a surface which separates the medium n_o from medium $n_1 = n_1 - ik_1$. The Fresnel reflection coefficients (Heavens, 1955) for normal incidence on the surface can be written as:

$$r = \sigma e^{i\beta} = \frac{n_o - n_1 + ik_1}{n_o + n_1 - ik_1} \qquad (5\text{-}2)$$

or

$$\sigma(\cos\beta + i \sin\beta) = \frac{n_o - n_1 + ik_1}{n_o + n_1 - ik_1} \qquad (5\text{-}3)$$

where σ represents the (real) amplitude of the reflected beam for unit incident amplitude and β is the phase change of the reflected beam at the surface.

For a non-absorbing medium, i.e. $k_1=0$, eqn.5-3 can be simplified to

$$\sigma(\cos\beta + i \sin\beta) = \frac{n_o - n_1}{n_o + n_1} \qquad (5\text{-}4)$$

so:

$$\sin\beta = 0, \quad \text{and} \quad \sigma\cos\beta = \frac{n_o - n_1}{n_o + n_1} \qquad (5\text{-}5)$$

or

$$\beta = \begin{cases} 2m\pi & \text{for } n_o > n_1 \quad \text{no phase shift} \\ (2m+1)\pi & \text{for } n_o < n_1 \quad \text{half cycle phase shift} \end{cases} \qquad (5\text{-}6)$$

where m is a integer.

For a higher absorption medium, i.e. $k_1 >> n_0$ & n_1, eqn.5-3 can be simplified to:

$$\sigma (\cos\beta + i \sin\beta) = -1 \qquad (5\text{-}7)$$

so:

$$\sin\beta = 0, \quad \text{and} \quad \cos\beta = -1$$

or:

$$\beta = (2m+1)\pi \qquad \text{half cycle phase shift} \qquad (5\text{-}8)$$

For our sample system, there is a half cycle phase shift at the interfaces of air/film, film/Si, and film/Al since n(air) = 1, n(film) ~ 1.7-2.0, n(Si) ~ 3.4, and higher absorption in the aluminum substrate. The net phase shifts of the two beams from the upper and lower surfaces of the film on Si and Al substrates are therefore zero. Hence, the thickness of the film deposited on the aluminum or silicon substrate is:

$$d = m \frac{\lambda_m}{2n} \qquad (5\text{-}9)$$

Fig 5-1 is an example of the measured reflectance for a sample deposited on an aluminum substrate which is prepared at R=60, P=0.5 Torr, power density=0.43 W/cm^2, and T=200 ^{o}C. Since eqn. 5-9 is valid only for a non-absorbing film, only the data above λ = 4500 Å, in which region the absorption of film is close to zero, are used.

The three different substrates (quartz, aluminum, and silicon) are mounted together into the deposition chamber for deposition of

the films in the same run. It is reasonable to assume that the refractive indices of the films (which are a few thousand Å thick or more) are the same for films deposited on the different substrates in the same process since the substrate effect is only important at the beginning of the deposition. Therefore, the values of the refractive index obtained from the film on the quartz substrate (discussed in chapter 3) were used in eqn. 5-9. The order of m in eqn. 5-9 is initially guessed. Only when the correct m is given, will a constant d be obtained for all the maxima of reflectance in range of wavelength from 4500 to 8250 Å.

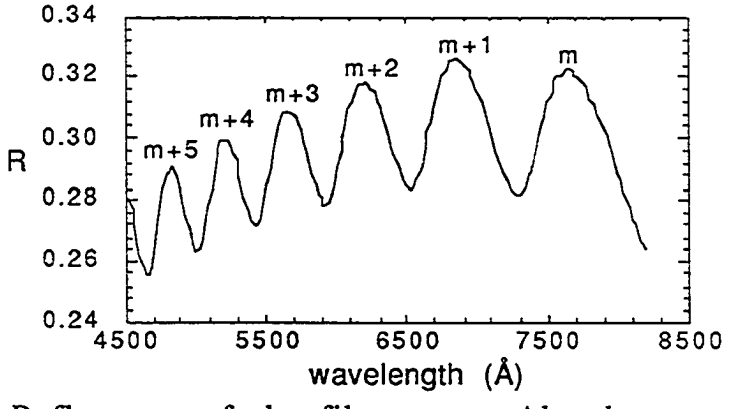

Fig.5-1 Reflectance of the film on an Al substrate prepared at R=60, T_S=200°C, P=0.5 Torr, power=0.43 W/cm^2.

Once the value of d has been determined, values for density ρ and growth rate are determined from ρ = m/Ad and growth rate = d/t, where m is the mass of the film, A the area of the film, t the time of deposition. The results of density and the growth rate for our samples are listed in Table 5-1 and their changes as functions of the deposition parameters (substrate temperature T_S, gas ratio R, and deposition power density) are shown in Fig.5-2. A summary of these results will be given later in this chapter.

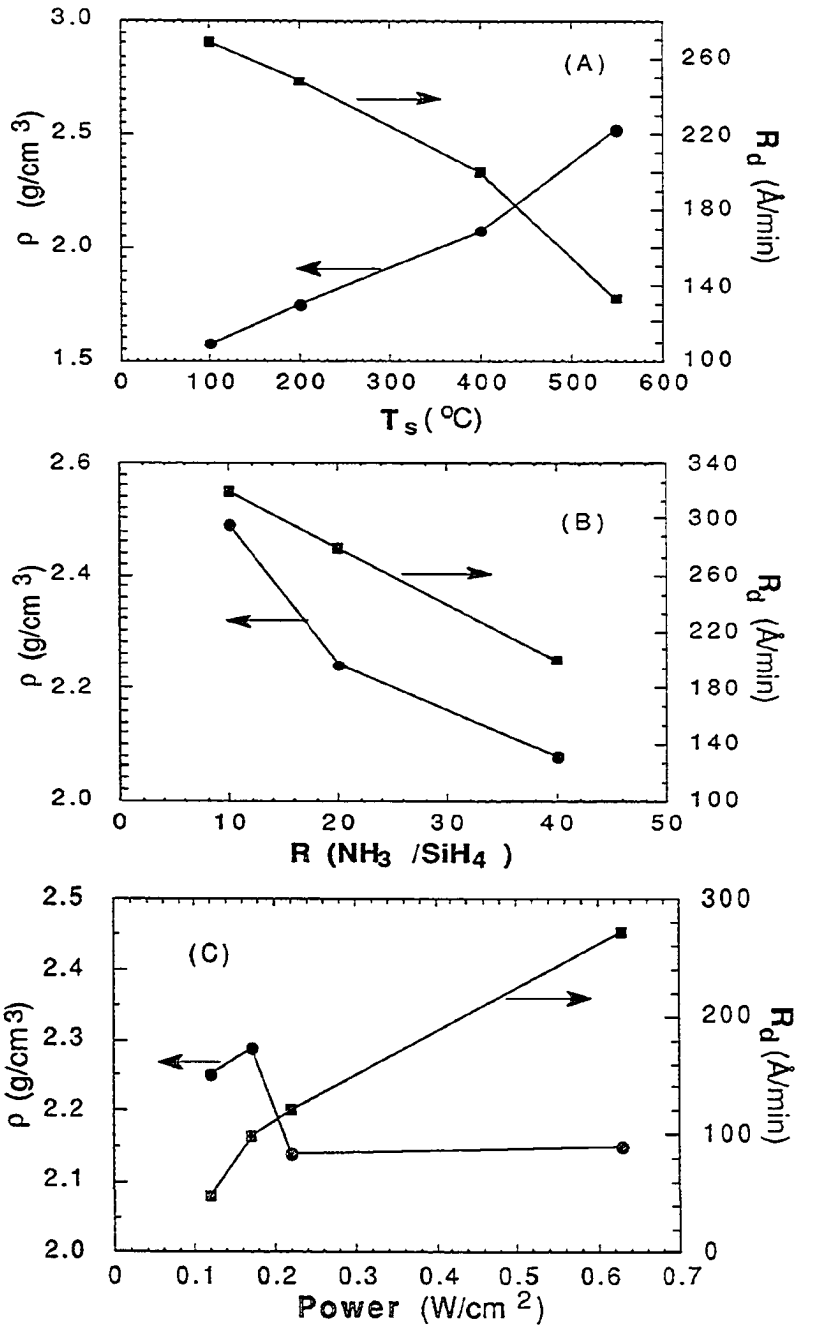

Fig.5-2 Film densities ρ and deposition rates R_d as functions of (A) substrate temperature T_s (samples 9, 10, 3, and 11); (B) reactant ratio R (=NH_3/SiH_4) (samples 1, 2, and 3); and (C) power density (samples 5, 6, 7, and 8).

Table 5-1 Thicknesses d (on quartz substrates), densities ρ, and deposition rates R_d for a-$Si_xN_yH_z$ films studied.

sample	thickness d (Å)	density * ρ (g/cm^3)	deposition rate R_d (Å/min)
1	9800	2.49	320
2	8600	2.24	280
3	14000	2.08	200
4	2552	2.18	60
5	5700	2.25	47
6	10219	2.29	99
7	7997	2.14	120
8	16120	2.15	272
9	16150	1.58	285
10	17350	1.75	254
11	7960	2.52	133

*. The uncertainty of densities is less than ±0.1 g/cm^3.

5.2 Film Composition

Si, N, and H are the three elements present in the plasma enhanced CVD silicon nitride films. Therefore, there are six possible types of bonds present inside the films, i.e. Si-N, Si-H, Si-Si, N-H, N-N, and H-H bonds. Since H-H bonds are not part of the network, it is reasonable to exclude them from the analysis. Also, N-N bonds are not considered since Si-N (3.45 eV) and N-H (4.05 eV) bonds are

much more stable than the weaker N-N (1.7 eV) bond*.

Based on the above assumptions, the relations between bond concentrations (i. e. N(Si-N), N(Si-H), N(Si-Si), and N(N-H)) and atom concentrations (i. e. N(Si), N(N), and N(H)) of the film are as follows:

$$N(Si) = \frac{1}{4}[\,N(Si\text{-}N) + N(Si\text{-}H)] + \frac{1}{2}N(Si\text{-}Si) \qquad (5\text{-}10)$$

---

* The single bond energies for the Si-N, N-H, and N-N bonds are obtained by using the heats of formation ΔH^o (300 °K) of H, N, Si, Si_3N_4, NH_3, and N_2H_4 as given in the JANAF Thermochemical Tables (Stull and Prophet, 1971). For example, in order to get the Si-N bond energy, we need to find out the heat of formation of Si_3N_4 for the following reaction:

$$3\,Si\,(g) + 4\,N\,(g) \rightarrow Si_3N_4\,(s) \qquad (1)$$

where the letters (g) and (s) in parenthesis indicate the gas phase and solid phase, respectively. Although the heat of formation for this reaction cannot be found in the JANAF Thermochemical Tables, we can find the heats of formation for the following reactions:

(a) $3\,Si\,(s) + 2\,N_2\,(g) \rightarrow Si_3N_4\,(s)$ $\quad \Delta H^o = -178.009$ kcal/mole

(b) $N\,(g) \rightarrow \frac{1}{2}N_2\,(g)$ $\quad \Delta H^o = -112.978$ kcal/mole

(c) $Si\,(g) \rightarrow Si\,(s)$ $\quad \Delta H^o = -107.701$ kcal/mole

Now, adding the three equations together to obtain the desired one :

$3\,Si\,(s) + 2\,N_2\,(g) \rightarrow Si_3N_4\,(s)$	$\Delta H^o = -178.009$ kcal/mole
$4\,N\,(g) \rightarrow 2\,N_2\,(g)$	$\Delta H^o = -4 \times 112.978$ kcal/mole
$3\,Si\,(g) \rightarrow 3\,Si\,(s)$	$\Delta H^o = -3 \times 107.701$ kcal/mole
$3\,Si\,(g) + 4\,N\,(g) \rightarrow Si_3N_4\,(s)$	$\Delta H^o = -953.024$ kcal/mole

Therefore, we find that the heat given off in the process (1) is 953.024 kcal per mole of Si_3N_4. Since there are twelve Si-N bonds in each Si_3N_4 formula unit, the average Si-N bond energy is equal to 953.024 ÷ 12 = 79.42 kcal/mole = 3.45 eV/bond. Similar analyses have been carried out to determine the N-H and N-N bond energies.

$$N(N) = \frac{1}{3}\,[\,N(Si\text{-}N) + N(N\text{-}H)\,] \qquad (5\text{-}11)$$

$$N(H) = N(N\text{-}H) + N(Si\text{-}H) \qquad (5\text{-}12)$$

where the bonding valences of Si, N, and H in the films are taken to be 4, 3, and 1, respectively.

In addition, the density of the film is given by:

$$\rho = m_{Si}\,N(Si) + m_N\,N(N) + m_H\,N(H) \qquad (5\text{-}13)$$

where the m_i are atomic masses.

From infrared measurements, we can obtain the N-H and Si-H bond concentrations by using eqn.(4-5). Since there is no accepted value of K(Si-N), which was discussed in Chapter 4, we cannot determine the Si-N bond concentration N(Si-N) properly from the infrared measurement. Therefore, the more reliable value of the Si-Si bond concentration obtained by using the Si-centered tetrahedron model with the Bruggemann effective medium approximation (EMA), which will be discussed in detail in chapter 6, was used with the experimental values for N(N-H), N(Si-H), and density ρ in equations (5-10) to (5-13) in order to solve for the four unknowns: N(Si), N(N), N(H), and N(Si-N). The value of the Si-Si bond concentration is considered to be more reliable because the optical absorption edge is directly related to the presence of the weaker Si-Si bonds (see details in chapter 6).

Table 5-2 Bond concentrations and K(Si-N)[a] values for a-$Si_xN_yH_z$ films studied

sample	N(N-H) (10^{22} cm^{-3})	N(Si-H) (10^{22} cm^{-3})	N(Si-Si) (10^{22} cm^{-3})	N(Si-N) (10^{22} cm^{-3})	K(Si-N) (cm-1)
1	1.12	0.65	0.36	11.35	2.46
2	3.19	0.29	0.15	9.56	2.02
3	3.66	not observed less than 0.002	0.084	8.79	1.80
4	4.24	not observed less than 0.002	0.092	9.02	2.10
5	3.46	0.17	0.13	9.59	2.45
6	2.61	0.16	0.09	10.26	2.35
7	3.19	0.18	0.12	9.16	2.09
8	4.45	0.10	0.056	8.73	1.76
9	6.07	0.19	0.052	5.58	2.14
10	5.06	0.17	0.068	6.32	1.88
11	1.96	0.14	0.065	11.8	2.25

*Bond concentrations N(X-Y); typical uncertainties are ±8% for N(N-H) and N(Si-H), ±25% for N(Si-Si), and ±5% for N(Si-N).

a. $K(Si\text{-}N) = \frac{1}{N(Si\text{-}N)} \int \alpha dv.$

The results for the bond concentrations N(N-H), N(Si-H), N(Si-Si), and N(Si-N) are listed in Table 5-2. Also given in Table 5-2 are values for K(Si-N) determined from the values of N(Si-N) given in Table 5-2 and the measured normalized infrared absorption band

Table 5-3 Atom concentrations, compositions, and [N]/[Si] ratios for a-$Si_xN_yH_z$ films studied

Sample	N(Si)[a] ($10^{22}cm^{-3}$)	N(N)[a] ($10^{22}cm^{-3}$)	N(H)[a] ($10^{22}cm^{-3}$)	x [b]	y [b]	z [b]	y/x
1	3.18	4.16	1.77	0.349	0.457	0.194	1.31
2	2.54	4.25	3.48	0.247	0.414	0.339	1.68
3	2.24	4.15	3.66	0.223	0.413	0.364	1.85
4	2.30	4.42	4.24	0.210	0.403	0.387	1.92
5	2.51	4.35	3.36	0.239	0.415	0.346	1.74
6	2.65	4.29	2.77	0.273	0.442	0.285	1.62
7	2.40	4.12	3.37	0.243	0.416	0.341	1.71
8	2.24	4.36	4.55	0.200	0.393	0.407	1.97
9	1.47	3.88	6.26	0.127	0.334	0.539	2.63
10	1.66	3.79	5.23	0.155	0.355	0.490	2.29
11	3.02	4.59	2.10	0.311	0.473	0.216	1.52

* Note that x, y, and z are meaningful to only two significant figures. In order to match the N(N)/N(Si) and y/x, three significant figures are kept for x, y, and z.

a. Atom concentrations N(X); typical uncertainties are ±6% for N(Si), ±5% for N(N), and ±7% for N(H).

b. Film composition; typical uncertainties are ±6% for x, ±6% for y, and ±8% for z.

areas $\int \alpha dv$ for Si-N (stretching) presented in Table 4-1. These values of K(Si-N) for nearly stoichiometric films are in good agreement with the results of Bustarret et al (see chapter 4). The atom concentrations N(Si), N(N), N(H), and composition parameters x, y, z, as well as the [N]/[Si] ratios y/x, for these a-$Si_xN_yH_z$ alloys are listed in Table 5-3.

Table 5-4 Comparison of SAM and composition results from our IR + ε + ρ measurements.

	$\frac{([N]/[Si])_1}{([N]/[Si])_2}$	$\frac{([N]/[Si])_1}{([N]/[Si])_3}$	$\frac{([N]/[Si])_1}{([N]/[Si])_4}$
SAM	0.81	0.72	0.64
our method	0.78	0.71	0.68

In order to check the results for the compositions of our films by using the above optical data analysis, i.e., infrared results for N(N-H) and N(Si-H), and N(Si-Si) from EMA analysis, comparisons of those results and SAM (scanning Auger microprobe) results were carried out. Because there are no valid SAM sensitivity factors for N and Si atoms in a-$Si_xN_yH_z$ alloys, the absolute value of atomic ratio [N]/[Si] for each sample cannot be determined. However, if we assume the sensitivity factors for N and Si atoms are constant in all the a-$Si_xN_yH_z$ alloys, then changes in the [N]/[Si] ratio between different samples should still be meaningful. SAM measurements have been taken for samples 1 to 4. In Table 5-4, the values of the [N]/[Si] ratio for sample 1 divided by the [N]/[Si] ratios for sample 2, 3, and 4, i.e.,$([N]/[Si])_1/([N]/[Si])_i$ where i=2, 3, and 4, are given from SAM measurements and from our optical analysis. One can see that the values from the two different methods agree to within 6% difference. In other words, the method we used to obtain the composition for a-$Si_xN_yH_z$ films is reliable.

For the computation of the experimental uncertainties in the bond concentrations, the accuracies of the cross sections have been

assumed to be ±5% for K(N-H) and K(Si-H). It should be pointed out that the reproducibility of the bond concentrations measured for films of different thicknesses prepared under the same conditions is much better than the estimated absolute accuracies quoted in Table 5-2. Again, the reproducibility of the results obtained for the atom concentrations and in turn x, y, and z is much better than the estimated absolute uncertainties given in Table 5-3.

5.3 Summary of Experimental Results.

A summary of the experimental results is given below.

Substrate temperature (T_S) effect. — As the substrate temperature is increased from 100 to 550 °C, the fraction of H atoms z decreases monotonically and the fractions of Si and N atoms x, y in the film increase monotonically, which is consistent with the observed increase of the film density (see Fig. 5-2A). At the same time, the ratio y/x decreases (see Fig.5-3). Also, the refractive index n (at 1.5 eV) increases with the increase of T_S (see Fig.3-9), which is also consistent with the increase of film density.

These experimental results can be explained very well by D. L. Smith's condensation mechanism (Smith et al, J. Electrochem. Soc.1990). They found that the triaminosilane radical, $Si(NH_2)_3$, in NH_3-SiH_4 plasmas is the principal depositing specie. A $Si(NH_2)_3$ radical absorbs on an N site, most likely one from which H has desorbed. Amino (NH_2) groups from neighboring $Si(NH_2)_3$ units on the surface react with each other to evolve NH_3 molecules, leaving Si and N dangling bonds which combine to develop the Si-N network

(see Fig.5-4). When the substrate temperature increases, more NH_3 will be driven off, i.e. more Si-N bonds will be formed per unit volume which can be seen very clearly in Fig.5-5. N(N-H) decreases with the increase of N(Si-N) when T_S increases from 100 to 550 °C. This explanation is also consistent with our experiment observations for the deposition rate and density of the films. As shown in Fig.5-2A, the deposition rate decreases and the film density increases with the increase of the substrate temperature. These results are in good agreement with the results of other researchers (Dun, et al, 1981, Maeda and Arita, 1982).

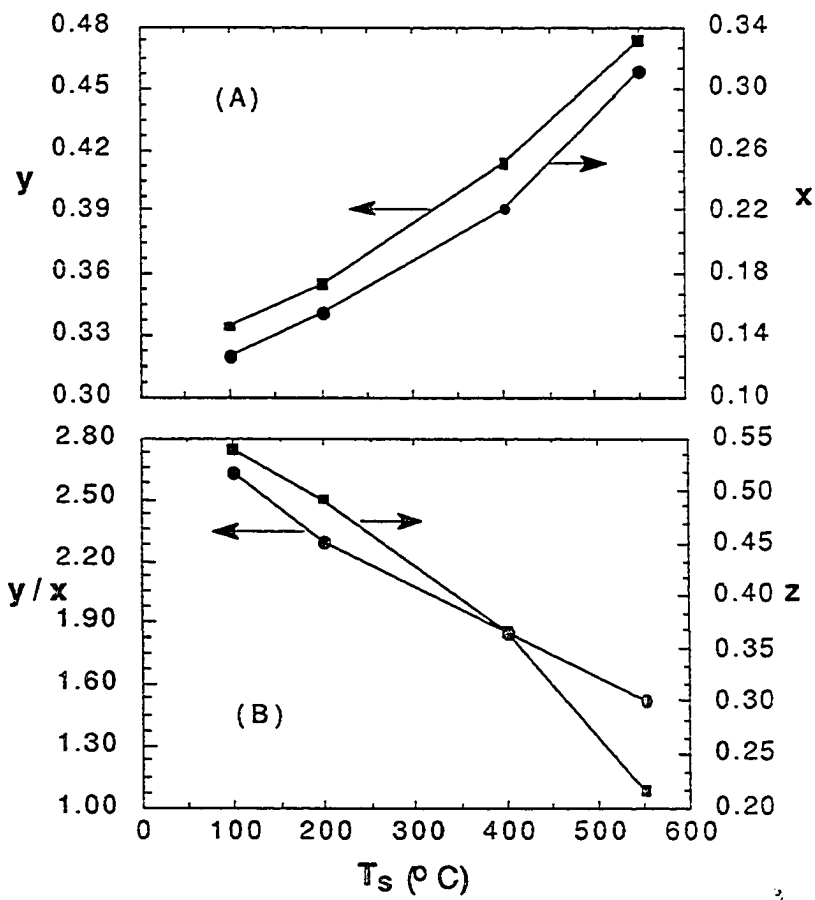

Fig.5-3 Film composition parameters, (A) x and y, and (B) z as well as the [N]/[Si] ratio y/x, as functions of substrate temperature T_S (samples 9, 10, 3, and 11).

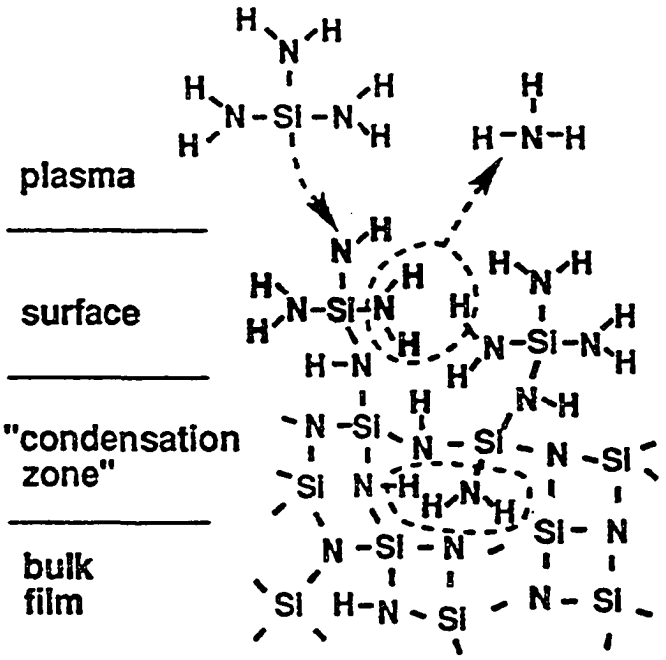

Fig.5-4 Condensation model for adsorbing $Si(NH_2)_3$ leading toward the development of the Si-N network with the evolution of NH_3 . (From D.L. Smith et al, 1990A)

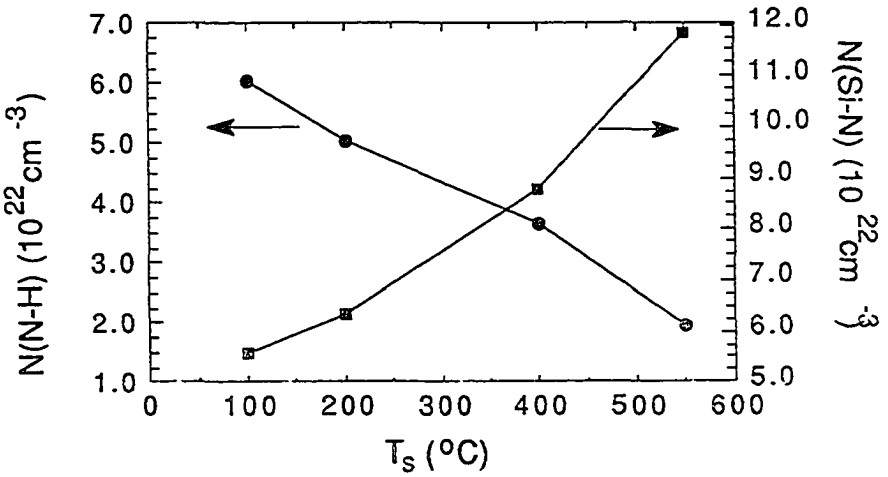

Fig.5-5 N-H and Si-N bond concentrations for the films as functions of substrate temperature T_S.

Reactive gas ratio (R) effect. — As the gas ratio R = NH_3/SiH_4 is increased from 10 to 40, the hydrogen fraction z and the ratio of N and Si atoms y/x both increase. But the Si and N fractions x and y both decrease with the increase of R (see Fig.5-6), which is consistent with the observation of decreasing density of the films (Fig.5-2B) and decreasing refractive index n (at 1.5 eV) for the films (see Fig.3-10). The key factor for this set of experiments is the flow rate of SiH_4. Ammonia requires more energy to be activated than does silane (the bond energies for $H\text{-}NH_2$ and $H\text{-}SiH_3$ are 110 and 94 kcal/mole (Weast, 1971), respectively.), i.e. SiH_4 dissociates much more readily than does NH_3. When the SiH_4 flow rate decreases and the NH_3 flow rate stays constant at a much higher rate, at least 10 times higher than SiH_4, the utilization of silane will increase to close to unity. In other words, the flow of SiH_4 into the plasma limits the deposition rate in this case. As shown in Fig. 5-7, the deposition rate decreases from about 380 Å/min to about 200 Å/min when the SiH_4 flow rate decreases from 10 sccm to 2.5 sccm with NH_3 flow rate constant at 100 sccm. In this set of experiments, the NH_3 flow rate is maintained at 100 sccm with variable flow rates for SiH_4 in order to obtain the desired gas ratio R = 10, 20, and 40. Therefore, when R increases in our experiment, it really means that the SiH_4 flow rate decreases. Also, one can see from Fig.5-7 that the Si-H bond concentrations are controled by the SiH_4 flow rate, i.e., N(Si-H) increase with the increase of SiH_4 flow rate during deposition of the films. When SiH_4 flow rate is less than 2.5 sccm, Si-H bonds are not observed in IR measurement.

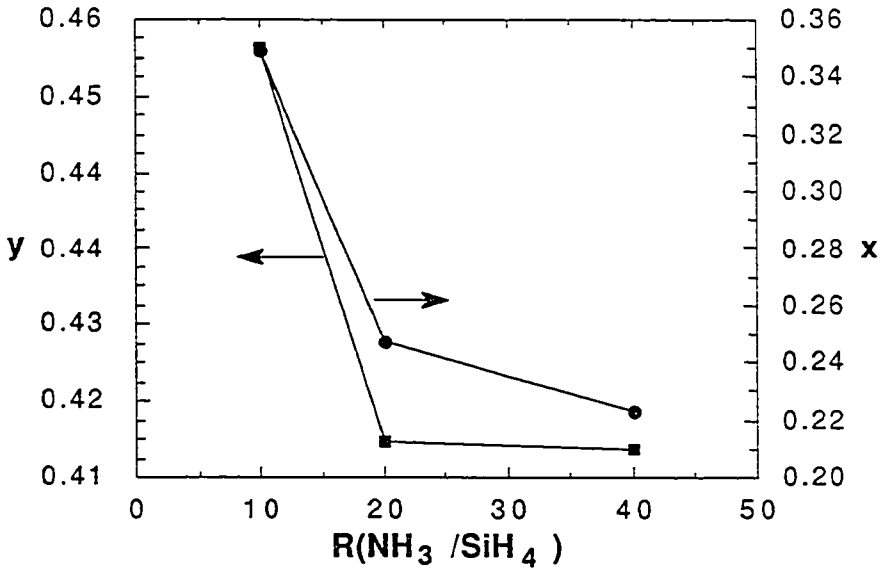

Fig.5-6A Film composition parameters x and y vs reactant ratio $R=NH_3/SiH_4$.

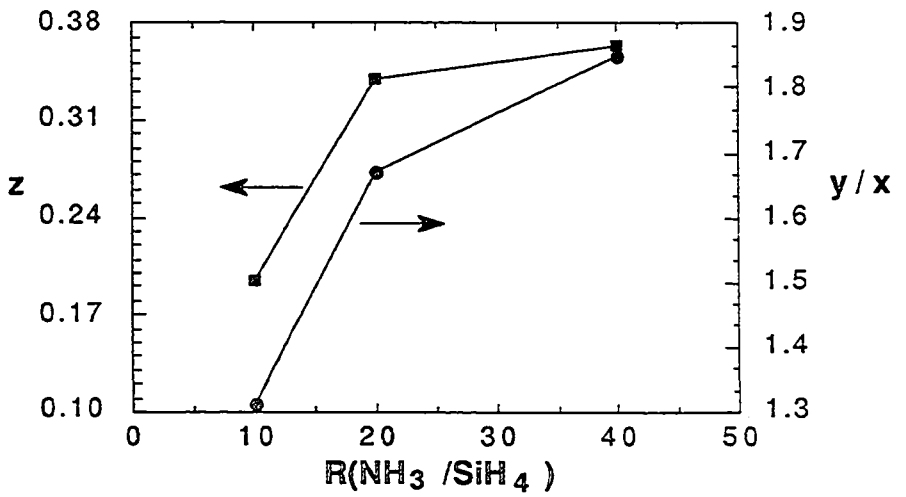

Fig.5-6B Hydrogen content and the [N]/[Si] ratio for the films (samples 1, 2, and 3) vs reactant ratio $R=NH_3/SiH_4$.

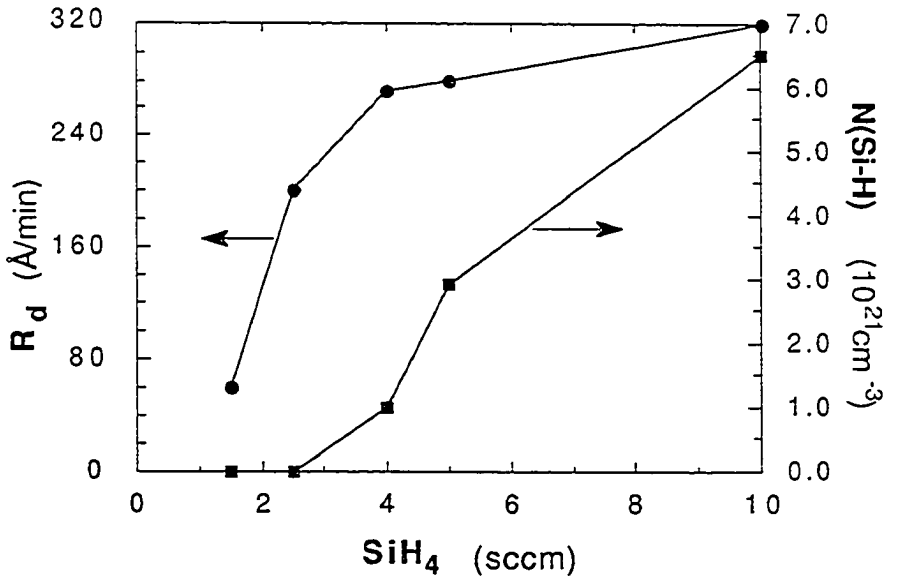

Fig.5-7 Deposition rate R_d and Si-H bond concentration N(Si-H) as functions of SiH_4 flow rate at T_s=400°C (samples 1, 2, 8, 3, and 4).

RF power effect. — As the RF power is increased, the deposition rate is increased as expected (see Fig.5-2C), which agrees with Dun's results. At lower power density (less than 0.17 W/cm^2), the density of the film increases slightly as the power increases (see Fig.5-2C). The film composition parameters x and y initially increase and z and y/x initially decrease with the increase of power density (see Fig.5-8A and B) in this region. The main trends for power density greater than 0.17 W/cm^2 are: (1) x and y decrease with increase of deposition power as shown in Fig.5-8A; (2) z and y/x increase with increase of deposition power (Fig.5-8B); (3) the density of the film first decreases for power from 0.17 to 0.22 W/cm^2 and then is constant as the power density increases to 0.63 W/cm^2 (see Fig.5-2C). Also, we note that the sample prepared at the highest power density,

$0.63 W/cm^2$, is close in composition to $Si(NH)_2$ with x = 0.2 and y = z = 0.4. From Fig.5-2C, one can see that the change of density occurs on a small scale.

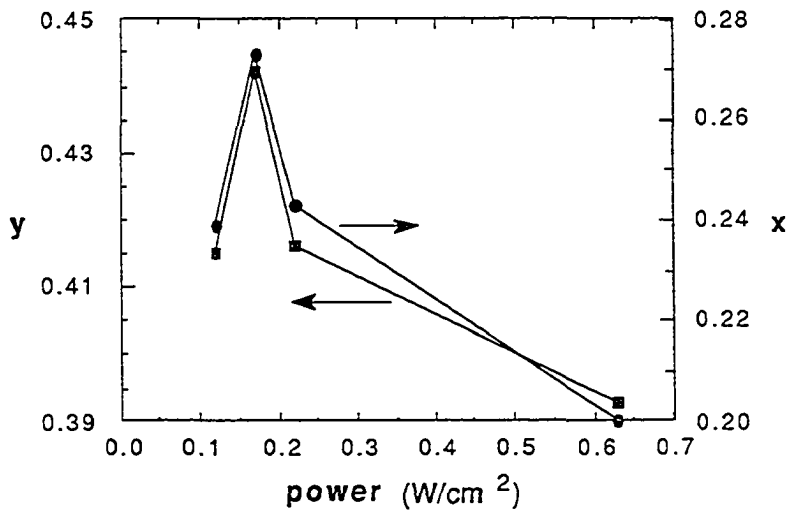

Fig.5-8A Film composition parameters x and y as functions of power densities at T_S=400°C, P=0.5 Torr, and R=60.

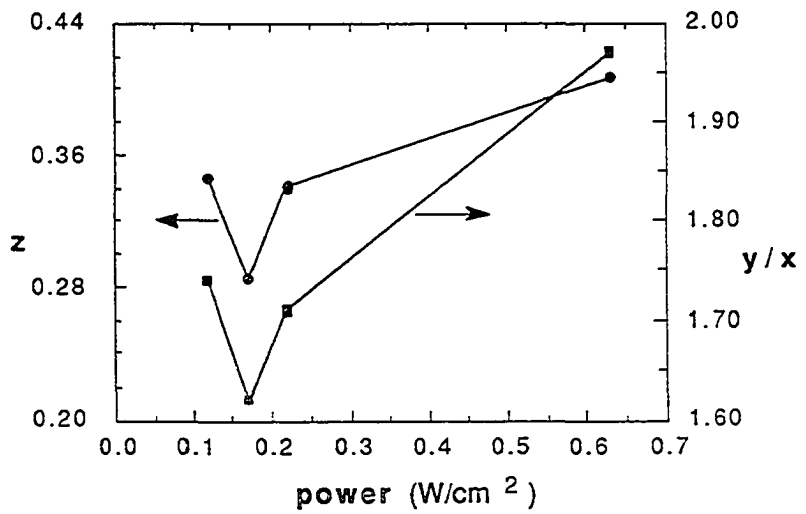

Fig.5-8B Hydrogen content z and the [N]/[Si] ratio y/x as functions of power density at T_S=400°C, P=0.5 Torr, and R=60.

We did not observe strong effects of the power density on the dielectric function ε (see section 3.5 of chapter 3). As discussed in section 3.5 of chapter 3, the plasma for our experiment may already be in the power saturation regime according to D.L. Smith' studies (D. L. Smith et al, J. Electrochem. Soc. 1990). Nevertheless, the change of power density in the power saturation regime has an effect on both the film composition and in turn the density of the films. At lower power density (less than 0.17 W/cm^2), minority species such as disilane present in the plasma may take part in the reaction on the surface, i.e., the concentration of H will be higher at lower power. When the power is high enough (greater than 0.17 W/cm^2), the effect of disilane on the film composition is not important and the growth of film is controlled by the triaminosilane, $Si(NH_2)_3$. More careful experiments need to be done to really understand the growth mechanism in detail.

For a-$Si_xN_yH_z$ films, Si-Si and Si-H bonds have been proposed (Jousse and Kanicki, 1989; D. L. Smith et al, J. Electronic Mater, 1990) to act as precursors for the Si dangling bonds which are important defects in the a-$Si_xN_yH_z$ films currently used in a variety of device-related applications. Also, we note that the films with higher N-$(H)_2$ concentrations are not thermally stable, such as the film prepared at 100 °C. Obvious evidence for oxygen can be seen in Fig.4-9. Therefore, in order to get good quality, stable films for device-related applications, Si-H, Si-Si, and N-$(H)_2$ bonds should be minimized. In Fig. 5-9 the density of Si-Si bonds N(Si-Si) and the infrared absorption area for the N-$(H)_2$ band (Table 4-1) are plotted

vs the [N]/[Si] ratio y/x. We can see that the minimum of the sum of Si-Si and N-$(H)_2$ bond concentrations corresponds to y/x of about 1.85-1.95, which is close to the ratio y/x = 2 for $Si(NH)_2$. Also, high energy gaps are obtained for films with y/x in region 1.85 to 1.95 (see Fig.5-10).

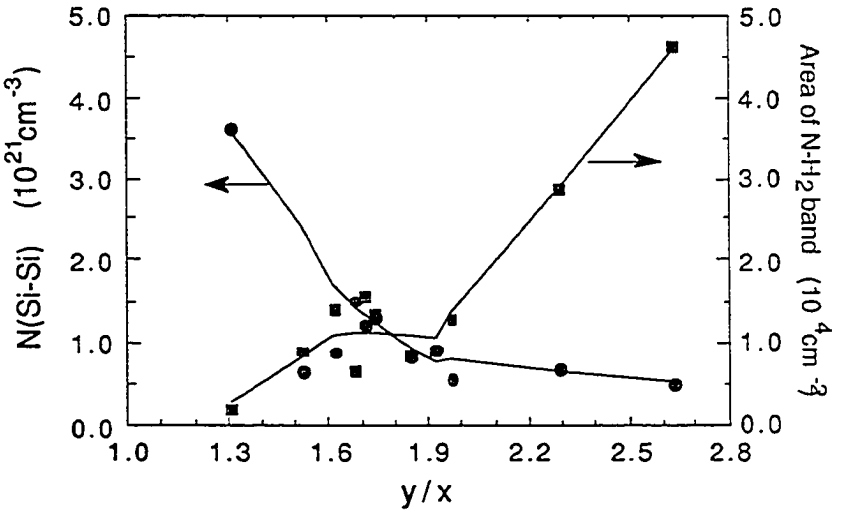

Fig.5-9 Si-Si bond concentrations and the area of the N-$(H)_2$ IR absorption band (at 1550 cm^{-1}) vs the atomic ratio [N]/[Si] y/x, for the films studied.

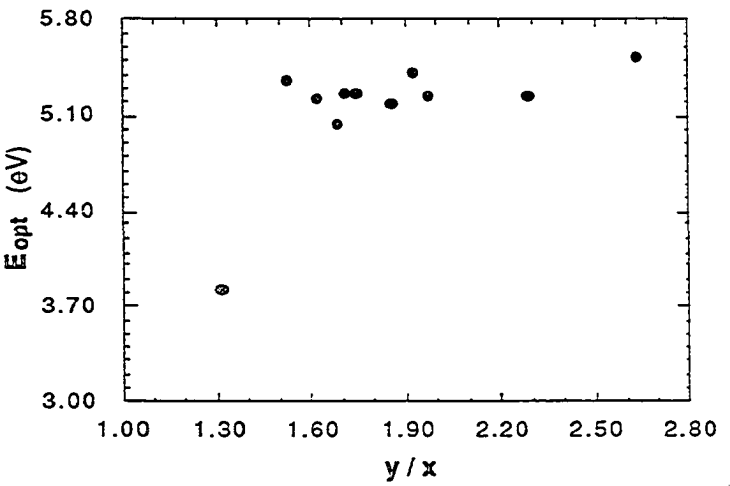

Fig.5-10 Energy gap E_{opt} vs the [N]/[Si] ratio y/x for the films studied.

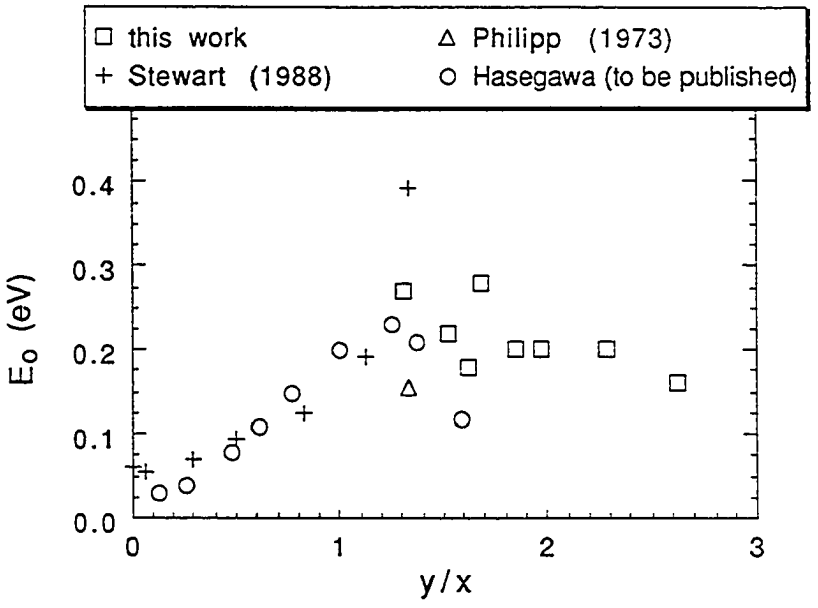

Fig.5-11 The Urbach edge parameter E_0 as a function of y/x for the films studied here and for other researchers (as indicated in figure).

In addition, the Urbach edge parameter E_0 as a function of y/x is shown in Fig.5-11. In order to show E_0 for the whole range of a-$Si_xN_yH_z$ alloys, the results of Hasegawa and of Stewart (Hasegawa et al, to be published; Stewart, 1988) are plotted with our N-rich samples. Philipp's data CVD film result is also included in Fig.5-11. It can be seen that E_0 increases on the Si-rich side and decreases on the N-rich side as the nitrogen content increases. Since E_0 is equal to the slope of the exponential part of the valence-band tail state density (Robertson, 1991) which is due to weak Si-Si bonds, E_0 should increase with the increase of the Si-Si bond concentration N(Si-Si) in N-rich alloys. This is in fact observed in Fig.5-12. Therefore, we can conclude from our experimental results (Fig. 5-3B, 5-6B, 5-7, 5-8B)

that in order to get high quality films, the optimum deposition parameters are: (1) substrate temperature of about 350 °C. (2) high gas ratio R (above 40). (3) high power density (about 0.63W/cm^2); and (4) low absolute SiH_4 flow rate (below 2.5 sccm).

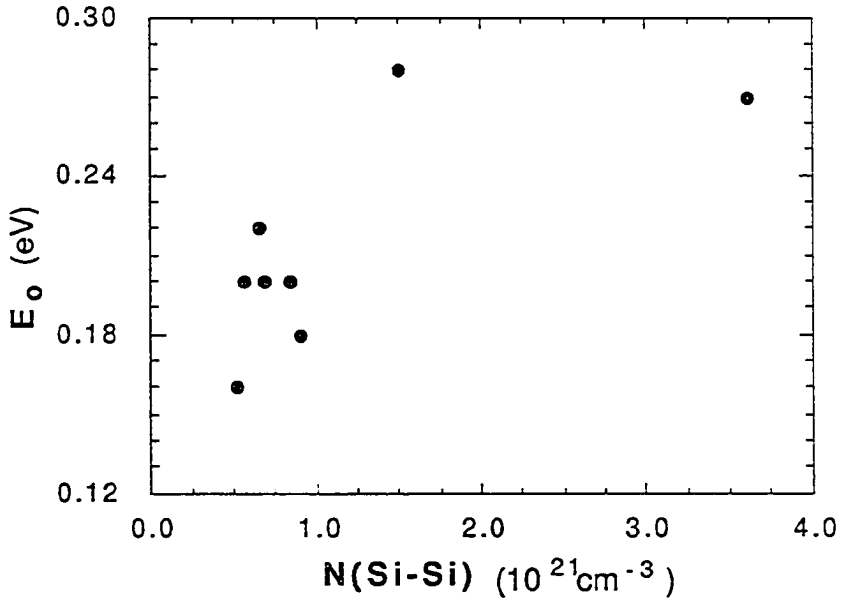

Fig.5-12 The Urbach edge parameter E_o vs the Si-Si bond concentrations for the films studied.

Chapter 6 Tetrahedron Model for the Optical Dielectric Function of a-$Si_xN_yH_z$

6.1. Introduction

Amorphous Si-based alloys are of great current interest not only due to their important applications but also as widely studied examples of primarily tetrahedrally coordinated amorphous semiconductors. Studies of the optical response of such alloy films have provided a wealth of information concerning the microstructure, i.e. local atomic bonding configurations present in the films (Brodsky et al, 1977; Philipp, 1973; Mui and Smith, 1987). In this chapter a microstructural model based on a random mixture of Si-centered tetrahedra will be presented and developed for the optical dielectric function $\varepsilon = \varepsilon_1 - i\varepsilon_2$ of hydrogenated amorphous silicon-nitrogen (a-$Si_xN_yH_z$) alloys. The goal of developing this model is to obtain as clear a correlation as possible between the microstructure and the macroscopic optical response of these films.

In the Si-centered tetrahedron model , the tetrahedra are considered to be the fundamental structural units determining the optical response of the films. This approach was first introduced by Philipp (1971) for amorphous silicon-oxygen-nitrogen films and was further developed by Aspnes and Theeten (1979) who correctly combined it with the Bruggemann effective medium approximation (EMA) (Bruggemann, 1935). The tetrahedron model has already been applied to a-Si:C:H and a-Si:H (Mui and Smith, Phys. Rev, 1987, 1988) alloys for the determination of the optical dielectric function

and to a-Si:H/a-Si:N:H multilayers for the optical response (Mui and Smith, J. Appl. Phys, 1988).

One important new feature of the present work is the explicit incorporation of hydrogen atoms in the Si-centered tetrahedra. In this way it has been possible to study separately the effects on the optical response of varying the film stoichiometry, i.e. the [N]/[Si] ratio, and of varying the H content of the films. In addition, the model has now been extended to include nitrogen-rich films ([N]/[Si] > 4/3). In particular, predictions have been made for the optical response of silicon diimide, $Si(NH)_2$, a compound whose significance for the study of a-$Si_xN_yH_z$ films has been stressed by Tsu et al (1986).

6.2. Tetrahedron Model Development

The goal of the Si-centered tetrahedron model as developed here is to provide an appropriate and convenient framework for calculating ε_1 and ε_2 for the a-$Si_xN_yH_z$ films under consideration. Using the model, it will be possible to explore the effects of varying the film stoichiometry and hydrogen content on the optical response of the alloys. In order to accomplish this, the tetrahedron probabilities P_i will first be derived as functions of the film composition. The ε_i for the tetrahedra will then be obtained using the scaling procedure developed first by Aspnes and Theeten (1979). Then, the P_i and ε_i will be incorporated into the Bruggemann EMA (Bruggemann, 1935) in order to predict the dielectric functions of the a-$Si_xN_yH_z$ alloy films of interest or to estimate the bond

concentrations from measured dielectric function data for a-$Si_xN_yH_z$ alloy films.

6.2.1 Probabilities of Tetrahedra

It is appropriate from the outset to impose some restrictions on the local atomic bonding configurations to be considered for these a-$Si_xN_yH_z$ alloys. In particular, H-H and N-H_3 configurations, i.e. H_2 and NH_3 molecules, are excluded since these units would not be part of the network. Also, N-N single bonds (1.7eV) are excluded from consideration as Si-N (3.5eV) and N-H (4.1eV) bonds are much more stable (see footnote in section 5.2 of chapter 5). Thus, the alloys to be considered do not have completely random bonding, but rather show some significant short-range order.

Each Si atom at the center of a tetrahedron has four valence electrons available, each of which can participate in a bond to one of the following five bonding units: Si(4), H(1), N(3), NH(2), and NH_2(1). The number of valence electrons which each of these units has available for bonding to the network is indicated in parentheses. By distinguishing between the N, NH, and NH_2 bonding units, some potentially important second-nearest-neighbor effects are included in the model. The parameters y_1 and y_2 are defined to be the fractions of N atoms bonded to one or two H atoms, respectively. The contribution of Si dangling bonds to the optical dielectric function is not included in this model since observed spin densities (less than 10^{19} cm^{-3} in hydrogenated and 10^{20} cm^{-3} in hydrogen-free silicon nitride (Hasegawa et al, 1986, 1987 in Appl. Phys.) are small

compared to typical Si-atom concentrations of $(2\text{-}3)\times10^{22}$ cm^{-3} (see chapter 5).

Now, we can write $Si_xN_yH_z = Si_x(N)_{y-y_1-y_2}(NH)_{y_1}(NH_2)_{y_2}H_{z-y_1-2y_2}$, i.e., $(y-y_1-y_2)$ N atoms will bond to 3 Si atoms, y_1 (NH) units will bond to 2 Si atoms, y_2 (NH_2) units will bond to one Si atom, and $(z-y_1-2y_2)$ H atoms will bond to a Si atom. So the fractions of the four bonding units (N, NH, NH_2, and H) bonded to a central Si atom are:

$$f_N = y - y_1 - y_2 \qquad (6\text{-}1a)$$

$$f_{NH} = y_1 \qquad (6\text{-}1b)$$

$$f_{NH_2} = y_2 \qquad (6\text{-}1c)$$

$$f_H = z - y_1 - 2y_2 \qquad (6\text{-}1d)$$

The fraction of Si atoms bonding to other Si atoms f_{Si} is equal to the total fraction x of Si atoms minus the parts which are occupied by the other four units with fractions of $(y-y_1-y_2)$, y_1, y_2, and $(z-y_1-2y_2)$. Since each N unit, (NH) unit, and (NH_2) and H unit will occupy 3/4, 2/4, and 1/4 of a Si atom, respectively, we can write f_{Si} as:

$$f_{Si} = x - \frac{3}{4} f_N - \frac{2}{4} f_{NH} - \frac{1}{4} f_{NH_2} - \frac{1}{4} f_H \qquad (6\text{-}1e)$$

Then, the probabilities of the units bonded to the central Si are equal to the number of bond available for bonding to the center-Si, such as 4 for Si unit, 3 for N unit, 2 for NH unit, and 1 for NH_2 and H units, divided by the total number of bonds given by center-Si, i.e., 4x. They are expressed as follows:

$$p_{Si} = 4f_{Si}/4x \quad (6\text{-}2a)$$

$$p_N = 3f_N/4x \quad (6\text{-}2b)$$

$$p_{NH} = 2f_{NH}/4x \quad (6\text{-}2c)$$

$$p_{NH_2} = f_{NH_2}/4x \quad (6\text{-}2d)$$

$$p_H = f_H/4x \quad (6\text{-}2e)$$

where $\sum p_i = 1$ as expected.

The number of distinct Si-centered tetrahedra which can be constructed from these bonding units is given by N=(n+k-1)!/k!(n-1)!, where n=5 is the number of distinct bonding units and k=4 is the number of valence electrons which the central Si has available for bonding. There are thus N=8!/4!4!=70 possible tetrahedra for a-$Si_xN_yH_z$ alloys. To include all 70 tetrahedra would make the model too complicated to be useful. The model will therefore focus only on some special cases which are reasonably simple yet meaningful enough to correspond to physically-attainable films. The first approximation will made at this stage is to ignore the NH_2 units primarily because little evidence has been found for their existence in the films studied except for the films deposited at low temperature ($T_s \leq 200$ °C). Therefore, in the following text NH_2 will not be considered, i.e., $y_2 = 0$. The probability of the ith tetrahedron, i.e., Si-$(Si)_h(N)_j(NH)_k(H)_l$, is given as:

$$P_i = \frac{4!}{h!\ j!\ k!\ l!} (p_{Si})^h (p_N)^j (p_{NH})^k (p_H)^l \qquad (6\text{-}3)$$

where h, j, k = 0 to 4, l = 0 to 3, and h + j + k + l = 4, i.e., no SiH_4 units.

Another potentially useful approach to bonding in these alloys is to consider N-centered units, of which there are three possibilities: 1) $N\text{-}(Si)_3$, $N\text{-}H(Si)_2$, and $N\text{-}SiH_2$. It is not possible, however, to develop a model for the optical response of the films based only on these three units as Si-Si bonds which absorb strongly in the photon energy range of interest are not explicitly included.

Three special case will now be discussed.

A. a-Si_xN_y ($0 \leq y/x \leq 4/3$)

Hydrogen-free a-Si_xN_y (y = 1-x) films containing only Si-Si and Si-N bonds will be considered first. These include the Si-rich alloys for which the [N]/[Si] ratio y/x is less than the stoichiometric value of 4/3. Since only Si and N are available for bonding to the central Si atom, the number of distinct tetrahedra is N=5!/4!1!=5, corresponding to $Si\text{-}Si_{4-i}N_i$, with i=0 to 4. This case has already been considered in detail by Aspnes and Theeten (1979), and so the presentation here will be brief. The probabilities P_i for these five tetrahedra with $y_1 = y_2 = z = 0$ are listed in Table 6-1 and plotted in Fig.6-1 as functions of the [N]/[Si] ratio y/x ($0 \leq y/x \leq 4/3$). The probabilities p_{Si} and p_N for the Si and N units bonded to the central Si are also listed in Table 6-1.

Table 6-1. The probabilities of units bonded to a central Si atom and the probability P_i of the ith tetrahedron

	p_{Si}	p_N	p_{NH}	p_H	P_i
A.$Si\text{-}Si_{4-i}N_i$	$\frac{4x-3y}{4x}$	$\frac{3y}{4x}$	0	0	$\frac{4!}{(4-i)!i!}\left(\frac{4x-3y}{4x}\right)^{4-i}\left(\frac{3y}{4x}\right)^{i}$
B. $Si\text{-}N_{4-i}(NH)_i$	0	$\frac{3(y-z)}{4x}$	$\frac{z}{2x}$	0	$\frac{4!}{(4-i)!i!}\left(\frac{3(y-z)}{4x}\right)^{4-i}\left(\frac{z}{2x}\right)^{i}$
C. $Si\text{-}Si(NH)_3$	$\frac{4x-3y+z}{4x}$	$\frac{3(y-z)}{4x}$	$\frac{z}{2x}$	0	$4\left(\frac{4x-3y+z}{4x}\right)\left(\frac{z}{2x}\right)^{3}$
$Si\text{-}SiN(NH)_2$	$\frac{4x-3y-z+2y_1}{4x}$	$\frac{3(y-y_1)}{4x}$	$\frac{y_1}{2x}$	$\frac{z-y_1}{4x}$	$12\left(\frac{4x-3y-z+2y_1}{4x}\right)\left(\frac{3(y-y_1)}{4x}\right)\left(\frac{y_1}{2x}\right)^{2}$
$Si\text{-}HN(NH)_2$					$12\left(\frac{3(y-y_1)}{4x}\right)\left(\frac{y_1}{2x}\right)^{2}\left(\frac{z-y_1}{4x}\right)$
$Si\text{-}HN_2(NH)$					$12\left(\frac{3(y-y_1)}{4x}\right)^{2}\left(\frac{y_1}{2x}\right)\left(\frac{z-y_1}{4x}\right)$
$Si\text{-}SiN_2(NH)$					$12\left(\frac{4x-3y-z+2y_1}{4x}\right)\left(\frac{3(y-y_1)}{4x}\right)^{2}\left(\frac{y_1}{2x}\right)$
$Si\text{-}Si_2N_2$					$6\left(\frac{4x-3y-z+2y_1}{4x}\right)^{2}\left(\frac{3(y-y_1)}{4x}\right)^{2}$

B. $a\text{-}Si_xN_{y-z}(NH)_z$ $(4/3 \le y/x \le 2)$

The incorporation of hydrogen in the films will now be explicitly considered by including the bonding of H in the Si-centered tetrahedra. For N-rich (N/Si>4/3) films which are typically prepared

via plasma-enhanced CVD using low SiH_4 flow rate (less than 4 sccm) and high ratios R, the films can be shown to essentially contain only Si-N and N-H bonds (see table 5-2). Therefore, Si-H and Si-Si bonds can be ignored to a first approximation. In addition, only two units will be allowed to bond to the central Si, namely N and NH. The number of distinct tetrahedra is again five, given by $Si\text{-}N_{4-i}(NH)_i$ with i=0 to 4. Note that the i=4 tetrahedron, i.e., $Si\text{-}(NH)_4$, corresponds to silicon diimide, $Si(NH)_2$. The results for the probabilities of the N and NH units (here $y_1 = z$, $y_2 = 0$) bonded to the central Si atom and the probabilities P_i of the five tetrahedra are listed in Table 6-1. Note that $P_{Si} = 0$ yields the supplemental condition that 4x-3y+z=0. The P_i for these tetrahedra are shown in Fig.6-1 as functions of the [N]/[Si] ratio y/x ($4/3 \leq y/x \leq 2$) together with the Si-rich alloys discussed in case A.

C. Tetrahedra containing Si-H or Si-Si bonds

For films prepared using high SiH_4 flow rates (greater than or equal to 4 sccm), experiments (see Table 5-1 and Table 5-2) indicate that Si-H and Si-Si bonds will be present in the films in addition to Si-N and N-H bonds. Six tetrahedra which have been used in the EMA to fit our measured ε_1 and ε_2 for the N-rich films studied will be given here. These tetrahedra include two containing Si-H bonds ($Si\text{-}HN(NH)_2$ and $Si\text{-}HN_2(NH)$) and four containing Si-Si bonds ($Si\text{-}Si(NH)_3$, $Si\text{-}SiN(NH)_2$, $Si\text{-}SiN_2(NH)$, and $Si\text{-}Si_2N_2$). The results for the probabilities are also listed in Table 6-1.

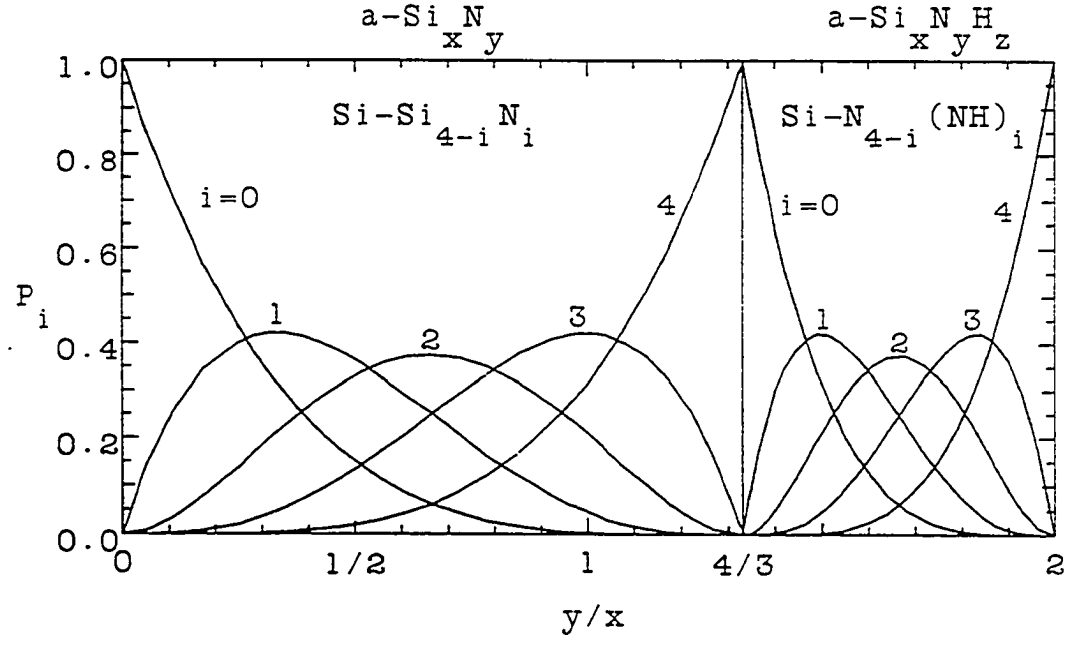

Fig.6-1 Probabilities P_i for Si-centered tetrahedra as functions of [N]/[Si] ratio y/x. Left-hand side of figure: Si-$Si_{4-i}N_i$ (i=0-4) tetrahedra in a-Si_xN_{1-x} alloys for $0 \leq y/x \leq 4/3$. Right-hand side of figure: Si-$N_{4-i}(NH)_i$ (i=0-4) tetrahedra in a-$Si_xN_{y-z}(NH)_z$ alloys for $4/3 \leq y/x \leq 2$.

6.2.2 The Scaling of ε_i for the Tetrahedra

Since the ε_i for the individual tetrahedra are in general not available from experiment, the scaling approach of Aspnes and Theeten (1979) along with the dielectric model of Phillips (1968, 1970), van Vechten (1969), and Levine (1973) (PVVL) will be used to obtain the ε_i by scaling from the measured ε of a-Si for Si-rich tetrahedra ($y/x < 4/3$) and a-Si_3N_4 for N-rich tetrahedra ($y/x > 4/3$).

The scaling approach is based on the expression:

$$\varepsilon_i(E) - 1 = C_{1i} [\varepsilon_{exp} (C_{2i}E) - 1] \qquad (6\text{-}4)$$

where E is the photon energy and ε_{exp} is the measured ε for a-Si or a-Si_3N_4. We use the data of Aspnes et al (1984) for CVD a-Si for $\varepsilon_{a\text{-}Si}$ and the data of Philipp (1973) for CVD a-Si_3N_4 for $\varepsilon_{a\text{-}Si_3N_4}$. C_{1i} and C_{2i} are the scaling parameters for amplitude and energy, respectively, appropriate for the ith tetrahedron. They are given by (Mui and Smith, 1987):

$$C_{1i} = \frac{n_i}{n(a\text{-}Si)} C_{2i}^2 \quad \text{or} \quad C_{1i} = \frac{n_i}{n(a\text{-}Si_3N_4)} C_{2i}^2 \qquad (6\text{-}5a)$$

$$C_{2i} = \frac{E_g(a\text{-}Si)}{E_{gi}} \quad \text{or} \quad C_{2i} = \frac{E_g(a\text{-}Si_3N_4)}{E_{gi}} \qquad (6\text{-}5b)$$

where n_i, n(a-Si), and n(a-Si_3N_4) are the densities of bonding electrons associated with the ith tetrahedron, with Si-Si_4 (a-Si), and with Si-N_4 (a-Si_3N_4), respectively. E_g is the average energy-gap parameter in the PVVL dielectric model and does not correspond to any particular energy gap in the band structure, but rather is an average over all the bands. E_g can be calculated from the PVVL dielectric model using the following relations:

$$E_g^2 = E_H^2 + C^2 \qquad (6\text{-}6a)$$

$$E_H = (7.123 \text{ eV}) (\langle r \rangle)^{-2.48} \qquad (6\text{-}6b)$$

$$C = (14.4 \text{ eV}) b \exp(-k_s \langle r \rangle)[Z_{si} - m \langle Z \rangle] \frac{1}{\langle r \rangle} \qquad (6\text{-}6c)$$

$$b = 0.089 N_c^2 \qquad (6\text{-}6d)$$

$$k_s = (4 k_f / \pi a_b)^{1/2} \qquad (6\text{-}6e)$$

$$k_f = (3\pi^2 N_e)^{1/3} \qquad (6\text{-}6f)$$

Here E_H and C are the homopolar (covalent) and heteropolar (ionic) parts of E_g. $< r >$ is one half of the average bond length between the central Si atom and the four other atoms bonded to the Si in the tetrahedron, with r(Si-Si) = 1.176 Å, r(Si-N) = 0.867 Å, and r(Si-H) = 0.74 Å We assume here that the Si-N, Si-H, and Si-Si bond distances are not affected by the second neighbor atoms. For example, $< r >$ is equal to $\frac{1}{4}(4\text{-}i)r(Si\text{-}Si) + \frac{1}{4}ir(Si\text{-}N)$ for $Si\text{-}Si_{4-i}N_i$ tetrahedra. $Z_{Si} = 4$ is the valence of Si atoms. $< Z >$ is the average valence of the four bonding units which are bonded to the central Si atom, with $Z_N = 5$, $Z_H = 1$. Since we already assume that r(Si-NH) is the same as r(Si-N), Z_N and Z_{NH} from the Si atom point of view are the same, i.e. $Z_{NH} = Z_N = 5$.

The m appearing in eqn.(6-6c) is in principle the ratio of the bonded atoms A and B (A-B bond only, i.e., no A-A and B-B bonds) in a binary alloy system, i.e., AB_m. Instead of the binary system, we will now apply this approach to a Si-centered tetrahedron to find m. The central Si atom will form four bonds with the following units: Si(4), H(1), N(3), NH(2). The number of bonds which each unit can have with the Si atom at the center of the tetrahedra is indicated in parentheses. For example, m is equal to (4-i)/3 + i/2 = (8+i)/6 for $Si\text{-}N_{4-i}(NH)_i$ tetrahedra, i.e., m = 4/3 = [N]/[Si] for i = 0 and m = 2 = [NH]/[Si] for i=4. Thus m is equal to the number of units which are bonded to the center Si in the tetrahedron. a_b = 0.53 Å in eqn.(6-6e) is the Bohr radius. N_c in eqn.(6-6d) and N_e in eqn.(6-6f) are the

average coordination number and the average density of valence electrons in the tetrahedron. They can be written as follows:

$$N_c = \frac{4 + 3\times N_N + 2\times N_{NH} + N_H}{1 + N_N + N_{NH} + N_H} \qquad (6\text{-}6g)$$

$$N_e = \frac{4 + 3\times N_N + 4\times N_{NH} + N_H}{\text{volume of tetrahedron}} \qquad (6\text{-}6h)$$

where N_{Si}, N_N, N_{NH}, and N_H are the number of Si, N, NH, and H units in the tetrahedron. For example, $N_{Si} = 1$, $N_N = \frac{4-i}{3}$, and $N_{NH} = \frac{i}{2}$ are the number of the corresponding units in a $Si\text{-}N_{4-i}(NH)_i$ tetrahedron.

One can see from the above equations that the lone-pair electrons associated with the N atoms have not been included here in the dielectric model even though they have been predicted to lie near the top of the valence band for stoichiometric films and thus might be expected to contribute to the optical response. Aspnes and Theeten (1979) have attempted to indirectly include the lone-pair electrons in the model by using the measured ε of $a\text{-}Si_3N_4$ for the contribution of the Si-N bonds. Martin-Moreno et al (1987) have pointed out, however, that the lone-pair contribution to the optical response can be neglected to a large degree due to a low cross-section for transitions from the lone-pair states to the states lying at the bottom of the conduction band, which are spatially separated from them.

Table 6-2. Tetrahedron volumes V_i and scaling parameters for $Si\text{-}Si_{4-i}N_i$ tetrahedra.

Tetrahedron	V_i ($Å^3$)	<r> (Å)	E_H (eV)	C (eV)	E_g (eV)	C_1	C_2
$Si\text{-}Si_4$	20.02	1.176	4.76	0	4.76	1.00	1.00
$Si\text{-}Si_3N$	21.08	1.099	5.64	0.94	5.72	0.824	0.832
$Si\text{-}Si_2N_2$	22.12	1.022	6.75	2.16	7.09	0.610	0.671
$Si\text{-}SiN_3$	23.18	0.944	8.22	3.91	9.10	0.413	0.523
$Si\text{-}N_4$	24.24	0.867	10.15	6.50	12.05	0.257	0.395

The results of the scaling of ε_i for the tetrahedra which were discussed in the previous section will now be given.

A. a-Si_xN_y ($0 \leq y/x \leq 4/3$)

The results for V_i, <r>, E_H, C, E_g, C_{1i}, and C_{2i} for the five tetrahedra, $Si\text{-}Si_{4-i}N_i$, i = 0-4, are listed in Table 6-2. In Fig. 6-2 the scaling predictions for ε_1 and ε_2 for the five tetrahedra are given as functions of photon energy E. The curves for i=0 correspond to the data of Aspnes et al (1984) for hydrogen-free CVD a-Si. It is apparent that the maxima in both ε_1 and ε_2 decrease in magnitude and shift to higher energies as stronger Si-N bonds replace weaker Si-Si bonds, as expected. In a previous work (Mui and Smith, 1988) the ε_1 and ε_2 spectra for these tetrahedra were scaled from a-Si:H in order to at least partially account for the effects of hydrogen bonded in the films. Since the effects of hydrogen are now explicitly included in the model, it is more appropriate now to scale from a-Si. The

spectra shown for the i=4 tetrahedron, Si-N_4, correspond to a-Si_3N_4. The measured spectra obtained by Philipp (1973) for CVD a-Si_3N_4 are shown for comparison.

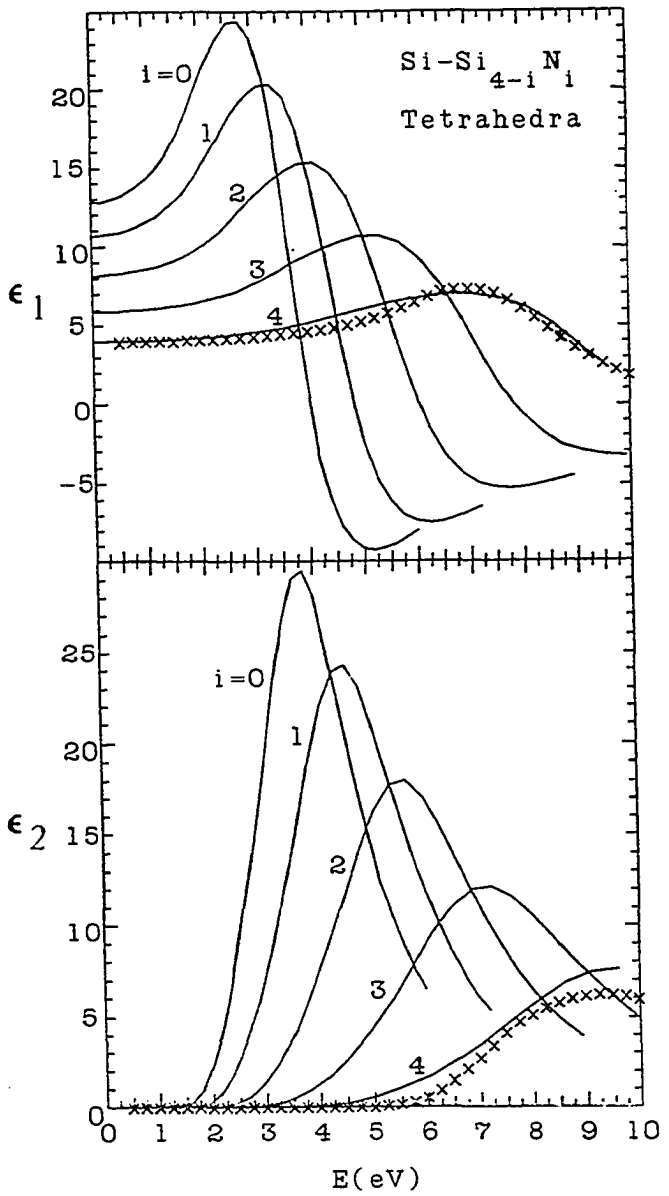

Fig.6-2 Real part ε_1 and imaginary part ε_2 of the dielectric function vs energy E for Si-centered tetrahedra Si-$Si_{4-i}N_i$ (i=0-4), obtained by scaling from a-Si. The experimental data of Philipp CVD a-Si_3N_4 (×) are included for comparison with the predictions for the i=4 tetrahedron Si-N_4.

B. a-$Si_xN_{y-z}(NH)_z$ (4/3 ≤ y/x ≤ 2)

The results for V_i, E_H, C, E_g, C_{1i}, and C_{2i} for the five tetrahedra, $Si\text{-}N_{4-i}(NH)_i$ i = 0-4, are listed in Table 6-3. Note that <r> = 0.867 Å for all five tetrahedra. The volume V_o=27.25 $Å^3$ for $Si\text{-}N_4$ has been obtained by using a density of 2.86 g/cm^3 for a-Si_3N_4 (Niihara et al, 1976). For $Si\text{-}(NH)_4$, i.e. $Si(NH)_2$, a measured density of 2.08 g/cm^3 for a N-rich film prepared at R = 40, T_s = 400 °C, P = 0.5 Torr, and power density = 0.43 W/cm^2 was used to yield V_4=48.81 $Å^3$. This analysis has made use of IR absorption results to obtain experimental values for the P_i for this film.*

---

* The density of an alloy is given by

$$\rho = \sum_i v_i \rho_i = \sum_i v_i \frac{m_i}{V_i} \qquad (1)$$

where m_i and V_i are the mass and volume of the ith tetrahedron, respectively, and v_i is the volume fraction of the ith tetrahedron in the alloy. When v_i which is given by

$$v_i = \frac{P_i V_i}{\sum_j P_j V_j} \qquad (2)$$

is substituted into the (1), then:

$$\rho = \frac{\sum_i P_i m_i}{\sum_j P_j V_j} \qquad (3)$$

or

Table 6-3. Tetrahedron volumes V_i and scaling parameters for $Si\text{-}N_{4-i}(NH)_i$ tetrahedra

Tetrahedron	V_i (Å^3)	E_H (eV)	C (eV)	E_g (eV)	C_1	C_2
$Si\text{-}N_4$	27.25	10.15	6.75	12,19	1.00	1.00
$Si\text{-}N_3(NH)$	32.64	10.15	7.87	12.84	0.846	0.949
$Si\text{-}N_2(NH)_2$	38.03	10.15	8.69	13.36	0.745	0.912
$Si\text{-}N(NH)_3$	43.42	10.15	9.29	13.76	0.677	0.886

$$\sum_i m_i P_i = \rho \sum_j P_j \; V_j \qquad (4)$$

For the sample prepared at R=40, P=0.5 Torr, T_s=400 °C, and power density=0.43 W/cm^2, we assume that no Si-H and Si-Si bonds are present in the film, i.e., only five tetrahedra, $Si\text{-}N_{4-i}(NH)_i$ i=0 to 4, are assumed to be present in this film. Therefore we can write:

$$\sum_{j=0}^{4} P_j \; V_j = P_o \, V_{sin} + P_1 \left(\tfrac{3}{4} V_{sin} + \tfrac{1}{4} V_{sinh}\right) + P_2 \left(\tfrac{1}{2} V_{sin} + \tfrac{1}{2} V_{sinh}\right)$$

$$+ P_3 \left(\tfrac{1}{4} V_{sin} + \tfrac{3}{4} V_{sinh}\right) + P_4 \, V_{sinh} \qquad (5)$$

where $V_{sin} = V_0$ and $V_{sinh} = V_4$ are the volume of the $Si\text{-}N_4$ and $Si\text{-}(NH)_4$ tetrahetra,respectively (see Table 6-3). From (4) and (5) we obtain

$$V_{sinh} = \frac{\frac{1}{\rho}\sum_{i=0}^{4} m_i P_i - \left[P_o + \frac{3}{4}P_1 + \frac{1}{2}P_2 + \frac{1}{4}P_3\right] V_{sin}}{\frac{1}{4}P_1 + \frac{1}{2}P_2 + \frac{3}{4}P_3 + P_4} \qquad (6)$$

The composition parameters x, y, and z can be obtained by using our IR results along with equation (5-10) to (5-13) and then the P_i can be obtained from Table 6-1. Finally, V_{sinh} = 48.81 Å^3 was obtained by using equation (6).

ε_1 and ε_2 for the $Si\text{-}N_{4-i}(NH)_i$ tetrahedra have been scaled from the measured ε of Philipp for a-Si_3N_4 (1973), with the results presented in Fig. 6-3. The spectra shown for i=4 correspond to the predictions of the model for a-$Si(NH)_2$. The gradual shifts of the maxima in both ε_1 and ε_2 to higher energies reflect increases in E_g and the average Si-N bond energy as the Si-N bond becomes more ionic. This prediction is in agreement with that of Robertson (1981) who found an energy gap in the density of states for the $Si\text{-}N_3(NH)$ tetrahedron (equivalent to his Si_2N_3H case) which was larger than that of $Si\text{-}N_4$.

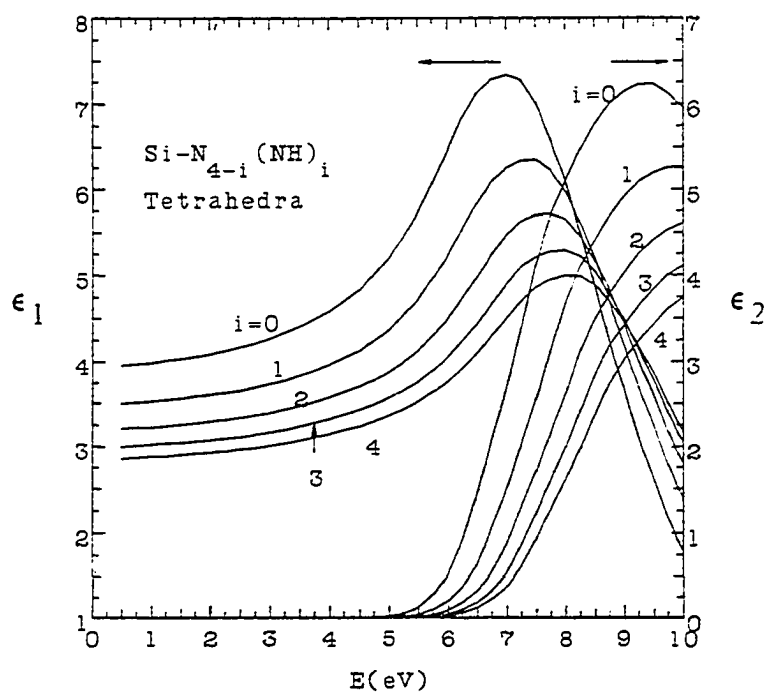

Fig.6-3 Real part ε_1 and imaginary part ε_2 of the dielectric function vs energy E for Si-centered tetrahedra $Si\text{-}N_{4-i}(NH)_i$ (i=0-4), obtained by scaling from a-Si_3N_4.

C. The Six Tetrahedra Discussed in 6.2.1.C

In Table 6-4, the results for V_i, <r>, E_H, C, E_g, C_{1i}, and C_{2i} for the six tetrahedra which were discussed in section 6.2.1.C are listed. The ε spectra for the six tetrahedra listed in Table 6-4, again obtained by scaling from Philipp's data for a-Si_3N_4 (Philipp, 1973), are shown in Fig. 6-4. Note that the ε_1 and ε_2 spectra for tetrahedra containing 0, 1, or 2 Si-Si bonds are quite distinct from each other.

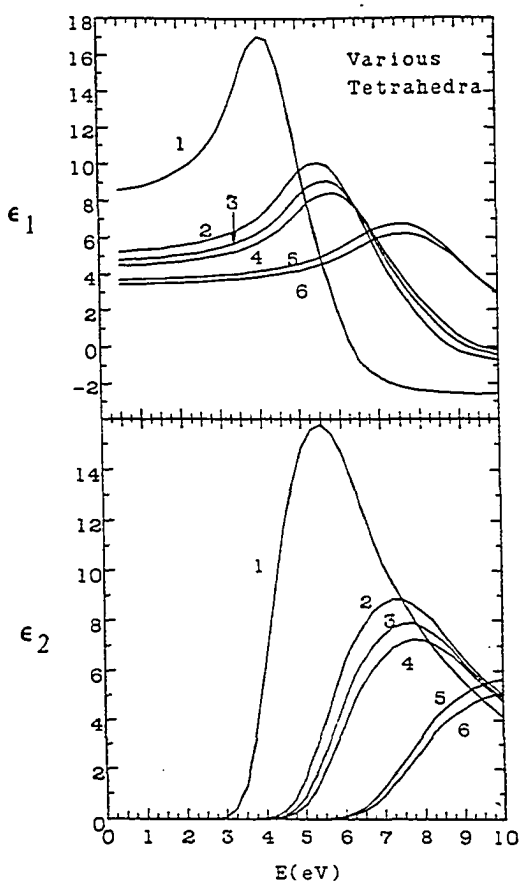

Fig.6-4 Real part ε_1 and imaginary part ε_2 of the dielectric function vs energy E for six Si-centered tetrahedra, numbered as follows: (1) Si-Si_2N_2; (2) Si-SiN_2(NH); (3) Si-$SiN(NH)_2$; (4) Si-$Si(NH)_3$; (5) Si-HN_2(NH); (6) Si-$HN(NH)_2$.

Table 6-4. Tetrahedron volumes V_i and scaling parameters for several Si-centered tetrahedra

Tetrahedron	V_i (Å^3)	<r> (Å)	E_H (eV)	C (eV)	E_g (eV)	C_1 [a]	C_2 [a]
Si-$HN(NH)_2$	34.34	0.835	11.13	7.38	13.36	0.826	0.912
Si-$HN_2(NH)$	28.95	0.835	11.13	7.01	13.16	0.908	0.926
Si-$Si(NH)_3$	41.61	0.944	8.21	6.03	10.19	1.171	1.196
Si-$SiN(NH)_2$	36.22	0.944	8.21	5.59	9.93	1.274	1.227
Si-$SiN_2(NH)$	30.83	0.944	8.21	4.95	9.59	1.428	1.271
Si-Si_2N_2	23.64	1.022	6.76	2.22	7.11	2.539	1.714

[a] Note that $C_1 = C_2 = 1$ corresponds to Si-N_4.

6.3 EMA Analysis of the Optical Dielectric Function

In addition to the predictions of the tetrahedron model for the ε_1 and ε_2 spectra for the individual tetrahedra which have already been presented in Figs 6-2, 6-3, and 6-4, predictions for specific a-$Si_xN_yH_z$ alloys can be obtained by using the EMA to determine the optical response of homogeneous mixtures of tetrahedra. Also, one can obtain important information concerning the microstructure of the a-$Si_xN_yH_z$ films by using the EMA analysis based on Si-centered tetrahedra. The Bruggemann EMA (Bruggemann, 1935) for the dielectric function ε of the alloy is given by

$$\sum_i v_i \frac{\varepsilon_i - \varepsilon}{\varepsilon_i + 2\varepsilon} = 0 \qquad (6\text{-}7a)$$

$$\sum_i v_i = 1 \qquad (6\text{-}7b)$$

where v_i and ε_i are the volume fraction and the complex optical dielectric function, respectively, of the ith component, and ε is the measured value for the film. The sum is over all the possible tetrahedra in the alloy. For an a-$Si_xN_yH_z$ alloy, the $v_i(x, y, z)$ to be used in the EMA are given in terms of the $P_i(x, y, z)$, the probability of the ith tetrahedron, and the V_i, the volume of the ith tetrahedron, by

$$v_i(x,y,z) = \frac{P_i(x, y, z)V_i}{\sum_i P_i(x, y, z)V_i}. \qquad (6\text{-}8)$$

We will also make use of the following relationship for the measured film density ρ:

$$\sum_i v_i \rho_i = \rho \qquad (6\text{-}9)$$

where ρ_i is the density of the ith tetrahedron and ρ the measured density for the film.

The goal of this EMA analysis is to obtain independent estimates for bond and atom concentrations, especially the concentration for the Si-Si bond. We note that there is no direct

method available to determine the concentration of Si-Si bonds in these alloys. It should also be pointed out that an advantage of the EMA analysis is that information can be obtained concerning not only the concentrations of bonds and atoms, but also the manner in which the bonds and atoms are incorporated into the Si-centered tetrahedra.

A computer fitting program is used for the EMA analysis, which first reads in the experimental dielectric function ε data from 1.5 to 6.25 eV and the measured density ρ. Initial values are chosen for the fitting parameters x, y, and y_1 (z = 1-x-y). Then the ε_i and ρ_i for specific tetrahedra which are assumed to be present in the film will be used in eqn.(6-7)-(6-9) along with the measured ε, ρ, and fitting parameter x, y, and y_1 in order to determine the tetrahedron volume fractions v_i for the films under consideration. After obtaining the v_i, the Si-Si bond concentration is equal to:

$$N(\text{Si-Si}) = \sum_i \frac{N_i(\text{Si-Si})}{2} \frac{v_i}{V_i} \qquad (6\text{-}10)$$

where the sum is over all the tetrahedra which contain Si-Si bonds. N_i(Si-Si) is the number of Si-Si bonds in the ith tetrahedron. The factor of 1/2 is included in order to avoid double counting since each Si-Si bond is shared by two tetrahedra.

The results of the EMA analysis for specific alloys and also for our N-rich alloy films will be presented in the following two sections.

6.4 The Predictions of the EMA

Using the EMA, one can predict the dielectric function for a particular alloy of interest. Two special cases will now be considered.

A. a-Si_xN_y ($0 \leq y/x \leq 4/3$)

The predicted ε_1 and ε_2 for several a-Si_xN_y alloys with y/x lying between 0 (a-Si) and 4/3 (a-Si_3N_4) are presented in Fig. 6-5. The spectra evolve smoothly as y/x increases from 0 to 4/3, reflecting the smooth evolution of the ε_i for the tetrahedra shown in Fig. 6-2. The agreement between the i=4 spectra and the measured spectra for a-Si_3N_4 of Philipp (1973) shown in Fig. 6-2 is quite good with regard to the shift of the energy scale, given by C_2. The agreement for the magnitude of ε_1 is also good, while the measured ε_2 lies somewhat below the prediction of the model. The assumption of the model that the lone-pair electrons of the nitrogen atoms do not contribute significantly to the optical response of the alloys thus appears to be consistent with experiment.

The predicted variations of the optical energy gap E_{opt} and the static index of refraction n are shown in Fig.6-6 as functions of the [N]/[Si] ratio, y/x. n is predicted to decrease almost linearly with [N]/[Si], in agreement with experiments on amorphous silicon nitride both with and without incorporated H (Davis et al, 1987). E_{opt} is predicted to increase slowly initially and then much more rapidly as the stoichiometric [N]/[Si] ratio of 4/3 is approached, which is in good agreement with other theoretical predictions (Martin-Moreno et al,

1987). This rapid increase in E_{opt} is a clear signal of the disappearance from the film of the more strongly-absorbing Si-Si bonds, see Fig. 6-1, and is qualitatively consistent with a wide range of experimental observations (Davis et al, 1987; Chaussat et al, 1985).

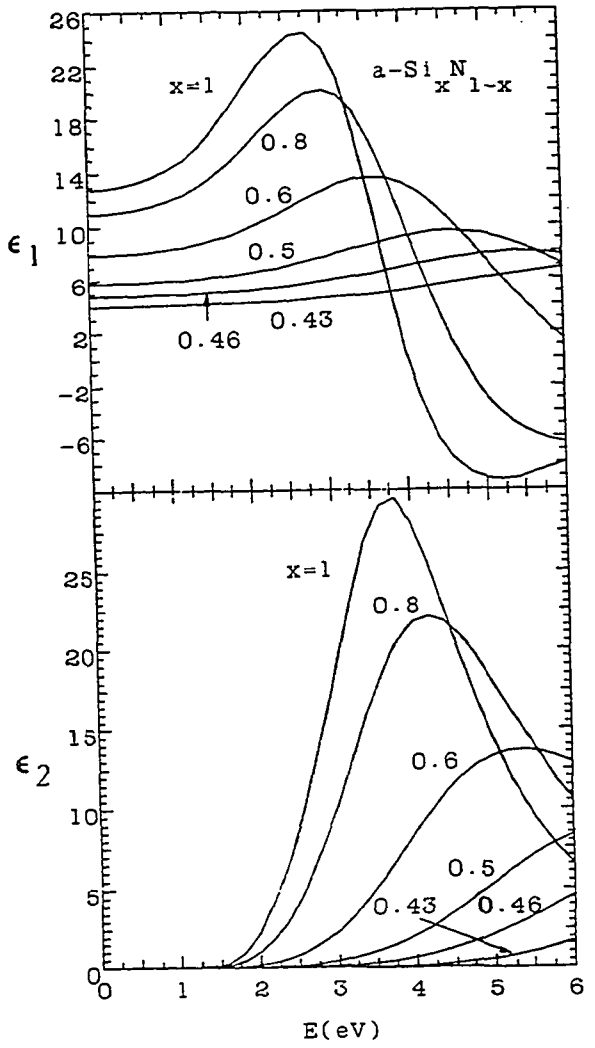

Fig.6-5 Real part ε_1 and imaginary part ε_2 of the dielectric function vs energy E for a-Si_xN_{1-x} alloys, obtained using the EMA. Curves are labeled with the Si fraction x.

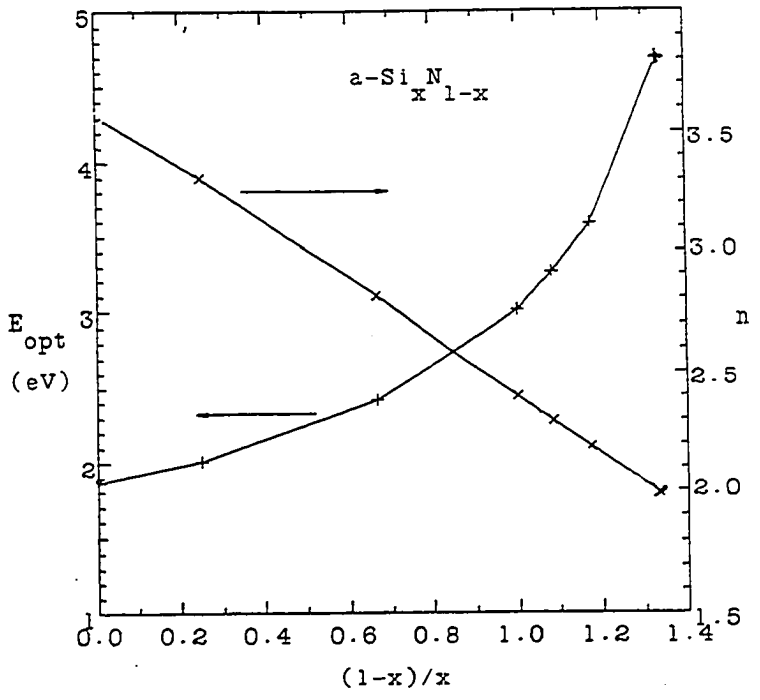

Fig.6-6 Predicted optical energy gap E_{opt} and static index of refraction n vs [N]/[Si] ratio (1-x)/x for a-Si_xN_{1-x} alloys, obtained using the EMA.

B. a-$Si_xN_{y-z}(NH)_z$ (4/3 ≤ y/x ≤ 2)

In Fig. 6-7 are shown the predicted ε_1 and ε_2 for three films with [N]/[Si]=y/x=4/3, 5/3, and 2, corresponding to hydrogen fractions of z=0, 0.273, and 0.4, respectively. Note that these three alloys contain, respectively, all Si-N bonds (a-Si_3N_4), half Si-N and half Si-NH bonds (a-$Si_3N_5H_3$), and all Si-NH bonds (a-$Si(NH)_2$). The predicted values of E_{opt} for these specific alloys, shown in Fig.6-8, are 5.38, 5.88, and 6.17eV, respectively, reflecting an increase in C, the heteropolar or ionic part of E_g. At the same time, the predicted values of n, also shown in Fig. 6-8, decrease from 1.99 to 1.79, and finally to 1.69 for a-$Si(NH)_2$..

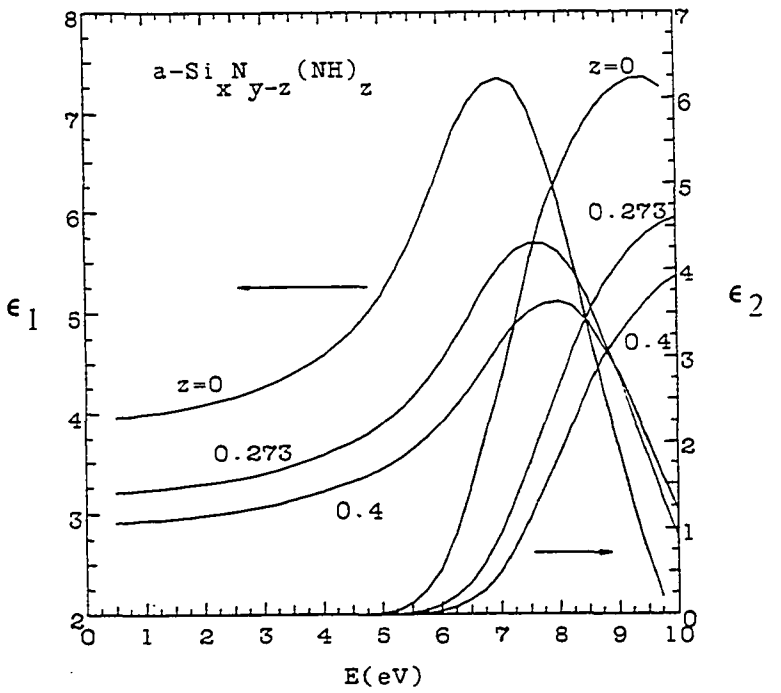

Fig.6-7 Real part ε_1 and imaginary part ε_2 of the dielectric function vs energy E for a-$Si_xN_{y-z}(NH)_z$ alloys, obtained using the EMA. Curves are labeled with the H fraction z, with z=0 corresponding to a-Si_3N_4, z=0.273 to a-$Si_3N_5H_3$, and z=0.4 to a-$Si(NH)_2$.

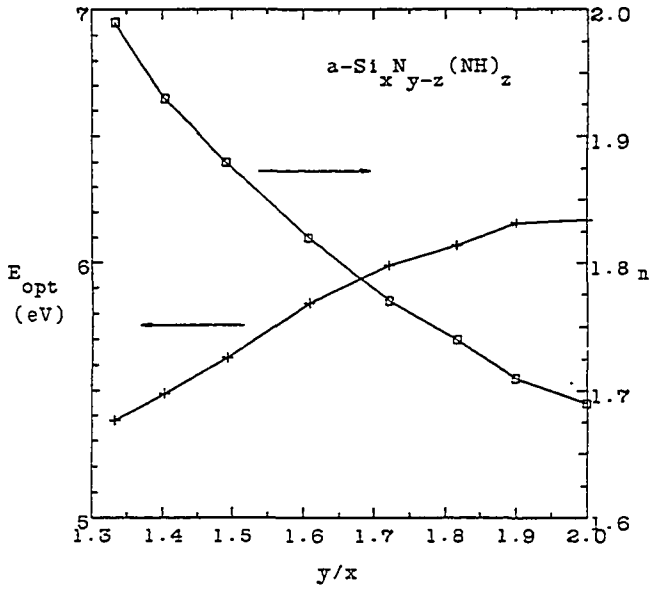

Fig.6-8 Predicted optical energy gap E_{opt} and static index of refraction n vs [N]/[Si] ratio y/x for a-$Si_xN_{y-z}(NH)_z$ alloys.

6.5 EMA Analysis for our a-$Si_xN_yH_z$ Films

The EMA analysis for our films has employed only those tetrahedra which are necessary to model the optical response and which are consistent with the IR results. Three examples of this analysis will be now given.

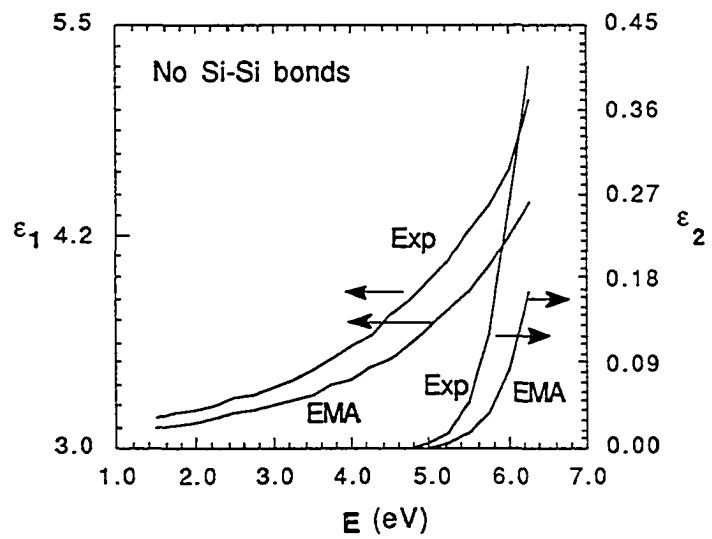

Fig.6-9 Comparison between the measured and fitted dielectric functions ε for sample 3 (R=40, P=0.5 Torr, T_S=400°C, and power=0.43 W/cm^2). Exp, measured ε; EMA, fitted result of EMA analysis without any tetrahedra containing Si-Si bonds.

A. Sample 3 (R=40, P=0.5 Torr, T_S=400 °C, power=0.43 W/cm^2)

For this N-rich a-$Si_xN_yH_z$ film which has no observed Si-H absorption in the IR spectrum, the five Si-centered tetrahedra,

$Si\text{-}N_{4-i}(NH)_i$, i=0 to 4, provide the dominant contribution to the measured ε and ρ. With these five tetrahedra, however, it has not been possible to obtain a satisfactory fit to the measured ε. The comparison between the measured and fitted ε using only these five tetrahedra for this alloy film is shown in Fig.6-9.

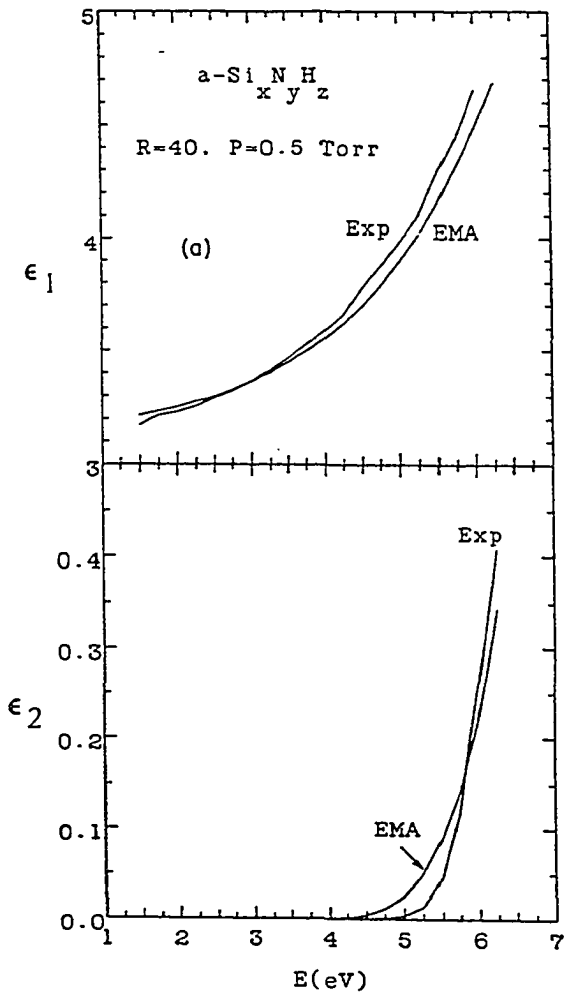

Fig.6-10 Comparison between the measured and fitted dielectric functions ε for sample 3 (R=40, P=0.5 Torr, T_S=400°C, and power=0.43 W/cm^2). Exp, measured ε; EMA, fitted result of EMA analysis including a tetrahedron containing a Si-Si bond.

In order to improve the fitting an additional tetrahedron containing a Si-Si bond has been included in the EMA analysis. Since a high concentration of N-H bonds are present in this sample, the tetrahedron $Si\text{-}Si(NH)_3$ was chosen. The addition of this tetrahedron leads to shifts of the onset of ε_2, i.e., the absorption edge, to lower energies, and the magnitude of ε_1 to higher values, in better agreement with experiment. One can see from Fig.6-10 that satisfactory agreement has been obtained after including this tetrahedron containing a Si-Si bond. The concentration N(Si-Si) of Si-Si bonds resulting from this analysis is 8.3×10^{20} cm^{-3}, which is in fact consistent with the upper limit of 7×10^{21} cm^{-3} estimated from the analysis of the IR absorption and film density measurements (Table 4-1 and 5-1). The results of the EMA fit for the film composition and density for this film all agree with the results presented in Table 5-1 and 5-3 to within experimental error.

B. Sample 2 (R=20, P=0.5 Torr, T_s=400 °C, power=0.43 W/cm^2)

Evidence for the presence of Si-H bonds has been found in the IR absorption spectrum of this film and the density of this film is higher than the density of the previous film, sample 3. Therefore, additional tetrahedra containing Si-H and Si-Si bonds have been used in the EMA analysis. The five $Si\text{-}N_{4-i}(NH)_i$, i=0 to 4, tetrahedra, also used for sample 3, along with two tetrahedra containing Si-Si bonds, $Si\text{-}SiN_2(NH)$ and $Si\text{-}SiN(NH)_2$, and two containing Si-H bonds, $Si\text{-}HN_2(NH)$ and $Si\text{-}HN(NH)_2$, have been employed in the EMA analysis.

The results of this fit are shown in Fig.6-11 and it can be seen that reasonable agreement has been obtained with experiment. For this alloy tetrahedra containing just one Si-Si bond are sufficient to obtain the fit shown and the EMA analysis has yielded N(Si-Si) = 1.5×10^{21} cm^{-3}.

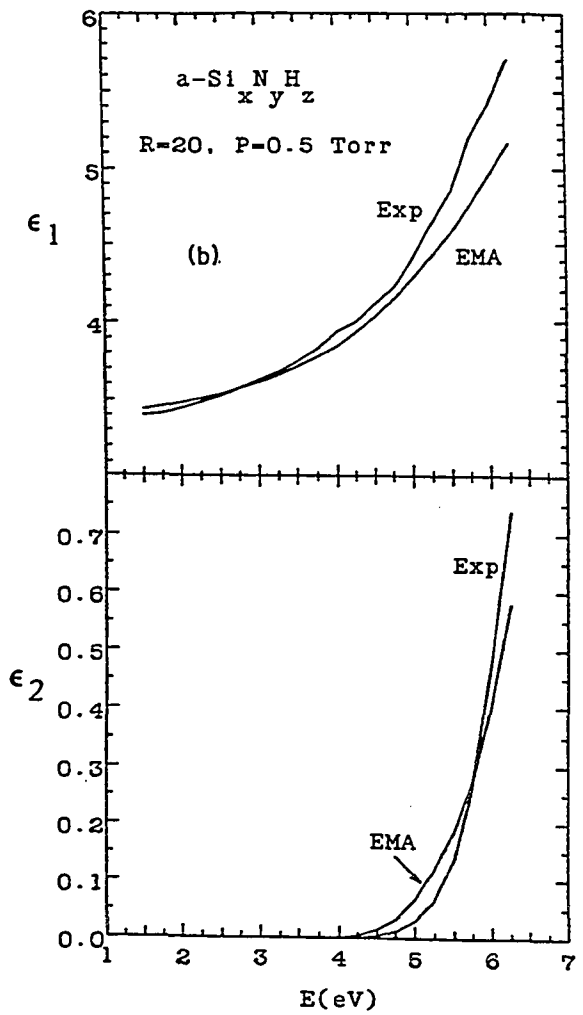

Fig.6-11 Comparison between the measured and fitted dielectric functions ε for sample 2 (R=20, P=0.5 Torr, T_S=400°C, and power=0.43 W/cm^2). Exp, measured ε; EMA, fitted result of EMA analysis.

C. Sample 1 (R=10, P=0.5 Torr, T_S=400 °C, power=0.43 W/cm^2)

For the sample prepared at R=10, P=0.5 Torr, T_S=400 °C, and power=0.43 W/cm^2, the observed Si-H bond IR absorption and the density of the film are higher than those for sample 2. Also, a low concentration of N-H bonds and a high concentration of Si-N bonds relative to samples 2 and 3 appeared for this film (see Table 5-2). Therefore, the following five tetrahedra have been employed: Si-$N_2(NH)_2$, Si-$HN_2(NH)$, Si-$HN(NH)_2$, Si-$SiN_2(NH)$, and Si-Si_2N_2. Although a reasonable fit to the measured ε can be obtained, the fitting procedure is not unique. One result which has been confirmed, however, is that a Si-centered tetrahedron containing two Si-Si bonds is required to obtain even a qualitative fit to the measured ε_2 for this alloy. Also, a void component with a volume fraction of 0.06 has been used to obtain the fit for the alloy. The EMA analysis has yielded N(Si-Si) = 3.6×10^{21} cm^{-3} for this film.

Chapter 7 Free Energy Model for the Bond Concentrations of a-$Si_xN_yH_z$ Alloys

7.1 Introduction

Amorphous covalent network alloys such as a-Si_xH_y and a-$Si_xN_yH_z$ are first and foremost characterized by the absence of long range order (LRO). They can, nevertheless, possess a considerable degree of short range order (SRO) which, in alloys, is generally referred to as chemical ordering (CO) (Betts et al, 1970; Lucovsky et al, 1977). CO usually corresponds to a preference for unlike nearest-neighbor (nn) bonds and results from the tendency to maximize the chemical bonding energy in the alloy. Random bonding, on the other hand, refers to a purely statistical distribution of nn bond types (Betts et al, 1970). While the nn distribution of Si-Si and Si-H bonds in single phase a-Si_xH_y alloys is fixed by the composition (Mui and Smith, 1988) and by the fact that H-H bonds cannot be considered to be part of the network, the distribution of bonds in a-$Si_xN_yH_z$ and similar ternary alloys cannot be determined from the composition alone even if bonds such as H-H and N-N are excluded. This is due to the fact that the division of H into Si-H and N-H bonds cannot be obtained solely from the composition, but must be specified separately. The ability to predict the nn bond distributions in amorphous covalent network alloys is clearly of fundamental importance as an aid in constructing realistic network models and is also of great practical significance since, for example, Si-Si bond concentrations, as discussing in chapter 6, are potentially harmful

defects in a-$Si_xN_yH_x$ films, but their concentration N(Si-Si) can not be directly measured by any available method.

A free energy model (FEM) for bonding in amorphous covalent alloys has been developed. The model includes chemical bonding effects in the enthalpy and effects due to the statistics of bonding within local structural units (in this case Si-centered tetrahedra) in the entropy. While recognizing the obvious fact that these alloys are not in thermodynamic equilibrium, our approach has been to determine the state of lowest free energy among the possible states of the amorphous alloy which lack LRO. The rationale for this approach is that even though the deposition processes typically used for these alloy films are not strictly speaking equilibrium processes, nevertheless the bonding in the film which corresponds to the greatest product stability should be favored.

It is difficult to justify a priori the use of thermodynamics, i.e. free energy minimization, to determine the nature of the bonding in amorphous covalent alloys. It is not suggested here that this type of thermodynamic approach is a substitute for a detailed model including kinetic effects, but rather that it can lead to new insights concerning the nature of chemical ordering and the importance of entropy.

7.2 General Idea of the FEM

The FEM for bonding in amorphous covalent alloys is based on the quasichemical approach to the thermodynamics of regular solutions (Gordon, 1968). The Gibbs free energy of mixing is given by

$$G_M = H_M - TS_M \qquad (7\text{-}1)$$

where H_M and S_M are the enthalpy and entropy of mixing, respectively.

Since the enthalpy $H = E + PV$, where P and V are pressure and volume, respectively, of the system considered and the energy E is made up of the sum of the potential energies between the atoms E^{PE} and their thermal kinetic energies E^{KE}, we may write the mixing enthalpy as

$$H_M = \Delta E^{PE} + \Delta E^{KE} + \Delta(PV) \qquad (7\text{-}2)$$

where Δ refers to the change of a item caused by mixing. For condensed phases PV is small at ordinary pressures, and also generally the change of volume ΔV before and after mixing is small, so that $\Delta(PV) \approx 0$. In the first approximation, we can assume that the change of thermal kinetic energies for atoms before and after mixing is small so that $\Delta E^{KE} \approx 0$. Therefore, the only term considered here is the change of the potential energies caused by mixing for the system. By using the quasichemical approach which was developed by Guggenheim (1935), the potential energy of a system is equal to the sum of the bonding energies E_i for all the pairs in the system. Therefore, we can write

$$H_M = E_{atoms} - E_{bonds} \qquad (7\text{-}3)$$

where E_{atoms} is the sum of the energies of the isolated atoms and E_{bonds} is the sum of the nearest neighbor bond energies in the alloy.

Note that E_{atoms} and E_{bonds} are both positive here, i.e. the negative sign of the bonding energy for atoms and for bonds is already considered so that the absolute value of the energy should be used in eqn.(7-3).

The mixing or configurational entropy S_M is given by

$$S_M = k_b \ln \Gamma \qquad (7\text{-}4)$$

where k_b is the Boltzmann constant and Γ is the number of possible bonding configurations in the system considered. The stable state of an alloy corresponds to the minimum of the Gibbs free energy of mixing. Thus G_M is minimized in the free energy model in order to determine the normalized bond concentrations, i.e. bond fractions, for the a-$Si_xN_yH_z$ alloy of fixed composition x, y, and z.

7.3 Development of the FEM for a-$Si_xN_yH_z$ Alloys.

With three constituents present in the a-$Si_xN_yH_z$ alloys of interest, there are in principle six possible types of nn bond pairs. As discussed in section 5.2 of chapter 5, only four types of bonds (Si-N, Si-H, Si-Si, and N-H) are considered to be present in a-$Si_xN_yH_z$ alloys. In addition, we will assume a fully-coordinated network, so that broken (or dangling) bonds are not considered. While defects such as dangling bonds can have an important influence on the electrical properties of these alloys, their concentrations are typically at the 1% level or lower (see discussion in section 6.2.1 of chapter 6), and hence they will not make a significant contribution to the free energy. E_{bonds} and E_{atoms} in eqn.(7-3) can then be expressed in terms

of the four bond concentrations N(X-Y), the corresponding nn bond energies E(X-Y), the heats of formation of the atoms $H_o(X)$, and the atom concentrations N(X) by

$$E_{bonds} = N(Si\text{-}Si)E(Si\text{-}Si)+N(Si\text{-}H)E(Si\text{-}H) + N(Si\text{-}N)E(Si\text{-}N)+N(N\text{-}H)E(N\text{-}H), \quad (7\text{-}5a)$$

and

$$E_{atoms} = N(Si)H_o(Si) + N(N)H_o(N) + N(H)H_o(H) \quad (7\text{-}5b)$$

where E(Si-Si) = 2.34 eV, E(Si-H) = 3.34 eV, E(Si-N) = 3.45 eV, E(N-H) = 4.05 eV, $H_o(Si)$ = 4.68 eV, $H_o(N)$ = 4.91 eV, and $H_o(H)$ = 2.27 eV (see the footnote in section 5.2 of chapter 5). These nn bond energies are assumed initially to be independent of the local chemical and physical environment of the bonds in the alloy, i.e. the identity of the 2nd nn's and strain effects due to deviations of bond lengths and angles from their "ideal" values. The uncertainties in the bond energies will limit the ability of the model to make quantitative predictions. Extensions of the model to explicitly account for the effects of the bonding environment on these energies will be desirable.

H_M is minimized for a given alloy when the chemical bonding energy E_{bonds} is maximized. This limit corresponds to the maximum possible CO and it will be shown below for a-$Si_xN_yH_z$ that this is equivalent to maximizing the concentrations of Si-N and Si-H bonds,

N(Si-N) and N(Si-H). This result is consistent with the following network bond reaction equation,

$$\text{Si-Si} + \text{N-H} \leftrightarrow \text{Si-N} + \text{Si-H} \qquad (7\text{-}6)$$

for which the change in the energy of the chemical bonds is exothermic in the forward direction. It is important to note that N-H bonds, which are the strongest bonds in the alloy, are nevertheless not favored by CO since they are paired in eqn.(7-6) with Si-Si bonds which are the weakest bonds in the alloy. From eqn.(7-6), it can be seen that the driving force for CO is given by the generalized interaction parameter Ω which can be expressed for a-$Si_xN_yH_z$ by

$$\Omega = E(\text{Si-N}) + E(\text{Si-H}) - E(\text{Si-Si}) - E(\text{N-H}) \qquad (7\text{-}7)$$

When the bond energies listed above are used, a value of Ω = +0.4 eV is obtained. Improved estimates for Ω are obtained below from comparisons of the predictions of the FEM with the results of experiments on a-$Si_xN_yH_z$ alloys. We note that for the simpler A_xB_{1-x} binary alloys (Gordon, 1968), the network bond reaction analogous to eqn.(7-6) is given by A-A + B-B $\leftrightarrow$ 2A-B, and so the interaction parameter is Ω = 2E(A-B) - E(A-A) - E(B-B). In this case if $\Omega > 0$, CO will correspond to a preference for A-B bonds over A-A and B-B bonds.

In order to determine the mixing or configurational entropy S_M, the Si-centered tetrahedra again have been employed as the fundamental structural units in the alloys, as discussed in detail in

chapter 6. The five bonding units, Si, H, N, NH, and NH_2, to the central Si are all considered in the FEM.

It is assumed in the FEM that all four bonding sites in a Si-centered tetrahedron are equivalent, so that according to eqn.(7-4) $S_M = k_b \ln\Gamma_1\Gamma_2\Gamma_3\Gamma_4 = 4k_b \ln\Gamma_1$, with Γ_1 for a single site given by

$$\Gamma_1 = \frac{N(Si)!}{N_{Si}!\, N_H!\, N_N!\, N_{NH}!\, N_{NH_2}!} \qquad (7\text{-}8)$$

where N_i is the concentration of the ith unit bonded to site 1 in the Si-center tetrahedron and N(Si) is the concentration of Si atoms in the alloy. By introducing n_i which is defined as N_i normalized to N(Si), i.e., $n_i = N_i/N(Si)$, then $\sum_i n_i = 1$. Using $\ln(N_i!) \approx N_i \ln(N_i)$, we can then obtain

$$S_M = -4k_b\, N(Si) \sum_i n_i \ln(n_i)\ , \qquad (7\text{-}9)$$

The relations between the concentrations of bonding units and of bonds are given by:

$$N_{Si} = \frac{1}{2} N(Si\text{-}Si) \qquad (7\text{-}10a)$$

$$N_N = \frac{1}{4} N(Si\text{-}(N)Si_2) \qquad (7\text{-}10b)$$

$$N_{NH} = \frac{1}{4} N(Si\text{-}(NH)Si) \qquad (7\text{-}10c)$$

$$N_{NH_2} = \frac{1}{4} N(Si\text{-}(NH_2)) \qquad (7\text{-}10d)$$

$$N_H = \frac{1}{4} N(Si\text{-}H)\ , \qquad (7\text{-}10e)$$

and also:

$$N(Si\text{-}N) = N(Si\text{-}(N)Si_2)+N(Si\text{-}(NH)Si)+N(Si\text{-}(NH_2)) \qquad (7\text{-}11)$$

$$N(N\text{-}H) = \frac{1}{2}N(Si\text{-}(NH)Si) + 2N(Si\text{-}(NH_2)). \qquad (7\text{-}12)$$

From eqn.(7-10) to (7-12), we can get:

$$N(Si\text{-}Si) = 2N_{Si}, \qquad (7\text{-}13a)$$

$$N(Si\text{-}H) = 4N_H, \qquad (7\text{-}13b)$$

$$N(Si\text{-}N) = 4(N_N + N_{NH} + N_{NH_2}), \qquad (7\text{-}13c)$$

$$N(N\text{-}H) = 2N_{NH} + 8N_{NH_2}. \qquad (7\text{-}13d)$$

When eqn.(7-13) and standard relationships between the bond and atom concentrations given by eqn.(5-10) to (5-12) are used, the n_i for the five types of bonding units can be expressed in terms of the composition x,y,z and two additional parameters y_1 and y_2, which were introduced in section 6.2.1 of chapter 6 and defined to be the fractions of N atoms bonded to one or two H atoms, respectively. Equivalently, the two additional parameters y_1 and y_2 can be replaced by s_1 and s_2 which are defined to be $s_1 = N(Si\text{-}Si)/N(Si)$ and $s_2 = N(Si\text{-}(NH_2))/N(Si)$, respectively. The n_i as functions of x, y, z, s_1, and s_2 are given as follows:

$$n_{si} = \frac{1}{2}s_1 \qquad (7\text{-}14a)$$

$$n_N = \frac{3}{4}\left(2 - s_1 - \frac{z}{2x} - \frac{y}{2x} + s_2\right) \qquad (7\text{-}14b)$$

$$n_{NH} = \frac{1}{4}\left(2s_1 - 4 + \frac{3y}{x} + \frac{z}{x} - 4s_2\right) \qquad (7\text{-}14c)$$

$$n_{NH_2} = \frac{1}{4} s_2 \qquad (7\text{-}14d)$$

$$n_H = \frac{1}{4}\left(2 - s_1 + \frac{z}{2x} - \frac{3y}{2x}\right). \qquad (7\text{-}14e)$$

The Gibbs free energy of mixing G_M of a-$Si_xN_yH_z$ can thus be expressed as a function of the composition x,y,z, the two parameters s_1 and s_2, the nn bond energies, and the temperature T. For given x, y, z, and T, the predicted bond concentrations can be calculated once the values of s_1 and s_2 which minimize G_M are found. We note that the T = 0° K limit of the FEM corresponds to $G_M = H_M$ and thus yields the maximum possible CO. The $\Omega = 0$ (or $T \rightarrow \infty$) limit, on the other hand, corresponds to the maximum possible bonding disorder, or simply the random limit.

7.4 Predictions of the FEM and Comparisons with Experiment.

The predictions of the FEM for the bond fractions, i.e. N(Si-X)/N(Si) with X = Si, H, or N, and N(N-H)/N(N), are shown in Fig.7-1 for these a-$Si_xN_yH_z$ alloys (x + y + z = 1) as functions of the N/Si ratio y/x for (a) z = 0, (b) z = 0.2, and (c) z = 0.4, using Ω = +0.40 eV, and T = 300 °C, a typical film deposition temperature. Also included for comparison are the predictions corresponding to maximum CO (T = 0°K) and maximum disorder (Ω = 0). For z = 0, the Si-Si and Si-N bond fractions are completely determined by the composition x since N-N bonds have been excluded. Thus in the absence of hydrogen, the

predictions of the FEM and the random and CO limits all coincide (Fig.7-1a).

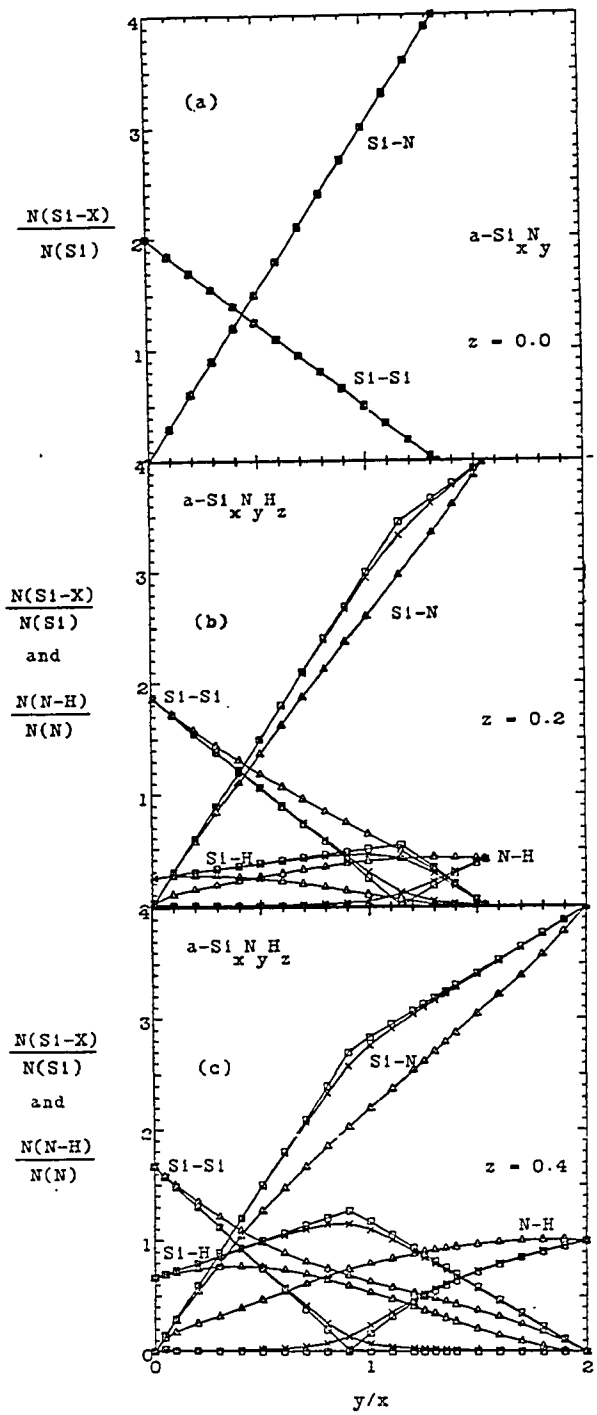

Fig.7-1 Predicted bond fractions N(Si-X)/N(Si), with X=Si, H, or N, and N(N-H)/N(N) as functions of the [N]/[Si] ratio y/x for a-$Si_xN_yH_z$ alloys with (a) z=0, (b) z=0.2, and (c) z= 0.4. Predictions of the FEM are shown for T=300 °C with Ω=+0.40 eV (×××) and also for the random (Ω=0, $\Delta\Delta\Delta$) and CO (T=0 K, □ □ □) limits.

Since the interaction parameter Ω for a-$Si_xN_yH_z$ is relatively large (+0.40 eV), it is not surprising that the T = 300°C predictions for both z = 0.2 and 0.4 lie close to the CO limit over the entire composition range. The random limit can be seen from Fig. 7-1 to correspond for z = 0.2 and 0.4 to significant concentrations of Si-Si bonds even in N-rich alloys and of N-H bonds even in Si-rich alloys. The CO limit, on the other hand, yields no Si-Si or N-H bonds for the same alloys, which, as mentioned before, is equivalent to maximizing N(Si-N) and N(Si-H). The dividing line between what are referred to here as Si-rich and N-rich alloys is a function of z and is given by y/x = (4-5z)/(3-2z). This expression yields y/x = 4/3, as expected, for z = 0 and has been obtained using x+y+z = 1 and 4x-3y-z = 0 which is the condition for having only Si-N and Si-H bonds (and no Si-Si and N-H bonds) in the alloy.

Neither the random nor the CO predictions of the FEM have in fact been found to be valid for plasma-deposited a-$Si_xN_yH_z$ films where small but non-zero concentrations of Si-Si (N-H) bonds are found in N-rich (Si-rich) films from our experiment. It can be seen from Fig.7-1 that the FEM does in fact predict the presence of Si-Si bonds in N-rich films (and N-H bonds in Si-rich films) at 300 °C, in agreement with experiment. We will return to this important point below. From Fig.7-1b, we note that the FEM does not apply for y/x > (4-3z)/(3-4z)=1.54 for z =0.2 since beyond this point N-N bonds would have to be present in the network. This expression is obtained from x + y + z = 1 and 4x - 3y +z =0 which is the condition for having only Si-N and N-H bonds (and no Si-Si or Si-H bonds) in the alloy.

The prediction of the FEM for the fraction of H atoms bonded to Si, N(Si-H)/N(H), is shown in Fig.7-2 as a function of y/x for z = 0.3 and T = 300 °C along with the experimental results of Claassen et al (1983) for a-$Si_xN_yH_z$ films with values of z between 0.2 and 0.4 and deposited at 300 °C. The experimental results are seen to be quite consistent with the FEM prediction when the value of Ω is taken to be +0.25 eV. The predictions of the FEM corresponding to maximum CO and to random bonding are shown in Fig.7-2 to be in poor agreement with experiment. In the limit of maximum CO Si-H (and Si-N) bonds are favored and no N-H bonds are predicted to be present for $y/x < 1.04$, while for random bonding N-H bonds are predicted to be present for all $y/x > 0$. Also, the concentration of Si-H bonds for a fixed composition y/x and z is predicted to decrease with increasing temperature from the CO (T= 0 °K) limit to the random bonding limit ($T \rightarrow \infty$).

Although Ω = +0.40 eV was obtained using the bond energies listed previously, the lower value of +0.25 eV which has been found here to give the best agreement with experiment in Fig.7-2 may be understood if 1) Si-Si or N-H bonds in a-$Si_xN_yH_z$ are stronger than in solid Si or NH_3, respectively, or 2) Si-N or Si-H bonds are weaker in a-$Si_xN_yH_z$ than in Si_3N_4 or SiH_4, respectively. It is very unlikely that Si-Si bonds will be stronger since strain in the alloy will weaken these bonds. Since the electronegativity values for Si, H, and N atoms are 1.8, 2.1, and 3.0, (Eblin, 1970) respectively, N-H bonds are in fact expected to be stronger in the alloy due to the greater transfer of electrons to N from the Si atom(s). Likewise, Si-N bonds are expected

to be weaker in the alloy due to electron transfer to (from) H atoms bonded to the N (Si) atom. Si-H bonds, on the other hand, are expected to be weaker in Si-rich alloys and stronger in N-rich alloys due to electron transfer effects. It is not possible at this point to decide how the above changes in bond strength contribute to the decrease of Ω to +0.25 eV.

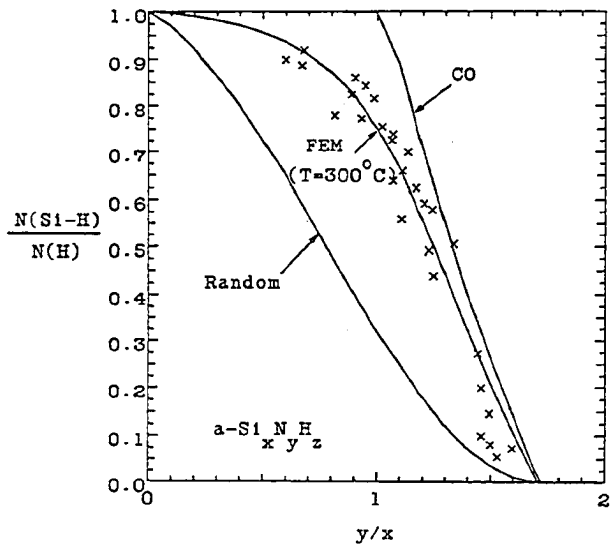

Fig.7-2 The comparison between the predictions of the FEM and the experimental results of Claassen et al (1983, ×××) for N(Si-H)/N(H) as a function of y/x for a-$Si_xN_yH_z$ alloys with z=0.3. The predictions of the FEM are shown for T=300 °C with Ω=+0.25 eV and also for the random (Ω=0) and CO (T=0 K) limits.

Si-Si bonds have been proposed to be potentially harmful defects in the a-$Si_xN_yH_z$ films currently used in device applications (Jousse et al, 1989; D.L. Smith et al, J. Electronic. Mater.1990). The FEM predicts that the number of Si-Si bonds per Si atom actually

increases with increasing H fraction z for N/Si ratios y/x greater than about 1.5 in the technologically-important N-rich alloys (see Fig.7-3). This conclusion can be understood in terms of the following reaction:

$$2\ \text{Si-N} + 2\ \text{H} \rightarrow \text{Si-Si} + 2\ \text{N-H}. \qquad (7\text{-}15)$$

When z increases at fixed y/x in N-rich alloys, the extra H atoms have a very high probability for insertion into Si-N bonds where they will preferentially bond to N atoms. As can be seen from eqn.(7-15), this process leads to the formation of Si-Si bonds. It is also found that the concentrations of N-H and Si-Si bonds are predicted to increase as T increases since these are the bonds favored by entropy.

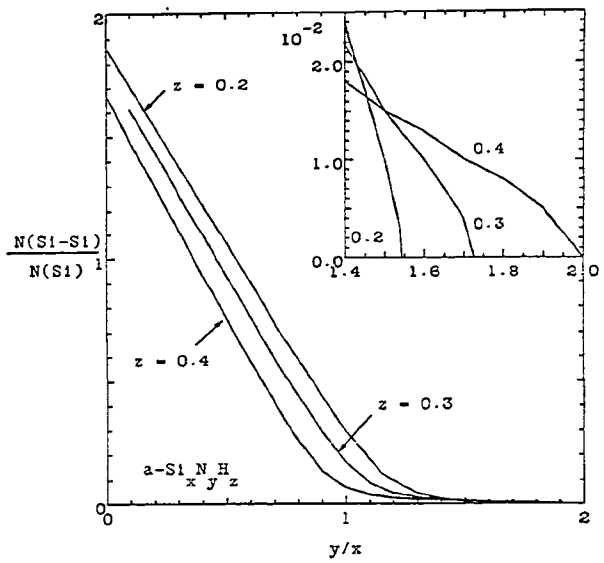

Fig.7-3 N(Si-Si)/N(Si) vs the [N]/[Si] ratio y/x for hydrogen content z=0.2, 0.3, and 0.4. When y/x is greater than about 1.5, Si-Si bonds increase with increasing z (see insert).

Our EMA results for N(Si-Si)/N(Si) are given in Fig.7-4 for the four films studied (samples 1 to 4), which were prepared via plasma-enhanced CVD at 400 °C and a power density of 0.43 W/cm^2, using R = NH_3/SiH_4 ratios of 10, 20, and 40 at P = 0.5 Torr and R = 40 at 0.15 Torr. Also included are the FEM predictions for these films for T = 400 °C with Ω = +0.25 eV and for the random (Ω = 0) and CO (T = 0 °K) limits. For the R = 10 (y/x = 1.31, z = 0.19) and R = 20 (y/x = 1.68, z = 0.34) films, the EMA results for N(Si-Si) agree, to within experimental error, with the T = 400 °C predictions of the FEM, and can be seen to be well below the prediction for the random limit and well above the prediction for the CO limit, which is N(Si-Si) = 0 for these films.

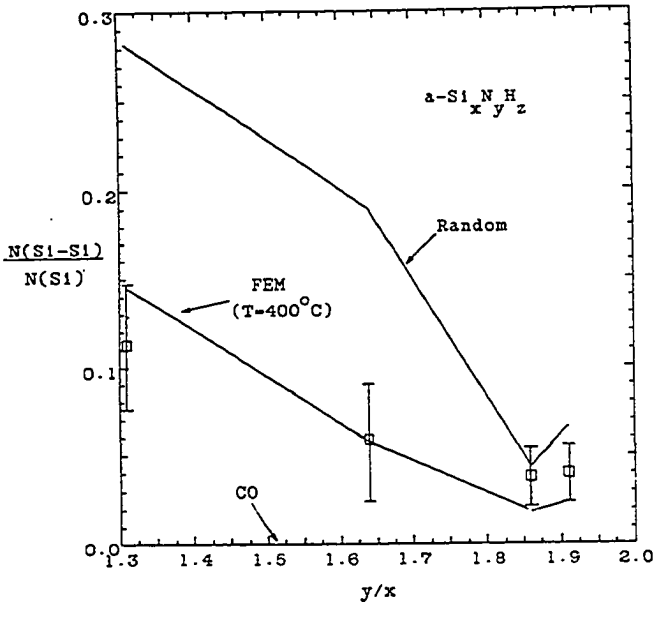

Fig.7-4 Predicted and experimental values (with error bars) of N(Si-Si)/N(Si) for samples 1 to 4 as functions of y/x. The predictions of the FEM for these films are shown for T=400 °C (the film deposition temperature) with Ω=+0.25 eV, and also for the random (Ω=0) and CO (T=0 K) limits.

For the two R = 40 films (y/x = 1.85, z = 0.36 for 0.5 Torr; y/x = 1.92, z = 0.39 for 0.15 Torr) we find instead that the values of N(Si-Si) obtained from the EMA analysis are about a factor of two higher than the T = 400 °C FEM prediction and thus are somewhat more consistent with the random limit prediction. The fact that no Si-H bonds have been observed (see Table 5-2 in chapter 5) in these two films is also in agreement with random bonding. A possible explanation for this result is that $\Omega \rightarrow 0$ for these two films which are quite close in composition to silicon diimide, $Si(NH)_2$, with y/x = 2 and z = 0.4.

Recent experimental analyses (Hasegawa et al, Phil.Mag. 1987; Bustarret et al, 1988) of the bonding in a-$Si_xN_yH_z$ films have indicated that each N atom in Si-rich films has at least one monohydrogenated Si nn. These observations can in fact be shown to be consistent with the tendency for CO in these alloys whereby Si-N and Si-H bonds are favored at the expense of Si-Si and N-H bonds. A specific example of a network bond reaction involving nearest-neighbor Si and N atoms which yields an N atom with one monohydrogenated Si nn can be illustrated as follows,

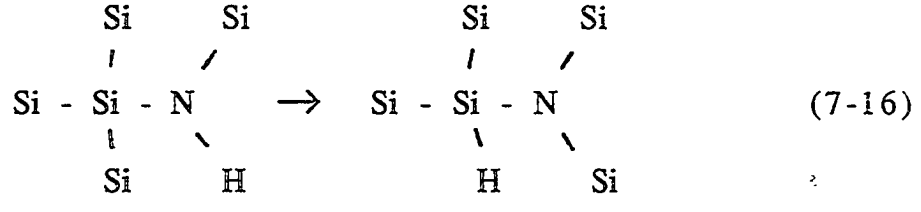

(7-16)

where, for simplicity, only the bonds of the nn Si and N atoms are shown. We note that the change in network bonding expressed in this diagram (Eq.(7-16)) is the same as that given by the simpler network bond reaction Eq.(7-6).

Chapter 8 Conclusions and Suggestions for Further Research

The a-$Si_xN_yH_z$ alloys which are currently used in device-related applications are typically deposited at low temperature, T_s < 400 °C. Therefore, hydrogen is unavoidably incorporated in the amorphous silicon nitride alloy, i.e. a-$Si_xN_yH_z$. The incorporation of H cause the real part of dielectric function ε_1 to shift to lower values and the imaginary part of dielectric function ε_2 to shift to higher energy. Also, we found that the hydrogen bonding effect in a-$Si_xN_yH_z$ films, Si-N··· H, was not observed in our ir measurement. However, significant effects of hydrogen bonding in a-$Si_xO_yH_z$ film have been observed, i.e. the reversible dissociation of hydrogen-bonded O-H··· O units with temperature.

The properties of PECVD a-$Si_xN_yH_z$ films are determined by the composition of the films and the local bonding configurations. These in turn are affected by the deposition parameters, such as substrate temperature T_s, reactant ratio R = NH_3/SiH_4, rf power density, and total pressure of deposition. The experimental results presented here show that a high gas ratio (R ≥ 40) and power density (about 0.63 W/cm^2), a low absolute SiH_4 flow rate (below 2.5 sccm), and a deposition temperature of about 350 °C will produce high quality films for device-related applications. The films prepared under these conditions will have a higher energy gap (above 5.2 eV), a lower Si-Si bond concentration (on the order of 10^{20} cm^{-3}), no detectable Si-H bonds in the infrared spectrum (i.e., the concentration of Si-H bonds is lower than about 10^{20} cm^{-3}), and low porosity and thermal

stability (i.e. with low NH_2 concentration in the film). The N and Si atomic ratio for these high quality a-$Si_xN_yH_z$ alloy films is in range 1.85 - 1.95, which is close to the composition of silicon diimide, $Si(NH)_2$.

In order to understand the correlation of local structural configurations and optical response of a-$Si_xN_yH_z$ alloys, a microstructural model based on Si-centered tetrahetra has been proposed for this alloy which explicitly considers both the effects of stoichiometry and of hydrogen content on film properties. Alloys both with and without incorporated hydrogen have been considered, including a-Si_3N_4 and a-$Si(NH)_2$. Predictions of the model for ε_1 and ε_2, the optical energy gap E_{opt}, and the static index of refraction n have been obtained and compared with experimental results. Good qualitative agreement with experiment has been found for the dependence of E_{opt} and n on the composition of the alloys. Another important achievement for the Si-center tetrahedron model as combined with the EMA analysis is to obtain the Si-Si bond concentration, N(Si-Si), in a-$Si_xN_yH_z$ since there is no direct method so far that can be used to find N(Si-Si) for the alloys. The results obtained for N(Si-Si) by using the EMA analysis are considered to be reliable because this analysis emphasizes the film absorption which is directly related to the presence of weak Si-Si bonds in the film.

The free energy model (FEM) for bonding in amorphous covalent alloys has been developed to predict the bond concentrations in a-$Si_xN_yH_z$ alloys. The predictions of the FEM for a-$Si_xN_yH_z$ alloys are in good agreement with the measured bond

concentrations in these alloy films. The success of these comparisons helps to justify the use of the quasichemical approach to the thermodynamics of the bonding in amorphous covalent alloys such as a-$Si_xN_yH_z$. These comparisons have also enabled us to determine values for the generalized interaction parameter Ω for these alloys. It has been shown that chemical ordering in a-$Si_xN_yH_z$ alloys corresponds to the preference for Si-N and Si-H bonds over Si-Si and N-H bonds, as expressed by the bond reaction equation Si-Si + N-H $\rightarrow$ Si-N + Si-H. The FEM thus provides a simple and convenient framework for understanding and expressing the competition between chemical ordering (enthalpy) and random bonding (entropy) in amorphous covalent alloys and will be useful in constructing realistic network models for a wide range of important alloy systems.

The experimental results obtained so far for a-$Si_xN_yH_z$ suggest that more work needs to be done in order to verify the change of the film composition and density at lower power density (less than 0.17 W/cm^2) and to understand the growth mechanism in this low power range. In addition, the effect of the deposition pressure on the character of a-$Si_xN_yH_z$ films has not been studied systematically. Therefore, another set of experiments under varying totai pressure of deposition can be done in order to help to understand the growth mechanism. In order to better understand the film growth mechanism, a very important study to be undertaken is to correlate the deposition parameter with the plasma species which are incident on the growing film surface.

The FEM model can be applied to different types of alloys. Further work can be done to predict the bond concentrations in alloy systems other than a-$Si_xN_yH_z$, including a-$Si_xO_yH_z$, a-$Si_wN_xO_yH_z$, a-Si_xC_y, a-$Si_xC_yH_z$, and so on.

Another interesting alloy system is a-$C_xN_yH_z$. Since C atoms have a similar role in a-$C_xN_yH_z$ alloys as Si atoms have in a-$Si_xN_yH_z$ alloys, one can use the tetrahedron model to predict the optical properties of this alloy if the experiment data for scaling of ε_i for different tetrahedra are found. Furthermore, the FEM can yield useful predictions for this alloy.

References

Aspnes, D.E. and Studna, A.A., Phys. Rev. B27, 985 (1983).

Aspnes, D.E., Studna, A.A., and Kinsbron, E., Phys. Rev. B29, 768 (1984).

Aspnes, D.E., and Theeten, J.B., J. Appl. Phys. 50, 4928 (1979).

Backmann, K.H. and Harrick, N.J., J. Electrochem. Soc. 118, 614 (1971).

Baerg, W., Sachder, S., Engel, P.R., and Gargini, P.A., in *Silicon Nitride Thin Insulating Films*, edited by V.J. Kapoor and H. J. Stein, The Electrochem. Soc., Inc, Pennington, NJ, 1983, P.476.

Bartle, D.C., Andrews, D.C., Grange, J.D., Harris, P.G., Trigg, A.D., and Wickenden, D.K., Vacuum, 34, 315 (1984).

Betts, F., Bienenstock, A., and Ovshinsky, S.R., J. Non-Cryst. Solids 4, 554 (1970).

Brodsky, M.H., Cardona, M., and Cuomo, J.J., Phys. Rev. B16, 3556 (1977).

Bruggemann, D.A.G., Ann. Phys. (Leipzig) 24, 636 (1935).

Budhani, R.C., Prakash, S., Doerr, H.J., and Bunshah, R.F., J. Vac. Sci. Technol. A5, 1644 (1987).

Bustarret, E., Bensouda, M., Habrard, M.C., Bruyere, J.C., Poulin, S., and Gujrathi, S.C., Phys. Rev. B38, 8171(1988).

Campbell, P.M. and Baliga, B.J., in *Silicon Nitride Thin Insulating Films*, edited by V.J. Kapoor and H. J. Stein, The Electrochem. Soc., Inc, Pennington, NJ, 1983, P.150.

Cardona, M., Phys. Status Solidi B118, 463 (1983).

Chayahara, A., Ueda, M., Hamasaki, T., and Osaka, Y., Jap. J. Appl. Phys. 24, 19 (1985).

Claassen, W.A.P., Valkenburg, W.G.J.N., Habraken, F.H.P.M., and Tamminga, Y., J. Electrochem. Soc. 130, 2419(1983).

Davis, E.A., Piggins, N., and Bayliss, S.C., J. Phys. C:Solid State Physics 20, 4415 (1987).

Dun, H., Pan, P., White, F.R., and Pouse, R.W., J. Electrochem. Soc., 128, 1555 (1981).

Dunnett, B., Jones, D.J., and Stewart, A.D., Philos. Mag. B53, 159 (1986).

Eblin, L.P., *The Elements of Chemistry*, 2nd. ed. Harcourt, Brace & World, Inc., p.351 (1970).

Ericksson, T.S. and Granqvist, C.G., J. Appl. Phys. 60, 2081(1986).

Gordon, P., *Principles of Phase Diagrams in Materials Systems*, McGraw-Hill, New York, (1968).

Guggenheim, E.A., Proc. Roy. Soc. (London), A148, 304 (1953).

Hasegawa, S., Matuura, M., Anbutu, H., and Kurata, Y., Phil. Mag. B57, 633(1987).

Hasegawa, S., Matsuda, M., and Kurata, Y., Appl. Phys.Lett. 49, 1272 (1986).

Hasegawa, S., Matsuda, M., and Kurata, Y., to be published in the 20th Int. Conf. on Phys. of Semiconductors, Greece.

Hasegawa, S., Tsukao, T., and Zalm, P.C., Appl. Phys. 61, 2916 (1987).

Heavens, O.S., *Optical Properties of Thin Solid Films*, Academic Press Inc., New York, 1955.

Helix, M.J., Vaidyanathan, K.V., Streetman, B.G., Dietrich, H.B., and Chatterjee, P.K., Thin Solid Films, 55, 143 (1978).

Hezel, R., Blumenstock, K., and Schorneer, R., J. Electrochem. Soc., 131, 1679 (1984).

Hezel, R. and Schorner, R., J. Appl. Phys. 52, 3076 (1981).

Ibaraki, N. and Fritzsche, H., Phys. Rev. B30, 5791 (1984).

Ishii, Y., Aoki, T. and Miyazawa, S., J. Vac. Sci. Technol. B2, 49 (1984).

Jousse D. and Kanicki, J., Appl. Phys. Lett. 55, 1112 (1989).

Jousse D., Kanicki, J., Krick, D.T., and Lenahan, P.M., Appl. Phys. Lett. 52, 445 (1988).

Katoh, K., Yasui, M., and Watanabe, H., Jap. J. Appl. Phys. 22, L321 (1983).

Kendall, David N., *Applied Infrared Spectroscopy*, New York Reinhold Pub. Corp. (1966).

Kern, W. and Rosler, R.S., J. Vac. Sci. Technol. 14, 1082 (1977).

Lanford, W.A. and Rand, M.J., J. Appl. Phys. 49, 2473 (1978).

Levine, B.F., J. Chem. Phys. 59, 1463 (1973).

Lucovsky, G., Solid State Commun. 29, 571 (1979).

Lucovsky, G., Galeener, F.L., Geils, R.H., and Keezer, R.C., *The Structure of Non-Crystalline Materials*, ed. P.H. Gaskell, Taylor and Francis, London, p.127 (1977).

Lucovsky, G, Mantini, M.J., Srivastava, J.R., and Irene, E.A., J. Vac. Sci. Technol. B5, 530 (1987).

Lucovsky, G. and Tsu, D.V., J. Vac. Sci. Technol. A5, 2231 (1987).

Maeda, H. and Arita, Y., J. Appl. Phys. 53, 6852 (1982).

Maeda, H. and Nakamura, H., J. Appl. Phys. 58, 484 (1985).

Maes, H.E., Heyns, G., Remmerie, J., Hinoul, M., Loos, H., van Calster, A., Lequesne, A., and Allaert, K., in *Silicon Nitride Thin Insulating Films*, edited by V.J. Kapoor and H. J. Stein, The Electrochem. Soc., Inc, Pennington, NJ, 1983, P.177.

Mar, K.M. and Samuelson, G.M., Solid State Technol. 32, 137 (April 1980).

Martin-Moreno, L., Martines, E., Verges, J.A., and Yndurain, F., Phys. Rev. B35, 9683 (1987).

Morosanu, C.-E., Thin Solid Films, 65, 171 (1980).

Mui, K. and Smith, F.W., J. Appl. Phys. 63, 475 (1988).

Mui, K. and Smith, F.W., Phys. Rev. B35, 8080 (1987).

Mui, K. and Smith, F.W., Phys. Rev. B38, 10623(1988).

Nagendra, C.L. and Thutupalli, G.K.M., Vacuum, 31, 141 (1981).

Nakamoto, K., Margoshes, M., and Rundle, R.E., J. Am. Chem. Soc. 77, 6480 (1955).

Narikawa, S., Kojima, Y., and Ehara, S., Jap. J. Appl. Phys. 24, L861 (1985).

Niihara, K. and Hirai, T., J. Mater. Sci. 11, 604 (1976).

Pankove, J.I., *Semiconductors and Semimetals, Vol.21 Hydrogenated Amorphous Silicon, Part B Optical Properties*, Academic Press, Inc. (London), (1984).

Philipp, H.R., J. Phys. Chem. Solids 32, 1935 (1971).

Philipp, H.R., J. Appl. Phys. 43, 2836 (1972).

Philipp, H.R., J. Electrochem. Soc. 120, 295 (1973).

Philipp, H.R., J. Appl. Phys. 50, 1053 (1979).

Phillips, J.C., Phys. Rev. Lett. 20, 550 (1968); Rev. Mod. Phys. 42, 317 (1970).

Pimentel, G.C. and McClellan, A.L., *The Hydrogen Bond,* W.H.Freeman, San Francisco, 1960.

Pliskin, W.A., J. Vac. Sci. Technol. 14, 1064 (1977).

Robertson, J., Philos. Mag. Jan (1991).

Robertson, J., Philos. Mag. B44, 215 (1981).

Saga, M. and Matsuzaki, K., *Plasma Processing*, ed. J. Dieleman, R.G. Frieser, and G.S. Mathad, Electrochem. Soc. Inc., Pennington, NJ, p486. (1982).

Sinha, A.K., Levinstein, H.J., Smith, T.E., Quintane, G., and Haszko, S.E., J. Electrochem. Soc. 125, 601 (1978).

Smith, A. L., *Applied Infrared Spectroscopy*, John Wiley & Sons Inc. (1979).

Smith, D.L., Alimonda, A. S., Chen, C.C., Ready, S.E., and Wacker, B., J. Electrochem. Soc., 137, 614 (1990).

Smith, D.L., Alimonda, A. S., Chen, C.C., and Tuan, H.C., J. Electronic Mater. 19, 19 (1990).

Soller, B.R., Snider, C.R., and Shuman, R.F., J. Electrochem. Soc., 131, 868 (1984).

Stewart, A.D. and Jones, D.I., Phil. Mag. B57, 431 (1988).

Stull, D.R. and Prophet, H., *JANAF Themochemical Tables*, 2nd ed., U.S.GPO, Washington, D.C., (1971).

Summers, D., Solid State Technol., 26, 137 (December 1983).

Swann, R.C.G., Mehta, R.R. and Cauge, T.P., J. Electrochem. Soc. 114, 713 (1967).

Tauc, R.G. and Vancu, A., Phys. Status Solid 15, 627 (1966).

Tsu, D.V., Lucovsky, G., and Mantini, M.J., Phys. Rev. B33, 7069 (1986).

Tsu, D.V. and Lucovsky, G., Mat. Res. Soc. Symp. Proc. 77, 595 (1987).

Valco, G.J. and Kapoor, V.J., in *Silicon Nitride Thin Insulating Films*, edited by V.J. Kapoor and H. J. Stein, The Electrochem. Soc., Inc, Pennington, NJ, 1983, P.128.

van der Maas, J.H., *Basic Infrared Spectroscopy*, second edition, Heyden & Son LTD, London•New York•Rheine, 56 (1972).

van de Ven, E.P.G.T., Solid State Technol. 24, 167 (April 1981).

van Vechten, J.A., Phys. Rev. 182, 891 (1969); Phys. Rev. 187, 1007 (1969).

Vinogradov, S.N. and Linnell, R.H., *Hydrogen Bonding*, van Nostrand Reinhold Company, New York, (1971).

Volgin, Y.N., Dubrovskii, G.P., and Ukhanov, Y.I., Fir. Tverd. Jela (Leningrad) 17, 1671 (1975) [Sov. Phys. — Solid State 17, 1089 (1975)].

Watanabe, H., Katoh, K., and Yasui, M., Jap. J. Appl. Phys. 23, 1 (1984).

Weast, R.C., *Handbook of Chemistry and Physics*, 52nd edition, The Chemical Rubber Co., U.S.A., (1971)

Woodward, J., Cameron, D.C., Irving, L.D., and Jones, G.R., Thin Solid Films, 85, 61 (1981).

Yadav, A.D. and Yoshi, M.C., Thin Solid Films 59, 313 (1979).

Yin, Z. and Smith, F.W., J. Non-Cryst. Solid 114, 459 (1989).

Yin, Z. and Smith, F.W., J. Non-Cryst. Solid 114, 489 (1989).

Yin, Z. and Smith, F.W., Phys. Rev. B42, 3658 (1990).

Yin, Z. and Smith, F.W., Phys. Rev. B42, 3666 (1990).

Yin, Z. and Smith, F.W., Phys. Rev. B43, 4507 (1991).